Motion measurement algorithms for MARS imaging

Fatemeh Asghariomabad

Te Whare Wānanga o Otāgo

NEW ZEALAND

A thesis submitted in fulfilment of

the requirements for the degree of

Doctor of Philosophy

The University of Otago, Christchurch,

New Zealand.

August, 2020

To loving memory of my late grandmothers,
Firozeh Abasi and Kobra Mohseni.

Abstract

The goal of the MARS molecular imaging team is to advance medicine by researching, developing, and commercialising spectral CT systems. This thesis presents the work I performed to facilitate live imaging with MARS scanners. This aim was achieved by developing a gating algorithm, designing and developing a mouse holder, and creating a motorised motion phantom. My gating algorithms will contribute to improving the image quality of human data obtained by human-scale MARS scanners.

I contributed to the design and development of a mouse holder with a temperature regulating system that is compatible with MARS scanners for the purpose of live animal imaging. This holder design provides simple animal handling, secure positioning, anaesthesia delivery, regulated temperature control, and physiological monitoring.

I developed a post-acquisition automatic gating method based on the acquired scan data over time. This method is capable of identifying various movement phases to sort the acquired exposure images into temporal bins. To reduce the undersampling noise due to gating, a weight-based reconstruction algorithm was introduced and implemented. Instead of binning the data, this method employed all images for the reconstruction of specific time points by assigning a weight to each. The result of applying this method showed that it can improve the undersampling artefacts compared to the temporal binning method.

To evaluate the gating method, a motorised motion phantom was designed and manufactured. The motion phantom could be programmed to produce periodic signals with a similar frequency and amplitude to that of a mouse or human breathing. The quantitative measurements showed that gating can reduce motion artefacts and blurring by 50% with a 1 mm amplitude and 26% for a 5 mm amplitude.

The effect of motion on the material decomposition process in MARS imaging systems was investigated. Known contrast agents were added to the motion phantom and then scanned with movements with the amplitude of 1 to 5 mm. No clear trend between the motion amplitude and the material decomposition accuracy was observed. The gated images had lower SNR compared to the non-gated data, resulting in more misidentified voxels. This suggests that noise properties are more important than motion blur.

In summary, the research documented in this thesis facilitates live imaging in MARS scanners in the future.

Acknowledgements

My sincere thanks go to Professor Anthony Butler for his supervision, ongoing guidance and support by providing several opportunities to attend various workshops, seminars, local and international conferences. I would like to express my sincere gratitude to Professor Philip Butler, whose advice and comprehensive comments and useful critiques of this research work were much appreciated. I would like to express my sincere appreciation for Dr. Niels de Ruiter, who supported me a lot on my PhD journey, with his professional advice, invaluable technical insight, fruitful discussions and impressive suggestions. I am very thankful to Dr. Aamir Raja and Honorary Associate Professor Nigel Anderson for their support and excellent consultation.

I thank the University of Otago, for awarding me the doctoral scholarship and supporting me by providing the necessary resources over my PhD program. Without it, this thesis would not have been possible. My special thanks are extended to Dr. Ruth Helms, Peter Hilton and Sam Gurney for their administrative support.

Also, my thanks go out to the MARS team members, for their support and feedback, which helped guide my thesis to completion by with countless hours of technical discussions. Particular mentions go to Dr. Marzieh Anjomrouz, Dr. Joseph L Healy, Dr. Stephen Bell, Dr. Ali Atharifard, Dr. Raj Kumar Panta, Brian Goulter and Dr. Mahdieh Moghiseh. My fellow PhD students made my work feel worthwhile; I am particularly grateful for motivation and support received throughout my research from Dr. Chiara lowe, Aysouda Motanaghi, Jereena Sreedharan Sheeja, Neryda Duncan, Yann Sayous and Dr. Emmanuel Marfo. I am very grateful to Dr. Marzieh Anjomrouz, Dr. Joseph L Healy, Helen Clayton, Dr. Mahdieh Moghiseh, Dr. Chiara lowe, Aysouda Motanaghi and Neryda Duncan for proofreading some chapters of this thesis.

I am particularly grateful for the assistance given by Arron Dyer in laboratory animal experiments, Geoffrey Graham and Stephen Hemmingsen for their support in design and fabrication of the motion phantom and the mouse holder, respectively.

Finally, my deepest love and gratitude to my family and friends. My beloved parents, Seyedeh Raheleh Razavi and Safarali Asghariomabad, for their endless love and encouragements. Thank you both for giving me the strength to chase my dreams; my siblings deserve my wholehearted thanks as well. Lastly, I wish to thank my loving and caring husband, Ezzatollah Saadate Omabad, for his unending inspiration, love and support. Without you, this journey would not have been possible.

Table of Contents

List of Figures

List of Tables

Academic contributions

The aim of this thesis is to contribute to MARS imaging development by providing an image processing solution for the presence of motion in the reconstructed images. This would facilitate live imaging for MARS small-bore and human-scale scanner users around the world in their studies, research and developments. This section lists the publications and achievements of the candidate.

My research was, directly and indirectly, a contribution to the research of the MARS team members by having a goal for performing *in vivo* scans with MARS preclinical and clinical scanners. The area of my contribution was in cancer research, cardiovascular imaging and human imaging. Overall, my contribution has included assisting researchers in the team in designing the scan parameters for considering the ultimate goal of *in vivo* in MARS; assisting in code development, programming and analysis of the results.

Peer reviewed conference proceeding/paper

1. Mahdieh Moghiseh, Dhiraj Kumar, Aamir Raja, Chiara Lowe, **Fatemeh Asghariomabad** and the MARS collaboration. Functionalised nanoparticles for ovarian cancer targeting and MARS spectral imaging. European Congress of Radiology (ECR), February 27 March 3 2019, Vienna, Austria.

2. **Fatemeh Asghariomabad**, Ana Ortega-Gil, Anthony P H Butler, Philip H Butler, Niels J A de Ruiter, Aamir Y Raja and MARS collaboration. Intrinsic Respiratory Gating for MARS Imaging. IEEE Nuclear Science Symposium and Medical Imaging Conference, Sydney, Australia, November 2018. *An intrinsic motion gating algorithm based on the exposure images intensity variation were developed and validated. The goal of the study is to improve the image quality of reconstructed images by mitigating motion artefacts and blurring. I contributed*

to the design of the algorithm, the MARS scanning protocol, performed scans and analysis. Imaging Conference. M-07-179.
Retrieved from: online-program/session?s=M-07#e631 [1]

3. Emily Searle et al. [includes **Fatemeh Asghariomabad**]. Distinguishing iron and calcium using MARS spectral CT, IEEE Nuclear Science Symposium and Medical Imaging Conference, Sydney, Australia, November 2018.
doi:10.1109/NSSMIC.2018.882467

4. Mahdieh Moghiseh et al. [includes **Fatemeh Asghariomabad**]. Cancer Imaging with Nanoparticles using MARS Spectral Scanner, IEEE Nuclear Science Symposium and Medical Imaging Conference, Sydney, Australia, 2018.
doi:10.1109/NSSMIC.2018.8824632.

5. Anthony Butler et al. [includes **Fatemeh Asghariomabad**]. First Living Human Images from a MARS photon-counting 8-Energy CT, IEEE Nuclear Science Symposium and Medical Imaging Conference, Sydney, Australia, November 2018.

6. Chiara Lowe et al. [includes **Fatemeh Asghariomabad**]. MARS Pulmonary Spectral Molecular Imaging: Potential for Locating Tuberculosis Involvement. IEEE Nuclear Science Symposium and Medical Imaging Conference, Sydney, Australia, November 2018.

Manuscript in preparation

1. **Fatemeh Asghriomabad**, Niels J A de Ruiter, Anthony P H Butler, Philip H Butler, Aamir Y Raja and MARS collaboration. An imaged based motion tracking algorithm for CT imaging. *This work presents the results of an automatic imaged based gating algorithm for mitigating motion artefacts in MARS Spectral CT. The goal of this algorithm is to reduce the induced motion artefacts from in vivo computed tomography images. The efficiency of the algorithm was tested on a mouse and six motion phantom datasets acquired by a MARS scanner (MARS Bioimaging). A weight-based reconstruction algorithm was developed, which targets a particular phase and uses all the exposure images for the reconstruction of each phase. The reconstructed data of the live scan in exhaled phase showed a sharper diaphragm transition compared to the inhaled phase and standard non-gated volumes. The reconstructed result of the motion phantom with the amplitude of 1 mm to 5 mm showed a sharp edge in the peak phases. I contributed*

[1] https://www.eventclass.org/contxt_ieee2018/online-program/session?s=M-07#e631

to developments of this algorithm, the phantom motion design, data acquisition and analysis, interpretation of the results, and write up of the first manuscript draft. I am the primary author of this paper.

2. **Fatemeh Asghriomabad**, Aysuda Motanaghi, Niels J A de Ruiter, Anthony P H Butler, Philip H Butler, Aamir Y Raja and MARS collaboration. Motion artefacts and Material decomposition.
   This work presents the results of studying the effect of motion on the MARS Material decomposition (MD) algorithm. A motorised contrast motion phantom with the amplitudes 0 mm to 5 mm was scanned with MARS scanner. The MARS MD algorithm were run on all the reconstructed data, and material identification and quantification were performed on the gated and non-gated dataset. No notable trend between the amplitude and the material decomposition accuracy was observed. The gated images with lower SNR did not improve the material decomposition results. I contributed to the developments of the motion gating algorithm, the contrast motion phantom design, data acquisition and analysis, interpretation of the results, and write up of the first manuscript draft. I am the first author of this paper.

Published abstracts

1. Shishir Dahal, Emily Searle, Steven Gieseg, Aamir Y Raja, Anthony Butler, , [includes **Fatemeh Asghariomabad**] and the MARS collaboration. Histology of atherosclerotic plaque compared with tissue components measured using a spectral photon-counting CT. Accepted for publication to European Society of Radiology (ECR), Vienna, Austria, 2020.

2. **Fatemeh Asghariomabad**, Anthony P H Butler, Philip H Butler, Niels J A de Ruiter, Aamir Y Raja and MARS collaboration. A motion artefacts reduction algorithm for in vivo imaging by MARS, Queenstown Research Week, Queenstown, New Zealand, 2019.

3. Philip Butler, [includes **Fatemeh Asghariomabad**]. MARS preclinical imaging: the benefits of small pixels and good energy data, SPIE Optics and Photonics: Optical Engineering and Applications, San Diego, CA, United States, 2019. https://www.spiedigitallibrary.org/conference-proceedings-of-spie/11113/111130C/MARS-pre-clinical-imaging–the-benefits-of-small-pixels/10.1117/12.2532367.

4. **Fatemeh Asghariomabad**, Anthony P H Butler, Philip H Butler, Niels J A de Ruiter, Aamir Y Raja and MARS collaboration. Optimisation of an intrinsic respiratory gating algorithm for MARS spectral CT, accepted abstract, ECR 2019.

5. **Fatemeh Asghariomabad**, Solinhac, F., Panta, R., Butler, A., Raja, A. and Anderson, N. and MARS collaboration. Physiological monitoring for spectral CT imaging of live small animals, University of Otago Student Research SymposiumTe Wānaka Rakahau - Ākoka 2017, Dunedin, New Zealand, 2017.

External presentations

Oral

1. **Fatemeh Asghariomabad**, de Ruiter, N., Raja, A., Butler, A., Butler, P. and MARS-Collaboration. A motion artefacts reduction algorithm for in vivo imaging by MARS, Queenstown Research Week, Queenstown, New Zealand, 2019. *This talk presented MARS imaging gating algorithm. The results of the application of the semi-automatic gating algorithm on the live animal data were illustrated.*

2. **Fatemeh Asghariomabad**, de Ruiter, N., Raja, A., Butler, A., Butler, P. and MARS-Collaboration. Motion artefacts and CT Imaging, Three minutes thesis competition, Christchurch, New Zealand, 2019.

3. **Fatemeh Asghariomabad**, de Ruiter, N., Raja, A., Butler, A., Butler, P. and MARS-Collaboration. Intrinsic respiratory gating and MARS imaging. MARS workshop, Christchurch, New Zealand, 2018.*The principals of the MARS gating algorithm, image quality improvements and the video of the mouse breathing retrieved form different temporal bins were presented to the audience.*

4. **Fatemeh Asghariomabad**, de Ruiter, N., Raja, A., Butler, A., Butler, P. and MARS-Collaboration. Machine learning and respiratory gating. MARS weekly Meeting, Christchurch, New Zealand, 2018. *In this talk, I presented some research on applying machine learning approaches for gating on the MARS data to the MARS team members.*

5. **Fatemeh Asghariomabad**, de Ruiter, N., Raja, A., Butler, A., Butler, P. and MARS-Collaboration. Physiological monitoring for spectral CT imaging of live small animals, Three minutes thesis competition, Auckland, New Zealand, 2017.

6. **Fatemeh Asghariomabad**, de Ruiter, N., Raja, A., Butler, A., Butler, P. and MARS-Collaboration. Respiratory gating and MARS imaging, the Postgraduate Symposium, University of Otago, Christchurch, New Zealand, 2018.

National and international poster

1. **Fatemeh Asghariomabad**, de Ruiter, N., Raja, A., Butler, A., Butler, P. and MARS-Collaboration. Intrinsic Respiratory Gating for MARS Imaging. IEEE Nuclear Science Symposium and Medical Imaging Conference, Sydney, Australia, November 2018.

2. Emily Searle et al. [includes **Fatemeh Asghariomabad**]. Distinguishing iron and calcium using MARS spectral CT, IEEE Nuclear Science Symposium and Medical Imaging Conference, Sydney, Australia, November 2018.

3. Chiara Lowe et al. [includes **Fatemeh Asghariomabad**]. MARS Pulmonary Spectral Molecular Imaging: Potential for Locating Tuberculosis Involvement; 2018 IEEE Nuclear Science Symposium and Medical Imaging Conference, Australia, 2018.

   Fatemeh Asghariomabad, de Ruiter, N., Raja, A., Butler, A., Butler, P. and MARS-Collaboration. Spectral CT imaging of live small animals. University of Otago Research Symposium, Dunedin, New Zealand, 2017.

4. **Fatemeh Asghariomabad**, de Ruiter, N., Raja, A., Butler, A., Butler, P. and MARS-Collaboration. Physiological monitoring for spectral CT imaging of live small animals, the Health Research Society of Canterbury poster event, University of Canterbury, Christchurch, 2017.

Student supervision

1. 2017, Fanny Solihac. Fanny was a visiting bachelor intern from Marcie University, France. My work with Fanny included teaching and supervising use of the MARS-11 scanner. I worked with Fanny to apply physiological monitoring system for respiratory gating purposes. I have supervised her in designing the physiological parameters acquiring experiments and analysing the data.

2. 2017, Ana Ortega. Ana was a PhD student from the University of Carlos III, Madrid, Spain. Department of Bioengineering and Aerospace Engineering, Spain. My work with Ana involved in developing an intrinsic motion gating algorithm

based on the MARS data.

Collaboration

Academic

1. University of Canterbury, Department of Physics. I work alongside technician staff for designing and manufacturing a motorised contrast motion phantom and also designing and manufacturing an animal holder.

2. University of Carlos III, Madrid, Spain. Department of Bioengineering and Aerospace Engineering. A PhD student worked alongside me for three months. *Details stated in student support, item two.*

3. Chinese University of Hong Kong, Hong Kong. Department of Orthopaedics and Traumatology. Applied the motion gating on the *in vivo* scans acquired by the MARS small-bore scanner in the Chinese University of Hong Kong.

4. Lincoln University, New Zealand. Scanning a motion phantom with an available CT scanner in Lincoln university.

Industrial

1. MARS Bioimaging Ltd. My research through the University of Otago is part of a large collaborative project with MBI, whose aim is to bring MARS scanners to the clinic. *I have contributed in the following ways: performing image quality assessment, developing a gating algorithm; designing and developing an animal holder for live imaging; designing and developing a motorised motion phantom, providing student support, designing scans and experiments. It is expected for the results of this thesis to become part of the commercial software for future MARS scanners. This is significant because it will help to improve the image quality of the motion effected images and increase the potential diagnostic of them. MARS scanners have already been sold around the world, contributing to a variety of preclinical research studies. In the near future, MARS will start selling its humans scanners. So this work will contribute to the medical community too.*

2. MARS Bioimaging Ltd. *I was a member of MARS CT Medipix detector, camera assembly team. My responsibilities were the installation of the detector's chips to the mounting boards, testing the functionality of each of the detectors. Designing*

mounting plates cover and assisted with electrical unit assembly, 2019.

3. MARS Bioimaging Ltd. *I was involved in developing and designing a radiologist friendly graphical user interface for MARS scanners by Python programming, 2020.*

Professional learning

1. PhD student thesis writing Workshop, 2019, Christchurch, New Zealand.
2. MPI and rat training, 2018, Christchurch, New Zealand.
3. Completed an eight weeks online course on C++, University of Tehran, 2018.
4. Completed an eight weeks online course on machine learning algorithms, University of Columbia, 2018.
5. Attended medical image reconstruction workshop: theory and practice, Sydney, Australia, 2018.
6. Attended Hybrid Imaging live conference, 2018.
7. Joined the Mind to the Market workshop, University of Canterbury, 2018.
8. Thesis/Dissertation writing when English is not your first language, 2017, Christchurch, New Zealand.
9. End-note and thesis writing workshop, 2017, Christchurch, New Zealand.
10. Study skills for new postgraduates, 2017, Christchurch, New Zealand.
11. Literature Review, 2017, Christchurch, New Zealand.
12. Plagiarism Paraphrase, 2017, Christchurch, New Zealand.
13. Stopping Spam and Viruses, 2017, Christchurch, New Zealand.
14. Instrumentation and Design, 2017, Auckland Bioengineering Institute (ABI), Auckland, New Zealand.
15. Computational physiology, 2017, Auckland Bioengineering Institute (ABI), Auckland, New Zealand.
16. Experimental Methods, 2017, Auckland Bioengineering Institute (ABI), Auckland, New Zealand.

17. Clinical Awareness, 2017, Auckland Bioengineering Institute (ABI), Auckland, New Zealand.

Professional national/internationals grants

1. 2020, **Recipient of University of Otago Departmental Award** This two-month scholarship was awarded in May 2020 to support my PhD further.
2. 2018, **Student Oral Presentation Prize** I was awarded second place oral prize for student oral presentations at the University of Otago Postgraduate Symposium.
3. 2018, **Travel Grant** Towards my travels to a 2018 IEEE Nuclear Science Symposium and Medical Imaging Conference; Sydney, Australia.
4. 2017, **Recipient of a PhD scholarship** I was awarded a Doctoral Scholarship for high-achieving international students from the University of Otago.

Chapter 1

Introduction

This thesis describes the research and developments of a gating algorithm for MARS imaging systems. The research is divided into three main parts; the first part is studying live animal imaging requirements and designing a mouse holder with anaesthesia delivery, secure positioning, temperature control, and physiological monitoring. The second part is the development of gating algorithms for improving the image quality of the motion affected volumes. This is supported by designing and manufacturing a motorised contrast motion phantom and scanning a live mouse. Finally, the effects of the presence of motion on the MARS material decomposition algorithm was investigated.

This chapter starts with the thesis objectives and outcomes in section 1.1. Section 1.2 outlines the motion artefacts and gating methods. Section 1.3 briefly explains the properties of MARS spectral imaging system. Section 1.4 outlines the thesis structure.

1.1 Research objectives and outcomes

The goal of the MARS team is to improve medicine by developing, applying, and commercialising spectral CT technology for a broad range of diseases. One of the most considerable challenges of live imaging remains the patient's movements during a

scan. The presence of the motion artefacts in reconstructed images can compromise the accuracy of measurements and threaten the diagnostic correctness. We aim to develop an automatic gating algorithm for MARS scanners as part of the image processing software tool-chain. This would help with live imaging in both the MARS small-bore scanners with laboratory animals and in future MARS human-scale scanners with patients.

This goal raised some research challenges to overcome. At the beginning of my PhD, there was no holder available for live animal imaging. Therefore, the first step was studying requirements of live animal imaging in MARS scanners to design and manufacture a mouse holder compatible with MARS scanners.

The MARS scanners as a spectral CT system have their own unique data. Therefore, the gating algorithm should be developed based on the properties of MARS spectral CT imaging.

The technology is also in an active state of development and evolution. Therefore, the gating algorithm should be flexible to support future versions. For example, the early version of the MARS small-bore scanners had only three detectors in its camera box and had to be translated to cover larger subjects. The latest versions of the camera have 14 detectors within the current human-scale prototype.

To achieve these goals, we started with laboratory mice as our first targets. We studied the requirements for supporting gating in the MARS small-bore scanners. A falcon tube was converted into a mouse holder and a live mouse was then scanned with the MARS-11 scanner (located at Otago University). Two mouse holders with physiological monitoring, anaesthetic gas delivery, and heating systems were then designed and manufactured.

We developed an automatic image-based gating algorithm and tested its functionality by using the live scan and the motion phantom data. The automatic gating algorithm requires minimal human involvement and can be applied to any scan that is found to have periodic motion of the sample.

We designed a controllable motion phantom to simulate a range of movements similar to those from a mouse or human. Its movements are consistent and controllable. Features can be added to it to convert it to a contrast motion phantom. It does not require ethics approval and it is helpful in longitudinal studies.

Given this information in the next section, we will review some background information about motion artefacts in medical imaging.

1.2 Motion artefacts

In CT, due to inaccuracies in the physical models used in algorithms, errors will show up in the images. When these errors form visible patterns, we refer to them as image artefacts. Some artefacts can be reduced by changing the scanning method and/or parameters. However, it is only by understanding and correctly modelling the physics that they can be eliminated. In CT imaging, there is a range of artefacts, including beam hardening, streaks, rings, truncation, windmill, motion, and more. Refer to an article by Barrett and Keat (2004) for other types of artefacts.

Motion artefacts will affect all medical imaging modalities simply the nature of scanning a live subject. Motion generally has 3D characteristics. Organs can move, expand or shrink throughout the scan. The image quality of reconstructed volumes with the presence of motion artefacts are degraded by double edges and blurred regions. For example, tracing the small metastatic foci in a thoracic cage of a patient with anatomical movements will be a challenge in a blurred image (Kuntz *et al.*, 2010). The presence of motion artefacts can sometimes mimic diseases and lead to an incorrect diagnosis. Therefore, avoidance and correction of motion artefacts can be critical.

Getting the patient to hold their breath is one possible option for reducing motion artefacts from the patient's side. However, this method is not very practical in animal subjects, patients with difficulty in breath-holding, and children. Even with breath-holding, some motion can be observed in the chest wall (Jiang, 2009).

The only way to truly reduce the motion from the scanner side is to either stop the subject from moving or start the exposure acquisition at the same time in the periodic signal. The latter is difficult to do accurately and slows down the scan thereby significantly increasing the dose. Alternatively, it is also possible to correct the motion through signal/image processing.

The motion in the reconstructed images originates from two primary sources: the scanner and the subject. The scanner gantry rotates continuously, and the sample bed may translate continuously in the case of a helical scan. The subject's movements can be periodic such as respiration, or it can be non-periodic such as gasping or any sudden anatomical movements. In this thesis, we will only look at the periodic motion of the subject as that should have sufficient available data to characterise and compensate for.

The configuration of the scan may also directly have an effect on better characterising the motion. A shorter exposure time means that the scanner can collect more exposures for the same scanning duration. This means the number of exposures at roughly the same phase angle in the periodic signal increases. MARS scanners have traditionally had smaller cameras than the width of the subject. This means that scans often need to translate the camera during the scan in-between helices. This greatly increases the scan time. Having more detectors in the camera helps with covering a wider volume of the subject in a single gantry rotation, meaning a faster scan.

Acquiring the motion signal with the assistance of external sensors is known as extrinsic gating. Extrinsic gating is prone to environmental noise as it requires external devices for obtaining the physiological gating data. In intrinsic gating, on the other hand, the gating signal is derived from the acquired images themselves. Similar image quality to extrinsic gating has been reported in intrinsic gating methods by Kuntz *et al.* (2010). No external devices mean less preparation time before the scan, less direct contact with the subject, and no risk of issues with the additional hardware required.

From the scanner's point of view, cardio-respiratory gating can be applied in real-time to dictate when exposure images are taken, or it can be applied after data acquisition is

completed. Real-time is called prospective, while the post-scan is called retrospective (Bartling *et al.*, 2008; Badea *et al.*, 2008). Due to needing the data to process, intrinsic gating must be done retrospectively.

Keeping the various options of gating in mind, we will next review the MARS imaging system to touch on aspects that are relevant to the work in this thesis.

1.3 MARS imaging system

The gating methods investigated in this thesis are aimed for use in MARS scanners. Therefore, we start by considering key aspects of the MARS scanner design that are relevant to gating.

MARS photon-counting scanners are comprised of five fundamental components, an X-ray source, a camera, a sample holder, a gantry, and software for image acquisition, processing and reconstruction. Fig. 1.1 shows a diagram of the MARS scanner internals. At the time of this thesis, MARS small-bore scanners were available for obtaining datasets. The scanned volume in this scanners can be up to 100 mm in diameter and 270 mm in length. The resolution (a typical cubic voxel is 80 μm wide) is not far from a micro CT (a typical voxel size can vary from 5 to 200 μm wide).

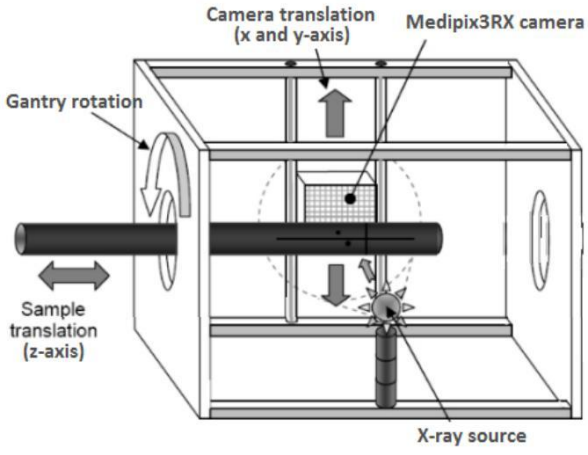

Figure 1.1: A diagram of the MARS scanner internals illustrating the the gantry rotation, X-ray source, camera translation and the sample holder's transitions (Image credit: Fred Ross, honours project at the University of Canterbury).

However, the scanner design mimics a full-body clinical CT as opposed to a benchtop micro CT. This ensures that MARS technology can be directly upscaled to human CT in the near future and that any preclinical research performed on the scanner is more easily translatable to the future human MARS scanners. For a good summary of the scanner, design refer to chapter 2 in the thesis by Anjomrouz (2017).

There is a broad range of applications for MARS imaging technology. They include musculoskeletal imaging, contrast agent and soft tissue imaging, cancer imaging such as in the lungs, cardiovascular diseases such as atherosclerosis, and more. Current researchers are limited to scanning only *ex vivo samples*. There is a growing need to perform *in vivo* imaging, for example, studying atherosclerosis and lung cancer in live mice.

We are interested in looking at the motion in mice (lung, hearts) in the small-bore scanner. In the human scanner, we are keen to look at cardiovascular diseases such as the presence of the plaque in arteries. The blood pulses, lung and heart movements may affect the position of the plaque. Even with regions such as patient wrists, there can be still some motion that we want to measure and compensate for at the resolution of MARS datasets.

A MARS camera is made up of multiple Medipix3RX detectors. Some common arrangements include a 1D array of three, five, or seven detectors in the small-bore scanner and fourteen detectors in the human scanner. Fig. 1.2 shows an image of a three-detector camera from a live mouse scan. Each detector contains a square pixel grid of 128 rows and columns. Each pixel has eight counters that measure eight overlapping energy ranges. Among these eight counters, four use charge summing mode (better energy resolution), three do not have charge summing mode (single-pixel mode) and one is an arbitration counter. The arbitration counter measures every detectable photon above the electronic noise level. For further details, refer to chapter 10 in the thesis by Walsh (2014).

The detectors are typically placed vertically. Each detector is separated from its adjacent detector resulting in a black bar going across the image. In Fig. 1.2, there are

two such bars that indicate the gaps between the three detectors. Each detector can be misaligned in any of the three-axis. In Fig. 1.2 the thin bar on the left of the top detector and the right of the other detectors comes from a 1-pixel misalignment.

An exposure image is a grey-scale 2D image of the measured photon counts. In an exposure image, a pixel represents the photons counted by each of the eight counters.

The camera is mounted to a translating structure, which can translate radially (inwards and outwards) and tangentially (across the subject to extend the diameter of the field of view). The mounting structure is attached to the rotating gantry. If the subject is wider than the camera, the camera will be translated tangentially to multiple fixed positions across the subject.

The radial movements of the source and the camera control the magnification. The camera can move in the range of 55-110 mm and the source can move between 155 and 215 mm. The magnification has a range of 1.26 to 1.7 in small-bore scanners.

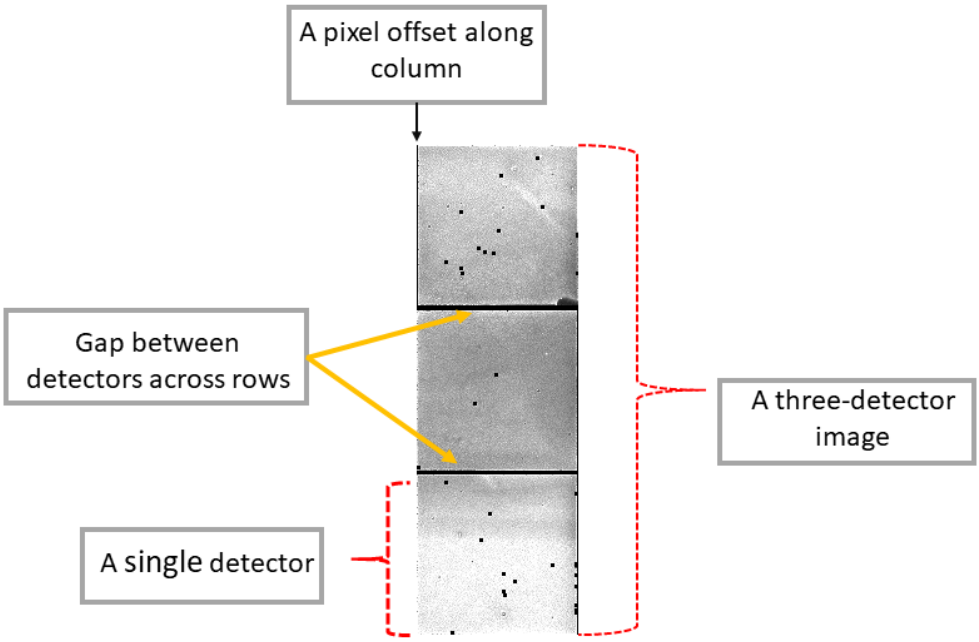

Figure 1.2: A three-detector MARS camera exposure image. The detector gap between detectors and the pixel offsets along column are shown in this figure.

The gantry rotates around the subject on a fixed axis. The sample holder can translate along the z-axis through the rotating gantry to cover the desired length in a helical scan. Any camera translations, as described above, occur in-between helices. This means that the subject may have moved between the exposures from different camera translations at the same gantry rotation angle and z position of the subject.

MARS scanners are quite slow compared to commercial CTs from Philips, Siemens, etc that can have rotational speeds that are a fraction of a second. To illustrate the typical speed of the MARS gantry, the live mouse scan, which will be introduced in chapter 4 had the gantry rotate at 1.41 degrees per second.

In this section, we reviewed key elements of the MARS system that will be important in developing the gating algorithm and supporting live animal imaging. MARS scans are helical, and the camera may translate across the object between helices. The MARS camera depending on its version is made up of different numbers of detectors. The detectors are separated with a small gap. The gating algorithm needs to deal with the complexity of hiding some parts of the subject in the gaps and it should be flexible regarding the camera size.

1.4 An outline of the thesis

This thesis reports on developments made to support live animal imaging in the MARS small-bore scanners. Developing an image-based motion gating algorithm for the MARS imaging system and studying the effect of motion on the MARS material decomposition algorithm is summarised below:

- Chapter 2 covers the studies performed to establish live animal imaging with MARS small-bore scanners. Temperature stability tests and the first live mouse scan are also presented in this chapter.
- Chapter 3 describes two mouse holders design and developments along with two heating solutions to keep the mouse warm during the scan.
- Chapter 4 details the development of an automatic image-based motion gating

algorithm along with preliminary results of applying the gating algorithm on the live mouse scan from chapter 2.

- Chapter 5 describes the design and development of a motion phantom and using it to study various aspects of the gating algorithm from chapter 4. A weight-based reconstruction algorithm is also introduced in this chapter to improve undersampling noise.
- Chapter 6 investigates the effect of motion on the MARS material decomposition algorithm.
- Chapter 7 concludes the thesis by summarising the achievements and conclusions in each chapter and introduces future research plans.

Finally, Appendix A provides details about a pixel inpainting algorithm developed in chapter 4. Appendix B studies the application of a post-reconstruction algorithm on MARS data for image quality enhancement.

Chapter 2

Live animal imaging with MARS

Live imaging of small animals presents a challenge for researchers due to motion artefacts. Small anatomical structures require high spatial resolution. However, cardiac and respiratory motion confound resolution and sensitivity, thus degrading image quality.

The ultimate goal for the MARS team is clinical imaging with live patients. The MARS scanners have successfully demonstrated several *ex vivo* preclinical applications for detection, differentiation, and quantifying different materials (Prebble *et al.*, 2018). MARS scanners are available for live animal imaging. Live small animal scanning is an effective test model for developing gating techniques that will be applicable to patient scans in the future. This chapter discusses the key factors associated with *in vivo* imaging in MARS scanners.

In this chapter, section 2.1 outlines general requirements for in *in vivo* imaging. Section 2.2 presents the result of a temperature monitoring test with a live mouse inside the MARS scanner. Preliminary tests to keep the mouse warm during the scan are given in section 2.3. Finally, the chapter concludes with a summary in section 2.4.

2.1 *In vivo* workflow of small animal imaging

Small animal imaging as a preclinical tool plays a significant role in human disease research by providing information about disease evolution and response to drug treatment (Dinkel *et al.*, 2008; Bartling *et al.*, 2008). For example, rodent models of human lung disease enable researchers to assess information about alterations in the structure and function of the lung (Brahme, 2014). Further, small laboratory rodent models of heart failure have enabled investigation into the development of heart disease in humans (Claudio *et al.*, 2015). Laboratory animals are easily handled, inexpensive and share some useful biological, anatomical and genetic similarities to humans.

The procedure of performing an *in vivo* scan in the MARS small-bore scanner has four main steps. These steps start with setting up the scan parameters, followed by setting up the physiological gating systems, then animal preparation, and finally performing the scan.

The first step is setting up the scan parameters for performing an *in vivo* scan. The field of view size is chosen based on the diameter of the subject in its widest point in (mm). The number of exposures is typically set to 720 acquisitions per rotation. The physical pixel size is 110 μm. The magnification is computed based on the source to detector distance (SDD) and the source to object distance (SOD). The filter material and its thickness determine the energy spectrum's starting point. For detection of materials which have more distinct spectral responses at low energies, aluminium filtration is suitable. On the other hand, if materials are distinguishable at higher energy ranges brass filtration is more commonly used. Removing low energy photons gives a spectrum with greater signal across smaller energy range and therefore improves spectral information.

In X-ray imaging, there is a trade-off between information and dose. Thus, scan settings are typically set between a minimum acceptable information level and a maximum acceptable dose. Tube voltage is chosen to provide an energy spectrum that will allow spectral material identification. Optimal count rates (the number of photon counts

divided by the exposure time) are based on detector performance. For the MARS scanners used, count rates between 5.7 and 6.4 counts per millisecond/pixel were recommended, giving between 1300 and 1500 total counts per pixel per exposure. Energy thresholds for each energy bin are based on maximizing spectral information for the materials of interest and frequently are chosen close to the K-edge of contrast agents if they are used.

For the live scans performed in this thesis, an available scan protocol designed by previous MARS researchers was used and it is shown in Table 2.1. Typically, the scanner first warms up the X-ray tube, then acquires the flatfield dataset before initiating the subject scan (though flatfields can be acquired after instead).

The second step is setting up the physiological gating systems. Regarding respiratory gating, there are two methods of data acquisition: retrospective and prospective. Retrospective gating acquires scanning data continuously (the default way MARS scanners acquire data). In contrast, prospective gating only acquires data during specific points in time where physiological movements are determined to be at a minimum.

Extrinsic and intrinsic methods can acquire the motion signal required for gating. In extrinsic methods, external sensors such as respiration pillows and electrocardiography (ECG) electrodes assist in recording the motion signal. In intrinsic methods, the motion signal is acquired based on the information available in the scan data. To apply gating in MARS scans, a retrospective method was chosen whereby the motion signal was acquired intrinsically. Section 2.1.1, discusses the benefits and disadvantages of these methods.

The third step is animal preparation. This may slightly change depending on the type of anaesthesia we are using. Two methods of anaesthesia are described in section 2.1.2 including injections and gas. For gas anaesthesia, an induction box needs to be set up together with a suitable animal holder. An anaesthetic machine, which generates a mixture of inhalation anaesthetic gases and oxygen for induction and maintaining the anaesthesia, should be ready for connection. The scavenging and waste anaesthetic gases system, which deals with ventilating anaesthetic gases, should also be prepared

for connection. Any physiological monitoring equipment and the core body temperature controlling system should be tested and be ready for the experiments. By having everything available for commencing the experiment, we place the animal in an induction box to be anaesthetised. Once the animal is unconscious, it is placed within the custom-made holder. The monitoring equipment will then be attached to it, and the holder will be mounted inside the scanner.

For injecting anaesthesia, the following needs to be prepared: an animal holder, a temperature controlling system and the physiological monitoring equipment, and the injection drugs and needles. The animal is weighed and placed in a secure container while drug calculations (dose based on weight) are performed. After completing the injection and ensuring that the animal has reached the desired level of anaesthesia, it will be placed inside the holder and mounted into the scanner.

The final step is starting the scan. The scanner acquires 2D exposure images with (scan) and without (flatfield) the subject in the field of view. The scan data, along with the flatfield data are then processed by the MARS iterative reconstruction algorithm. It produces 3D volumetric images with cubic voxels that are typically $80\,\mu$m wide.

In performing live imaging, some mistakes can happen that threaten the whole experiments. If the mouse gets a deep level of gas anaesthesia or overdose of injection, this can result in hypothermia, slow recovery or death. If the gas anaesthesia dose is too low the mouse may wake up and move during the scan. In injection methods, there is a risk of needle stick injury by an operator. An incorrect or poor seal with the holder may lead to gas leakage, contamination of the environment, health hazards for operators or an excess use of carrier and anaesthesia gas. The carrier gas is cold, so can result in hypothermia of the animal if under for an extended period.

In the scan parameters settings, a wrong selection of current and voltage can change the spectral responses. An inappropriate voltage, for example, can change the count rate and may result in photon starvation and beam hardening. Small field of view can lead to missing a part of the subject.

Wrong placement of a respiration pillow or ECG electrodes can lead to some noise in the motion signal acquisition process. This signal is then used for triggering the scan acquisition in the prospective gating. While in intrinsic gating, there is no need for additional hardware, and these types of noise are avoided. Intrinsic gating methods need to be designed carefully based on the characteristics of the imaging system. It mostly comes with retrospective gating methods as continuous motion data are critical in intrinsic gating approaches.

The process of collecting data on live animals is complicated and there are many sources of error or even failure in scanning. But the benefits are worth the effort since the ultimate goal is effective, worthwhile scans on living animals now and humans later.

2.1.1 Physiological gating

Mice as laboratory rodents are among the favourite specimens for preclinical imaging research. However, the rodent's relatively small size and their fast cardio-respiratory movements can be a limiting factor in the acquisition of dynamic structural imaging. For mice, the heart rate lies in the range of 400-600 beats per minute, and respiratory rate is in the range of 80-230 breaths per minute.

A rodents physiological movement poses a challenge in *in vivo* imaging due to motion artefacts in the reconstructed images. Respiratory movement can be more than 1 mm in amplitude (Bartling *et al.*, 2010; Guo *et al.*, 2011).

Cardio-respiratory gating can be applied during the scan in a process called prospective gating. It operates by monitoring the motion signal in real-time to trigger when exposure images are acquired. This is done by performing the image acquisition in the phases of the breathing or cardiac cycle with the least amount of organ motion. In other words, the imaging system will follow a step-and-shoot multi-frame acquisition protocol. This method is X-ray dose efficient but requires a long acquisition time and a complicated setup (Burk *et al.*, 2012; Guo *et al.*, 2011; Ford *et al.*, 2017; Kuntz *et al.*, 2010).

Gating can also be performed by retrospective gating methods. In these techniques, the acquisition of the exposure images happens continuously during the scan. Afterwards, gating is applied through signal and image processing. Therefore, the scan is independent of the gating criteria (Bartling *et al.*, 2008). The acquired exposure images will be labelled based on the acquired motion signal from the patient during the scan and sorted retrospectively into a set of scan data representing different cardiac cycles and respiratory phases (Ford *et al.*, 2009; Kuntz *et al.*, 2010). Only particular exposure images that belong to a specific cycle will be used for reconstruction. Retrospective gating is fast and could reduce the scanning time remarkably by having a constant acquisition rate (Burk *et al.*, 2012; Chavarrías *et al.*, 2008).

Glass *et al.* (2013) investigated two methods of physiological gating (prospective and retrospective) on a MARS scanner by using a lung and heart motion phantom. A marker was attached to the outer surface of a 3D lung and heart phantom to assess the consistency of exposure acquisition. The prospective gating method was reported as being successful. However, a considerable time variation between the gating signal triggering and exposure image acquisition was reported.

In summary, prospective gating methods require additional equipment to be installed and managed by the user (compared to retrospective). Software is needed to synchronise the motion signal's phase and image acquisition meanwhile retrospective gating methods are fast and free of any of these extra efforts. In performing gating with MARS, we have chosen the retrospective gating methods.

Gating signals can be acquired via a biological sensor, such as a respiration pillow or ECG. This method is referred to as extrinsic gating. If the information regarding the motion is obtained directly from exposure images without any assistance of external sensors, the gating method is called intrinsic gating or image-based gating. Obtaining a gating signal using external sensors can cause systematic biases in the reconstructed images (Rahmim *et al.*, 2004).

For performing an *in vivo* test with MARS scanners, we have developed an intrinsic gating algorithm. This algorithm is a post image acquisition tool and uses the retrospectively acquired data. This will be presented in chapter 4.

2.1.2 Anaesthesia

A required part of performing an *in vivo* experiment is to keep the rodent unconscious. Anaesthesia minimises animal movements during the scan (Tremoleda *et al.*, 2012). In small animal imaging, two methods of anaesthesia are prevalent; injection and gas.

To perform an *in vivo* scan in MARS, we have both options available. Injection does not require any supporting system. Once the mouse is injected, it will be placed inside a mouse holder and then will be mounted inside the scanner. The gas-based drug, however, requires a more complicated setup. It requires a stable and constant delivery of anaesthetic gas and oxygen to the mouse throughout the scan. As well a system for transferring the exhaust out of the scanner is required. In this section, we will discuss the advantages and disadvantages of both methods.

Gas narcosis can provide a constant level of anaesthesia for long periods of time. A constant level of anaesthesia helps to reduce subject movements further. The anaesthesia supply is flow-dependent, and higher flow rates are harmful to the mouse. The increased flow of oxygen increases the number of anaesthetic molecules flowing past the mouse, and also the amount of waste gas produced, as an animal can only breathe so much at once. This can then be expensive and even harmful to the environment (including humans) if the waste toxic anaesthesia is not properly and completely collected.

Isoflurane is an inhalation gas and is the most commonly used anaesthetic in relatively long preclinical experiments in mice (Constantinides *et al.*, 2011). The selected rate of administered gas is determined by the depth of anaesthesia required and the type of gas used. All animals have a MAC (minimum aveloar concentration). This is the amount of gas required to induce unconsciousness in 50% of a specific species. Most

animals are around 1.2-1.6 MAC. Therefore, it is common to use 1-2% of isoflurane to achieve this level of anaesthesia running at 1 L/min of oxygen. This appears to be a decent balance between sedation and oxygenation.

Controlling narcosis with injection, such as with ketamine and xylamine, is more challenging. With ketamine/domitor, a reversal agent is typically used to counter the side-effects of the domitor. Still, we would expect up to 90 minutes of anaesthesia. The temperature is critical because as it drops, their ability to process the drugs reduce, thereby extending the time taken for recovery (Suckow *et al.*, 2009).

The amount of administered injectable narcosis is determined based on the weight of the animal, dose rate, and the concentration of the drug to be injected. Compared to gas, injection narcosis is cheaper, user-friendly and less complex to use because it does not require technical support. However, injection offers a limited ability to control the depth and length of narcosis. Anaesthesia by injection can also be a bit more challenging as the degree of sedation/unconsciousness can greatly vary, and technical support may be necessary to administer an extra dose, which can cause more complications.

Injection narcosis is suitable for specific procedures where the equipment for gas is too challenging to use. Employing the same agents in different mice should cause reasonably similar effects, but there is always a bit of difference between animals. Still, there should only be a slight difference in drug effects unless one animal experiences an undiagnosed health issue.

Gas anaesthesia can be precisely controlled and altered in real-time according to test and subject requirements. This leads to decreased life-threatening after-effects, shorter recovery times and is more repeatable (Brahme, 2014). In addition, gas narcosis decreases the cardiac and respiratory rate, helping further reduce motion artefacts. This makes the gas anaesthesia a suitable method for retrospective gating (Bartling *et al.*, 2010).

The respiratory frequency and cardiac cycle are highly influenced by the type of anaesthetisation and the depth of narcosis (Brahme, 2014). Tremoleda *et al.* (2012) reports

that the cardio-respiratory system and core body temperature are highly dependent on the anaesthetic drug used and the dose of that drug. Therefore, the amount of administered dose is a critical factor in the animal's physiology. Inhalation anaesthetic agents are a better choice for imaging purposes compared to injectable anaesthetics because they reduce, rather than increase, respiratory and cardiac movements. Furthermore, inhalation anaesthetic helps with easier control of the dose and maintenance of the unconscious state. Gas anaesthesia is eliminated rapidly from the body by exhalation, which leads to rapid recovery after the scan and improved animal well being.

By reviewing the main aspects of using gas-based and injection anaesthesia, the ultimate conclusion was to use gas anaesthesia as it can provide us with the best result. Despite its requirement for additional hardware and preparation, it can provide a stable level of anaesthesia. Therefore, when designing a mouse holder compatible with MARS scanners, we need to consider the gas anaesthesia delivery and exhausts system needed. However, due to some difficulty in setting up the MARS gas delivery system in the time of this chapter's study, we have performed our tests in this chapter using the injection anaesthesia. In the next chapter 3, we will introduce methods for using gas anaesthesia in our experiments.

2.1.3 Free breathing or intubation

To limit breathing-induced motion, using intubation approaches are common. Intubation is a process of controlling breathing of a rodent via a tube inserted down the trachea and active ventilation control of the lungs during anaesthesia (Schambach *et al.*, 2010).

Systems are commercially available to monitor and control breathing, oxygen and anaesthesia transfer, and airway pressure (Brey, 2014). Intubating can lead to unnatural effects as it is not performed based on the rodent's breathing pattern. The ventilation is performed based on the ventilator's setting while the tidal volume, respiratory rate and airway pressure are selected by the operator (Ford *et al.*, 2007b).

The presence of an experienced operator during intubation is essential as the success of

intubation depends on the level of training and experience of the animal handler. The intubation can result in trachea injury, mechanically induced errors, and changes to the morphology and function of organs. Free-breathing methods allow the anaesthetised animal to breathe normally during the scan. The lung and thorax can be viewed in a more natural state, which is an advantage in disease models where the exact tidal volume and degree of inflation are critical. It avoids the potential drawbacks of intubation (Ford *et al.*, 2007a).

In this thesis, in all the *in vivo* experiments performed with MARS scanners and on the benchtop setup allowed the mice to breathe freely.

2.1.4 Temperature stability

In laboratory rodents, anaesthesia produces a rapid drop in metabolic rate. Therefore, maintaining stable body temperature during scans requires extra care in small animal imaging. Mice and rats particularly need to keep warm during the scan to prevent hypothermia. The standard core temperature for mice is $36 - 38^oC$, depending on the age breed and strain. Hypothermia can be classified as mild $30 - 32^oC$, moderate $28 - 32^oC$ and severe $< 28^oC$ (Horioka *et al.*, 2019).

There is a significant correlation between the rodent's body temperature and physiological parameters such as respiratory rate, heart rate, and recovery time. A mouse, for instance, has a high surface to mass proportion, which makes it extremely susceptible to hypothermia. Taylor (2007) reports that without a heating source, a mouse's body temperature can decrease between 4^oC to 19^oC within 10 to 15 minutes of beginning anaesthesia. A delayed recovery time is a direct after-effect of a body temperature drop resulting from anaesthesia. Furthermore, an anaesthetised rodent's body temperature is also regulated by the amounts of administered anaesthesia. In addition to anaesthesia, the cooling fan-driven airflow inside the MARS scanner, with an average temperature of 27^oC, may accelerate the core body temperature drop over the scan period. For this reason, thermoregulating devices are essential for maintaining a steady body temperature in small rodent experiments (Caro *et al.*, 2013).

Keeping the mouse warm and monitoring its core temperature during the scan and benchtop test was one of our main concerns. In this chapter, we look at off-the-shelf methods for keeping the mouse warm. In chapter 3, we will present our temperature regulating device and heaters.

In summary, to perform an *in vivo* scan with a MARS scanner, we are keen to use gas as our anaesthetic method while the mouse is breathing freely. We will need to develop heating and temperature regulating systems, which will be addressed in this chapter and chapter 3. We will present our intrinsic gating algorithm for MARS data in chapter 4.

2.2 Live animal temperature monitoring preliminary test

The first requirement in pursuing live animal imaging with MARS spectral scanner was obtaining ethics approval from the University of Otago's ethics committee. One of the concerns of the ethics committee was to maintain a stable core temperature during the scan. Therefore, we were required to perform a pilot study under ethics approval number C9 C9/17 to monitor a mouse core temperature during a scan with the MARS scanner. Thus, this section describes the tests done to accomplish this task.

Even though we wanted to use gas delivery in MARS scanners, two factors forced us to use the injection-based anaesthesia. The system was not ready for gas connections inside the scanner, and an appropriate mouse holder with gas delivery was not available. Therefore, we were compelled to perform our tests with injection narcosis first to gain some idea of what we are dealing with in regards to room temperature, scanner temperature, and mouse temperature.

The animal handling and preparation for scanning are key steps as it affects the animal's physiology. In this thesis, Model 1025T monitoring and gating system for acquiring physiological parameters of mice was used. This system monitors temperature via a rectal sensor, respiration rate via a respiration pillow and heart rate via ECG electrodes

(SAII - Instruments For Small Animals, 2017).

A C57BL6WT female mouse, 12 weeks old, 21.3 grams was chosen. For better animal handling, the mouse was first anaesthetised with Isoflurane gas 5% with an oxygen flow rate of 2 L/min. Following that, 0.21 mL of Domitor (Pfizer animal Health New Zealand) and 0.15 mL of Ketamine (Ceva Animal Health Australia) were injected by a senior animal technician.

The rectal temperature probe from the 1025T system was routed to the scanning area inside of MARS-11. For performing the test, a dedicated mouse holder was not available. Therefore, we used a modified falcon tube as a mouse holder. The anaesthetised mouse was placed inside the mouse holder and mounted inside the scanner, and the temperature probe was inserted into the mouse.

The scan protocol used in this experiment was an already available MARS protocol optimised to scan phantoms and mice with multiple contrast agents, such as iodine, gadolinium and gold. The scan parameters are shown in Table 2.1.

Table 2.1: Scan parameters for temperature monitoring scan

Scaning parameters	Set values
Scan type	Helical
Tube voltage	118 kVp
Tube current	26 µA
Exposure time	220 ms
SDD, SOD	250 mm, 200 mm
Field of view	32 mm
Circular exposures flatfields	720 over 360 ^{o}
Voxel size	0.11 mm
Filtration	2 mm Aluminium
Energy bins (CSM)	30-45, 45-60, 60-78, 78-120 keV
Pixel spacing	0.11×0.11

The mouse inside the falcon tube, as shown in Fig. 2.1, was mounted in the holder

after the scanner's warm-up and flatfield acquisition stage. The temperature trend during the total scan time of 18 minutes is shown in Fig. 2.2.

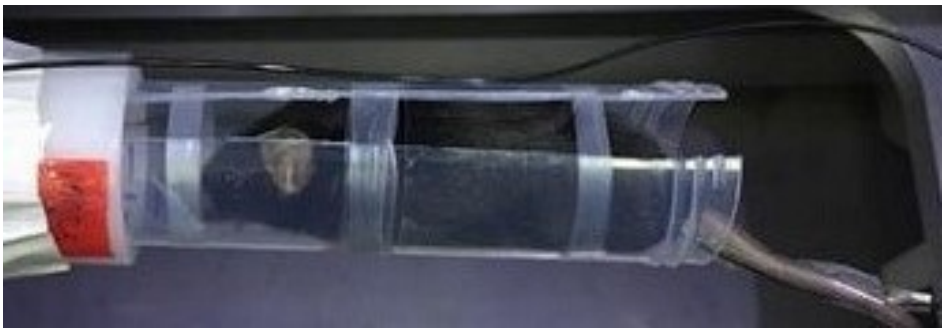

Figure 2.1: The temperature stability test performed on a mouse. The mouse placed in the falcon tube as a mouse holder and mounted inside the scanner. The core body temperature was recorded via the rectal temperature probe.

The scanner's internal temperature was stable during the experiment, with an average of 27^oC. The room temperature was 23.7^oC during the scan. The maximum and minimum of the core body temperature of the mouse were 35^oC and 31.5^oC respectively. Over the 18 minutes of the scan time, a 4.5^oC temperature drop was observed.

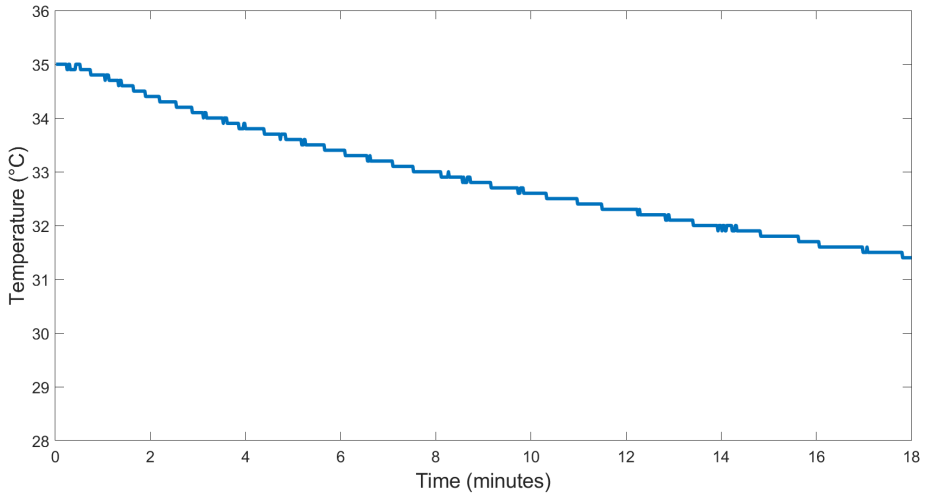

Figure 2.2: The monitored mouse core body temperature during scan time. The temperature trend is linear. Over 18 minutes of the scan time there was a 4.5^oC reduction in temperature.

The experimental result highlighted that we need to have a heating system to keep the core body temperature within safe limits $(36 - 38^oC)$. Using the falcon tube as

the holder was quite challenging and, subjectively, appeared to excessively squeeze the mouse. For the following tests, it is very important to prepare an appropriate mouse holder that provides comfortable mouse positioning.

The scan data from this experiment is the only live scan data acquired in this thesis. This scan data is used for developing and evaluation of an intrinsic gating algorithm which will be discussed in chapter 4.

2.3 Techniques for maintaining the mouse core body temperature

The result of the mouse core body temperature drop without the presence of a heating system from the previous section, motivated us to investigate a solution for keeping the mouse warm during the experiments. Therefore, in this section, we will present the result of using a chemical-based hand warmer as a heating source. To improve animal positioning, a third party's animal holder was modified to be compatible with the MARS scanner. We attached the hand warmer to the holder and measured its internal temperature during a scan using MARS-11. A mouse core body temperature trend inside the holder with the heater, on the benchtop, was also measured.

A mouse holder from one of the MARS collaborators (University of Carlos III of Madrid), became available after the previous temperature tests were done. This holder has a cylindrical shape with a diameter of 70 mm and a length of 140 mm. It has two holes for the inlet and outlet of gas anaesthesia with a diameter of 5 mm. Before scanning a mouse, the holder was modified to improve the mouse positioning and to prepare it to be usable inside MARS-11. Fig. 2.3 shows the original design and the modified version of the holder.

The original flatbed was replaced with a new 50 mm curved bed. This was done to enable the bed to bear the weight of the mouse and keep the mouse in a prone position. We moved the bed to a lower position in the holder to keep the mouse in the centre of the image. Supports were attached to the wall of the holder to limit the bed movements

during the scan. To keep the animal warm and convert the animal holder to a heated holder during the scan, we used a chemical-based hand warmer (HotHand, CW NZ, Auckland) commercially available in stores. The hand warmer was fixed and placed on the non-mounting corner of the holder, shown in Fig. 2.3.

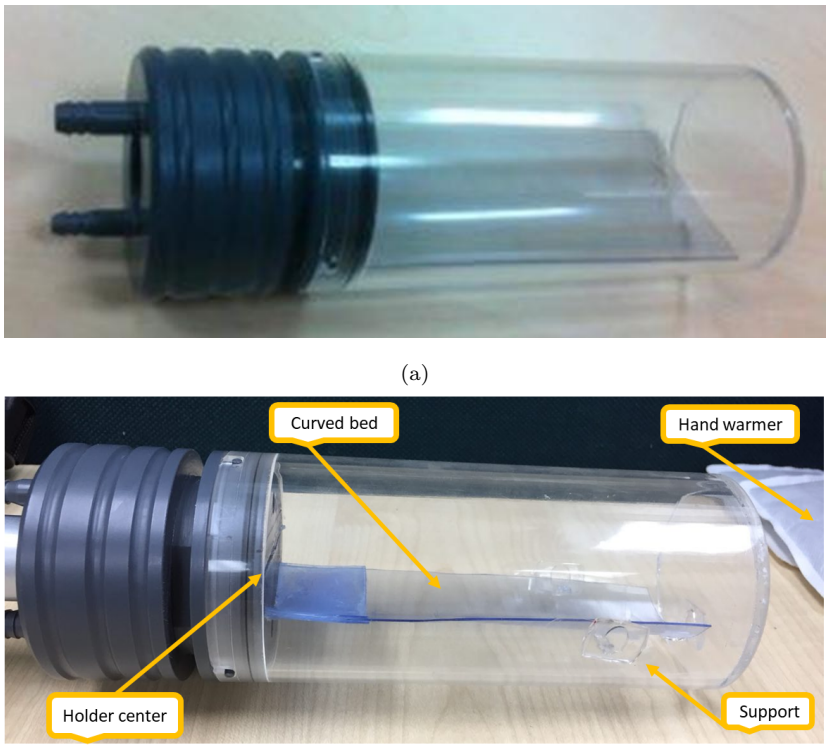

(a)

(b)

Figure 2.3: The modification performed on a mouse holder. The original holder design with a flat bed is shown in (a). The altered version of the holder, with the centre of the bed moved to a lower position to centre the mouse in the field of view, is illustrated in (b).

2.3.1 Heater's functionality test

To study the functionality of the hand warmer as the heater inside the holder, we performed two tests. To begin with, the hand warmer was attached to one end of the holder. A perspex rod was attached to the holder's bed. The holder was then mounted inside MARS-11. The 1025T temperature probe was inserted in the holder though the gas inlet hole. The acquisition protocol for the mouse holder is equal to the Table 2.1. The modified holder with the hand warmer and the temperature sensor is shown in Fig. 2.4. Fig. 2.5 shows the temperature trend during the scan.

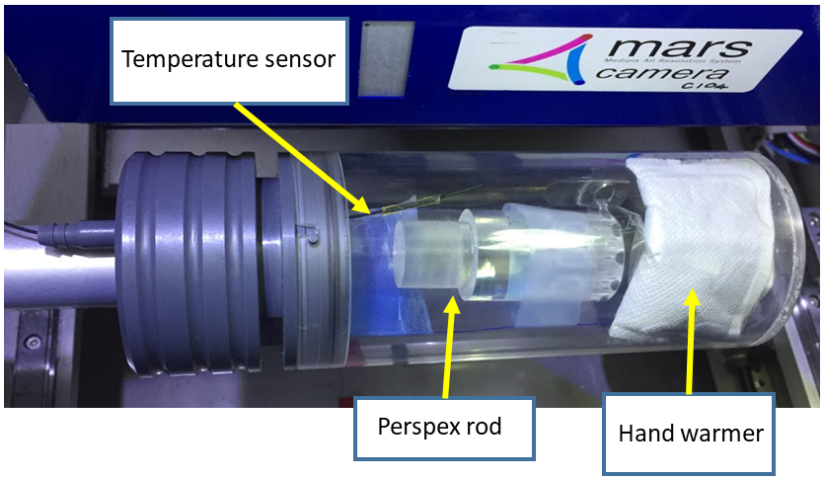

Figure 2.4: The modified holder with a perspex rod as the subject is being scanned with MARS-11 and the temperature is recorded with the small animal gating system. The temperature sensor is shown in black. The heater is attached to the right end of the holder.

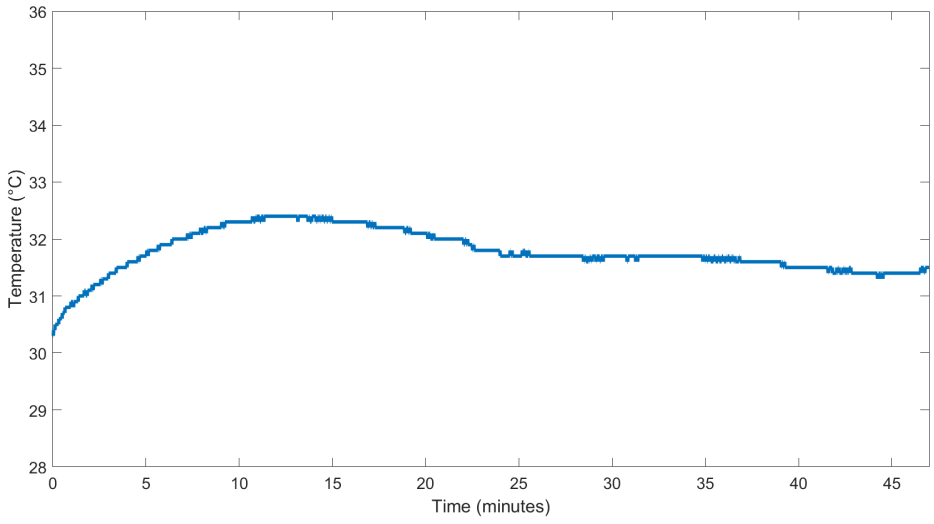

Figure 2.5: The hand warmer temperature trend inside the modified holder in the MARS scanner. The starting temperature was 30.3^oC. The temperature increased in the first 15 minutes of the scan and reached to its maximum at 32.4^oC. From there it reduced with a gentle slope.

The perspex in this scan cannot simulate the live subject since a mouse, for an example, is, by itself, a source of the heat. The aim of this test was to monitor how much heat the heater could deliver to the holder during the scan time. By performing the same

scan with a mouse we would expect to see a higher mean temperature compared to what we observed in this experiment.

The holder's internal temperature close to the perspex was monitored and recorded during the scan time of 47 minutes. An average room temperature of 24^oC was recorded. The scanner temperature was recorded at 27^oC. The starting temperature of the holder with the presence of the chemical-based hand warmer was measured as 30.3^oC. Over the first 13 minutes of scan time, the temperature reached a maximum of 32.4^oC, and the final temperature was 31.5^oC. The delivered heat in the holder area was stable with an average temperature of 31.8^oC.

In the second test, to monitor the core temperature of an anaesthetised mouse inside the holder with the presence of the hand warmer, we performed a benchtop experiment. A C57BL6WT female mouse, six weeks old, 22.3 grams, was chosen. The mouse was first anaesthetised with Isoflurane gas 5% with an oxygen flow rate of 2 L/min. Following that, 0.21 mL of Domitor and 0.15 mL of Ketamine were injected by a senior animal technician.

The initial core temperature of the mouse was 35^oC. We placed the mouse on the centre of the holder bed, activated the hand warmer, and attached the 1025T temperature sensor to the mouse. The wider space of the holder eased the mouse placement compared to the falcon tube. The mouse core temperature was monitored for 35 minutes. Fig. 2.6 shows the recorded temperature. Before the holder was sealed with the activated hand warmer and before data recording began, the mouse core temperature dropped 2^oC to 33^oC.

The presence of the hand warmer inside the holder helped to increase the core temperature from 33^oC to 35^oC in the span of 35 minutes. The heater could keep the core body temperature of the mouse at an average of 34^oC over 35 minutes of the scan time. A 2^oC increase in core body temperature during this time was observed. The benchtop experiment and the holder's internal temperatures replicate how much heat the hand warmer could deliver to the holder to keep the mouse warm during a scan.

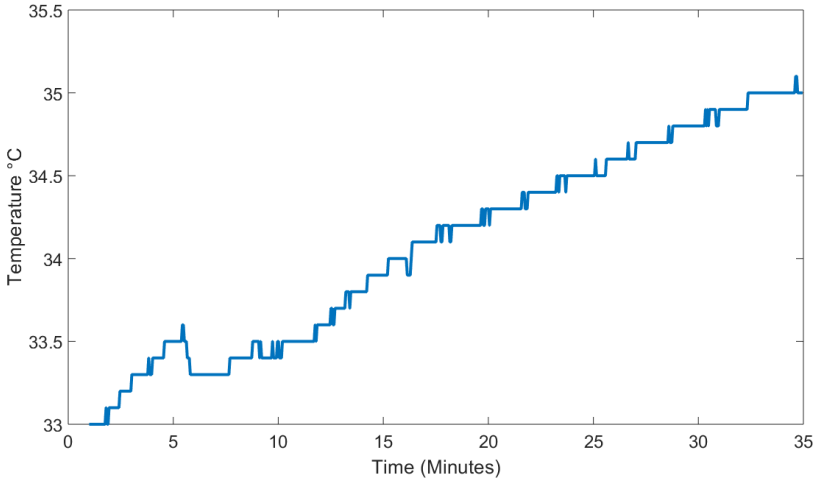

Figure 2.6: An anaesthetised mouse core body temperature inside the holder with hand warmer as a heater. In the span of 35 minutes, there was a 2^oC increase in the mouse core body temperature with a maximum of 35^oC.

The University of Otago's ethics committee requested that the mouse core temperature be maintained at 37^oC so the results of this experiment indicate some modifications are still necessary. Preventing the initial drop in animal temperature would seem particularly valuable. Techniques such as wrapping the tail, using heating pads under the induction box and utilizing heat blocks to warm up the oxygen as it is supplied to the animal can be applied in future experiments. It is also important to note that during the temperature experiments conducted in this section, there was no control over the hand warmer's delivered heat in the holder. In cases that the mouse temperature goes beyond 38^oC and cooling were required, there is no possible solution other than terminating the scan. Therefore, in chapter 3, we will try to design heating systems that include the temperature control and regulating systems.

2.4 Summary

- Intrinsic gating or image-based gating methods are defined as methods that acquire motion information based on the information in exposure images and does not require any external sensors. It is usually used as a retrospective gating technique.

- Gas narcosis methods require additional setups to injectable anaesthetics, but it is easier to control and provides a stable level of anaesthesia.
- Designing a heating system that can maintain and regulate the core body temperature of a mouse during the scan is important. The core body temperature drops linearly by time without any heating system.
- A chemical-based hand warmer was added to a modified animal holder to produce a heating holder.
- Temperature control and regulating systems remain key factors to consider for designing a heating system.

Chapter 3

Live animal imaging holder

This chapter presents the design and implementation of a mouse holder for MARS small-bore scanners. The design provides simple animal handling, secure positioning, anaesthesia delivery, temperature control, and physiological monitoring during the scan. All animals utilised in this research were treated according to University of Otago animal handling protocols, and all the tests were done in the presence of an animal specialist under ethics approval number C9 C9/17. The work presented in this chapter was done in collaboration with Dr. Joseph L Healy (MARS Bioimaging Ltd).

The work in this chapter is presented in four parts. First, a mouse holder design is presented in section 3.1, which discusses the leading factors that were considered in the design and implementation. Section 3.2 presents the first version of the holder and heater design. The design details of the second version of the holder and heater are given in 3.3. This chapter concludes with a summary presented in section 3.4.

3.1 A mouse holder design

Longitudinal studies are the primary benefit of small animal imaging. Longitudinal studies are important as a repeated scan on the same animal provides superior comparisons of long term changes, which leads to better statistical analysis. A reproducible

procedure, robust data acquisition over time and the welfare of the animal are critical factors in performing a longitudinal study.

An effective animal holder will assist with conforming to the essential requirements of longitudinal imaging. These requirements include standardised animal handling, accurate temperature control, stable anaesthesia delivery and physiological monitoring (Suckow *et al.*, 2009).

MARS imaging has been shown to provide valuable structural and anatomical information (Moghiseh *et al.*, 2018). However, a robust animal holder is essential to perform *in vivo* imaging with MARS scanners. Therefore, we aimed to build a MARS-compatible mouse holder that helps with animal longitudinal imaging and animal handling. We aimed to facilitate live imaging in MARS scanners by producing a mouse holder that enables gas anaesthesia to be administered during the scan.

Several criteria were considered in the mouse holder design for MARS imaging. It should be simple and inexpensive. It should be small enough to fit in the field of view of the MARS scanner (diameter less than 100 mm). The holder and the anaesthesia pathway should be sealed to prevent leakage of anaesthesia into the room. It should ease animal preparation before performing the scan. A temperature-regulating system is required for the animal's welfare. The holder should be easy to handle and install using an incorporated MARS mounting plate. Materials used for 3D printing the holder should have low X-ray attenuation to minimise artefacts (e.g. beam hardening) in the reconstructed images.

The following lists the fundamental components of the holder, as shown in Fig. 3.1:

- The holder is designed with two parallel pipes printed into the base of the holder below the animal bed. One tube transfers the warmed anaesthesia and oxygen mixture to the nose cone where a small nozzle accelerates the positive flow towards the animal's nose. The other tube exhausts the mixed animal exhalations to an appropriate exhaust system outside the scanner to absorb the waste gas. The continuous passing of the warm gas through the base of the holder is expected to keep the holder warm during the experiment.

- A nose cone is included in the design to directly deliver the anaesthesia and oxygen mixture to the animal. An indentation under the nose cone is designed to allow the mouse nose to be connected to the nose cone without changing its neck position.
- The holder has a circular indentation in its bed for the physiological monitoring system module 1025T's respiration pillow placement.
- Pathways are designed to pass the cables/tubes of the module 1025T temperature sensor, respiration pillow's tube, and three ECG electrodes.
- Physical restraints are designed to keep the mouse limbs secured to prevent movement.
- An air heater and temperature regulating system is provided to adjust the temperature of the holder to keep the mouse core temperature around 37^oC during the scan.

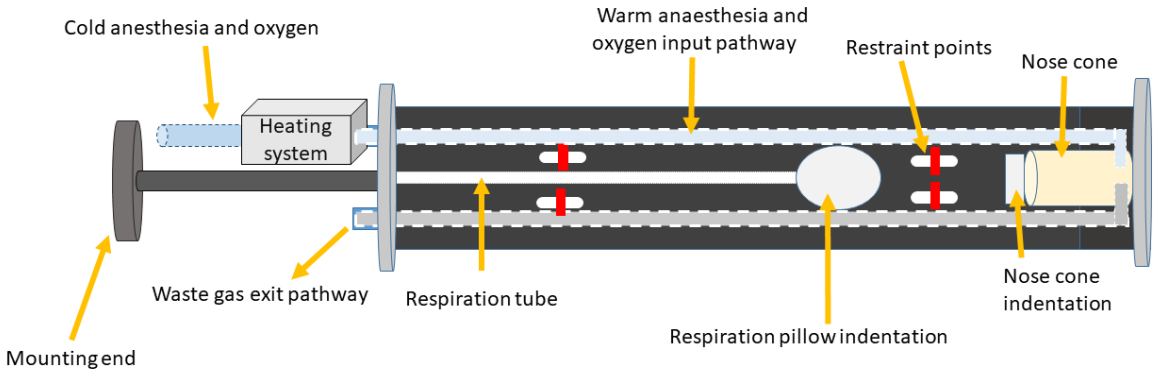

Figure 3.1: The initial mouse holder design components. The design includes anaesthesia delivery, temperature control, physiological monitoring and secure positioning.

To acquire the physiological parameters of the mouse, the available small animal control and gating module 1025T introduced in chapter 2 was used.

The MARS mouse holder has a cylindrical shape and is comprised of three main parts: a heating system, a three-dimensional (3D) printed body, and a sliding cover. The

mouse holder was designed using Autodesk Inventor 2019 (Autodesk, Inc., San Rafael, CA, USA).

The holder was designed to be airtight with a clear, acrylic cylindrical cover that slides over the 3D printed body. Having a removable cover allows easy access for mouse handling both on the benchtop and in the scanner if required. The airtight seal allows anaesthesia without the nose cone in place on the mouse if desired and serves as a backup to contain anaesthesia if the nose cone seal comes loose during a scan. The sliding cover was made from acrylic sheets.

The ideal holder's body is made from air equivalent material with the lowest X-ray attenuation. However, in reality, water equivalent materials are commonly used for the fabrication of a holder. Water is considered as a soft tissue equivalent material based on its scattering, low attenuation and X-ray energy absorption proprieties (Carlsson and Alm Carlsson, 1973). ABS (Acrylonitrile Butadiene Styrene) has a density of $1.04\,\mathrm{g}/cm^3$, which is close to water's $1\,\mathrm{g}/cm^3$. Other physical properties such as an effective Z atomic number closely resemble water (Burleson *et al.*, 2015). In addition, it is as an affordable, easily available and stable material for 3D printing purposes. Therefore, ABS was chosen as the material for 3D printing by a UP BOX 3D Printer.

A 3D printed nose cone provides a sealed mask for inhalation anaesthesia. The nose cone connects to two tubes that pass below the mouse: an intake for anaesthesia and oxygen supply, and an exhaust that leads to a vented hood or chemical trap for unused anaesthesia. A nose cone was considered a requirement in order to allow access to the mouse while in the scanner without leaking anaesthesia. This is also why a completely removable cover was chosen.

The effects of sudden movements, such as muscle contractions, can be limited by applying physical restraints on the animal (Lee *et al.*, 2014). Restraint points on the bed are designed to hold the animal's hands and legs. These restraint points prevent significant whole-body motion (such as a breath induced roll to the side), while also helping to reproduce positioning for longitudinal imaging experiments. To support mice of various lengths, several different restraints point locations are arranged near

the animal's forelimbs and hindlimbs.

To fit the mouse in the volume of the cylindrical holder and efficiently use all space available, the bed is positioned below the centre of the holder. Underneath the bed, there is only air and two gas pipes. The mouse's final position is established by the location of the circular respiration pillow, which sits in a dedicated indentation and must be positioned under the mouse's abdominal area.

To prevent the consequences of a core body temperature drop and to look after the mouse's well-being, two heating and temperature monitoring systems are designed and built and will be described in detail later in the chapter.

In the first design, the heater is outside of the holder. The cold gas and anaesthesia mixture is then warmed up in the heating system and will be transferred to the holder. The incoming oxygen and anaesthesia mixture from the SAS machine can be connected to the version 1 heater directly. From there, the warmed air will be transferred to the holder's internal area via a coupling tube. The SAS machine provided in the University of Otago has two oxygen flow settings of 2 L/min and 1 L/min. With the first version of the heater, we set the flow rate to 2 L/min at the start and once the animal was immobile and its respiration rate reduced to 60% of normal respiration, we switched the flow rate to 1 L/min.

In the second design, the heater is inside the main compartment of the holder. A feedback thermostat adjusts the heat input to maintain a constant holder temperature. In this version, the incoming gas mixture is directly connected to the holder, not to the heater. The second version of the heater does not have a gas flow rate. It warms all the gas in the main compartment to a user-defined temperature.

The heating and temperature-regulating systems are designed to monitor two temperatures: the holder interior temperature via the heater's temperature sensor and the rodent's internal temperature via the 1025T temperature sensor. The temperature of the holder is set by the user to maintain the holder's internal temperature and can be adjusted in response to the mouse's internal temperature. Because the holder has a small volume and is not insulated, changes in temperature can be made quickly in

response to adverse changes in animal temperature, whether too low or too high.

Using the warm air heating system promises to maintain a stable temperature during the scan as the amount of heat is controlled by the user. Compared to the hand warmer system described in section 2.3, the thermostat can easily regulate the holder's temperature, while the hand warmer is out of the user's control once placed in the holder.

The procedure for using the designed holder is to first anaesthetise the mouse in an induction box. Meanwhile, the heater is connected to the incoming mixture of oxygen and anaesthetic gas (for version 1). The temperature sensor, ECG electrodes, and the respiration pillow are already attached to the holder. The mouse will be placed in a prone position on top of the respiration pillow with the nose cone covering its nose. The ECG electrodes and the temperature sensor are connected to the mouse, and the limbs are secured to the holder's bed. The anaesthesia flow will be switched from the induction box to the mouse holder after knowing that the nose cone is working.

When scanning, the holder is mounted inside the scanner and the respiration, temperature, and ECG cables can be connected to the permanent extensions within the scanner. The incoming anaesthesia and oxygen flow is warmed by the heater, which is then connected to the version 1 holder. The exhaust gas tube is connected to the holder to take the wasted gas to the waste station. In the version 2 holder, the heater is placed inside the holder. To ensure the monitoring equipment is operational, the user will need to check the 1025T online recorded data in a PC connected to the monitoring system.

3.2 The version 1 mouse holder and heater

In the first design of the holder and heater, we decided to keep the heating system outside of the scanner. The warm mixture of anaesthesia and oxygen was delivered through an insulated PVC tube to the holder mounted inside the scanner. Some gross anatomical measurements were done on three female C57BL6WT mice, 6, 8 and 10 weeks old. The maximum width was 41 mm and the maximum length was 171 mm.

The distance between the chest and the longest mouse's nose was 45 mm. These simple measurements allowed us to develop dimensions for our prototype holder.

3.2.1 Holder design

The first version of the holder took into account the average diameter of a mouse and extra space for limb restraints. Therefore, the holder was made to be 46.5 mm which is also suitable for scanning in MARS research scanners (discussed in section 1.3). Due to limitations in the 3D printing machine size, the holder was made by printing and gluing two halves of the holder to each other.

A nose cone was printed in one end of the holder to efficiently deliver the mixed anaesthesia and oxygen to the animal. An elliptic cylinder nose cone with the major axis of 16 mm, the minor axis of 11.5 mm and height of 13 mm was designed. The thickness of the printed ABS in the nose cone was 2 mm. We considered having a rectangular indentation under the nose cone area with a width of a 6 mm and length of 23 mm and height of 2 mm. We decided to have the indentation below the nose cone to make it easier for us to put the membrane and O-ring on the nose cone. Without having an indentation it was difficult to get the O-ring on to hold the rubber membrane in place. The 3D design and dimensional measurements are shown in Fig. 3.2

For the test performed in this chapter, we used the model 1025T system's disposable ECG electrodes with 2 meter long cables. ECG leads were approximately 6.42 mm in diameter and the diameter of its cable was 0.04 mm. The respiratory pillow's diameter and depth were 30 mm and 1 mm respectively. The diameter of the respiration tube was set to be 2 mm. The inlet and outlet gas tube diameter were 18.65 mm. The holder included an indentation for a respiratory pillow and a pathway for its tube, which passed out of the holder to the model 1025T monitoring system. The respiration pillows indentation was designed with a diameter of 30 mm and height of 2 mm. The diameter of the restraint points was 2 mm, and the distance between the centre of each two consecutive restraint points was set to be 8 mm. The diameter of the anaesthesia inlet and outlet gas holes in the connection cavity was 5 mm.

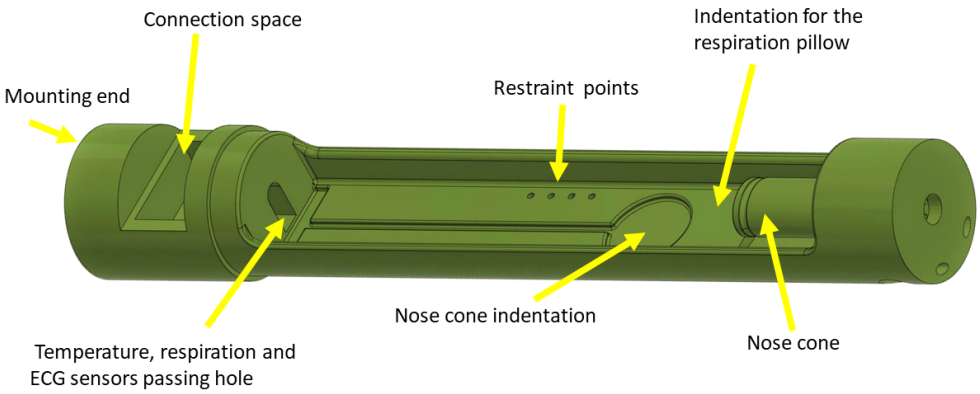

(a)

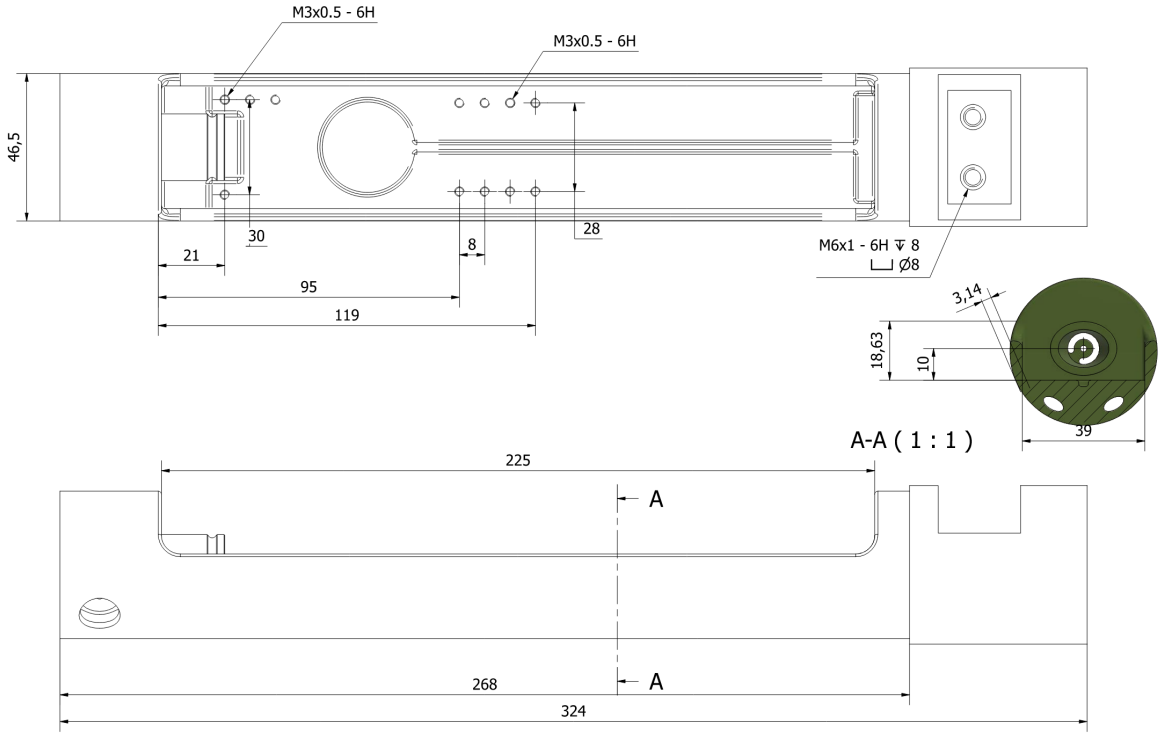

(b)

Figure 3.2: The mouse holder's first version design is given in (a) and (b).

A cavity was printed at the mounting end of the holder to accommodate the anaesthesia tubing connections. This cavity was designed to have a cuboid shape with a length of 35 mm, a width of 20 mm, and height of 15 mm. A passing hole with a diameter

of 8 mm was designed for ECG, respiration and the temperature sensor cable. The respiration tube's diameter was 1 mm and the diameter of the ECG cables and the temperature sensor were 0.05 mm. This hole connected the holder's inside space to its outside space.

3.2.2 Heater design

The first heating system attempt worked by heating the incoming anaesthesia and oxygen mixture. The anaesthesia system had a controlled positive pressure that, for mice, is typically run between 1 L/min and 2 L/min.

The heating system was first developed using a 150 mm length of 6 mm copper tubing with three small power resistors mounted to a copper plate attached to the tube. The tube was mounted in line with the flowing gas supply to the holder. In one of the ends, a mixture of cold anaesthesia and oxygen went through, and in the other end, the warm gas went out. Two pipes in the base of the holder transferred the warm gas mixture to the nose cone and took the warm exhaust out of the holder. These two lines of warm gas were considered to be heating sources inside the holder. In addition, the sealed nose cone delivered warm air directly to the mouse. A thermistor bead temperature sensor attached to the downstream end of the copper tube was used as the monitor point for the heater's thermostat. This sensor measured the temperature of the gas close to the heater's thermostat. The copper tube was heated by passing a current through the attached resistors. The power supply was approximately 15v DC. Fig. 3.3 shows the version 1 heater and the temperature regulating system.

A microcontroller and LCD display was used to set and regulate the temperature of the heater tube. A potentiometer was placed on the cover of the heating box to set the temperature by the user. The LCD showed the set temperature and the thermistor bead temperature. The maximum available set temperature in the heater was 50^oC. The heating system warmed the mixture of gas while it passed through the heater. The warmed gas was delivered to the version 1 holder.

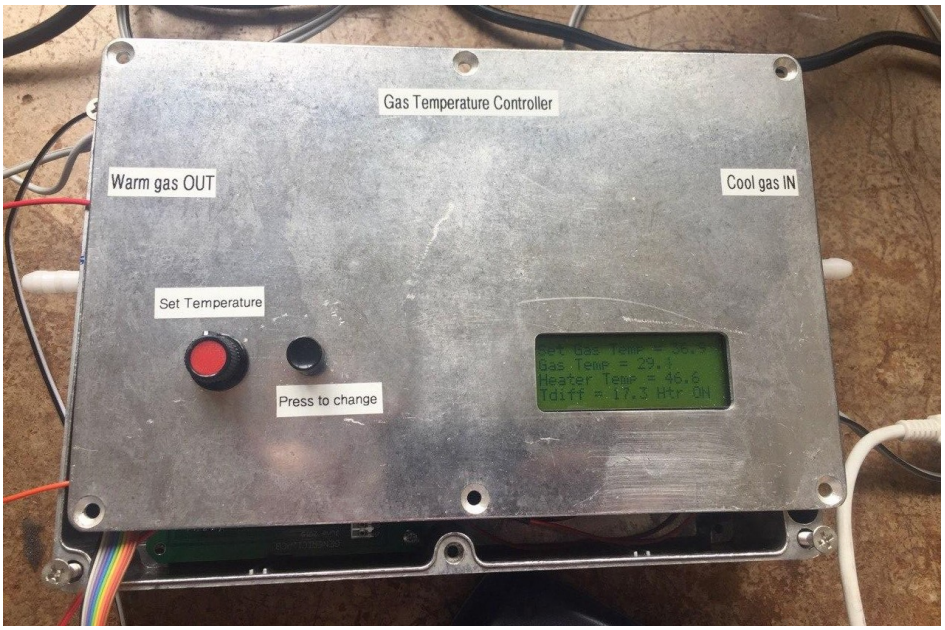

(a)

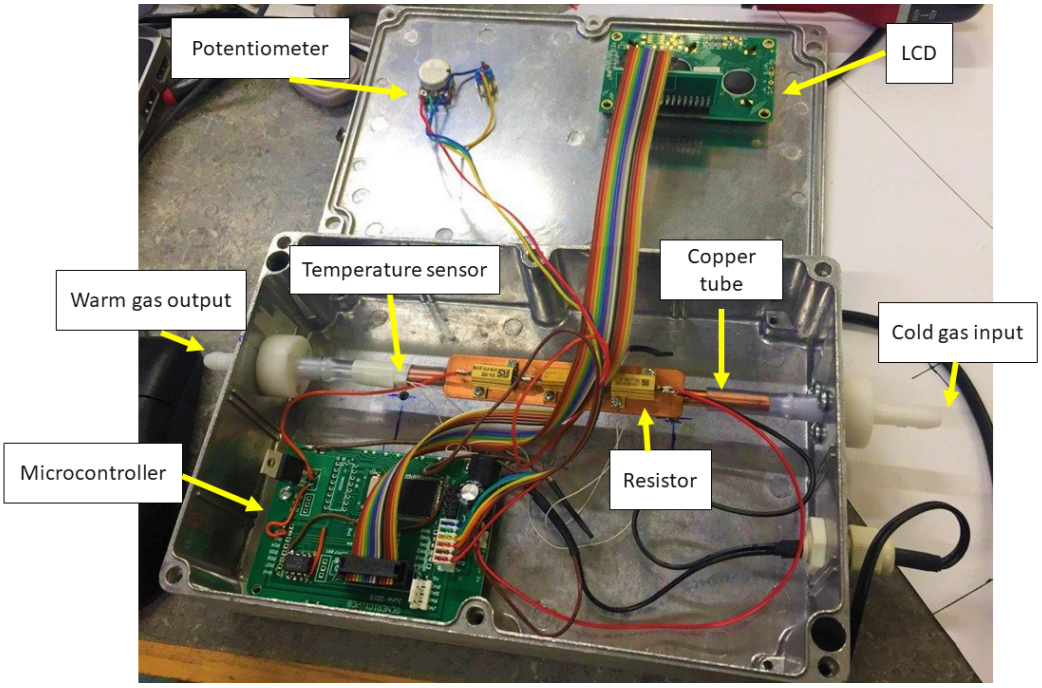

(b)

Figure 3.3: The version 1 heater and the temperature control system. The outer layer of the heating and temperature system controller box is shown in (a) which has the LCD, temperature regulator knob, and the input and the exhaust tubes. The controlling board and the heater components are displayed in (b).

3.2.3 Testing the quality of version 1 heater

To test the heat delivery to the version 1 holder, we initially took benchtop measurements by recording the temperature of the gas as it exited the heater. The anaesthesia supply tube with a set flow rate of 2 L/min was connected to the insulated one-metre tube meant to transfer the gas supply from the heater box into the scanner, and ultimately to the animal holder. The temperature of the inside of the holder was measured with the 1025T temperature sensor. The temperature of the heater was set by adjusting the value of the potentiometer.

The temperature of the heater was first set to 38^oC. After 10 minutes, the average measured temperature at the heater exit was 23^oC. To get enough heat from the heater, we set the potentiometer's temperature to its maximum at 50^oC. To measure the heat loss per unit length of tubing, the temperature value was first measured at the heater exit. Following that it was measured at the ends of two insulated 6 mm PVC tubes with lengths of 20 cm and 100 cm attached to the heater exit. The 1025T temperature sensor was inserted 10 mm into the tubing. Fig. 3.4 shows the measured temperature values in these lengths over 10 minutes. The recorded average temperatures in 0 cm, 20 cm and 100 cm of the heaters gas exit port in ten minutes were 33.1^oC, 32.4^oC and 31.1^oC respectively. The heat loss due to the insulated tubing is about 2^oC per meter. As there was no possibility of increasing the set temperature to more than 50^oC, the results indicated the maximum temperature of the warmed anaesthesia and oxygen mix is in the order of 33^oC. Our goal is to warm the oxygen and the anaesthesia gas to keep the mouse's temperature at 37^oC. The heat delivery of the heater proved to be stable and reliable, but it was insufficient.

3.2.4 Testing the quality of version 1 holder

To test the functionality of the mouse version 1 holder, a 3-month-old female C57BL6WT mouse was anaesthetised in an induction box and placed on the holder bed. 2% isoflurane with 100% oxygen flowing at 2 L/min was delivered to the animal through the nose cone to maintain anaesthesia during the measurements. The anaesthesia system

was effective for the duration of the experiment.

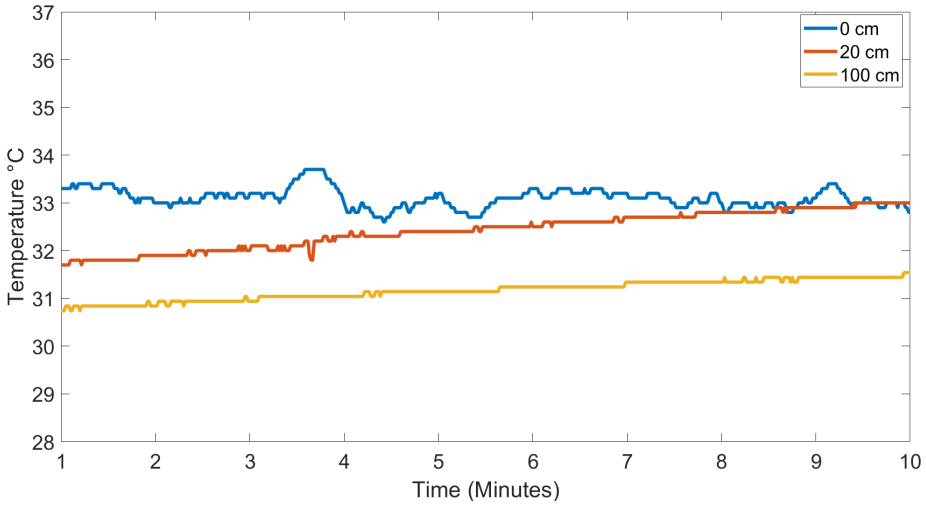

Figure 3.4: The measured temperature in three lengths (0, 20 cm, 100 cm) from the heater's gas exit port in 10 minutes.

The ECG electrodes and 1025T temperature sensor were connected to the mouse. The average respiration rate and heart rate of the mouse in this experiment were 55 breaths per minute and 420 beats per minute. In this version, the diameter of 50 mm revealed significant difficulties with the cable passthrough, tubing passing holes and the anaesthesia connections. It was also difficult to apply the physical restraints. These difficulties were compounded by the round design of the holder as the cylinder tended to roll when we placed the holder on the benchtop during scan preparations.

The distance between the nose cone and respiration pillow indentation turned out to be longer than the distance between the mouse's abdomen to the nose. This distance needed to decrease by about 5 mm. The experiment lasted only 5 minutes as the heater could not efficiently deliver enough heat to the nose cone. The mouse core body temperature had an average of 34^oC.

To connect the input gas into the holder and get the waste gas from it, we used a coupling tube. The connection space in the mounting end only increased the complexity of passing the monitoring cables and connecting the input and output gas tubes to the holder. Fig. 3.5 shows the 3D printed holder and a mouse placed in it with all the

monitoring equipment attached.

(a)

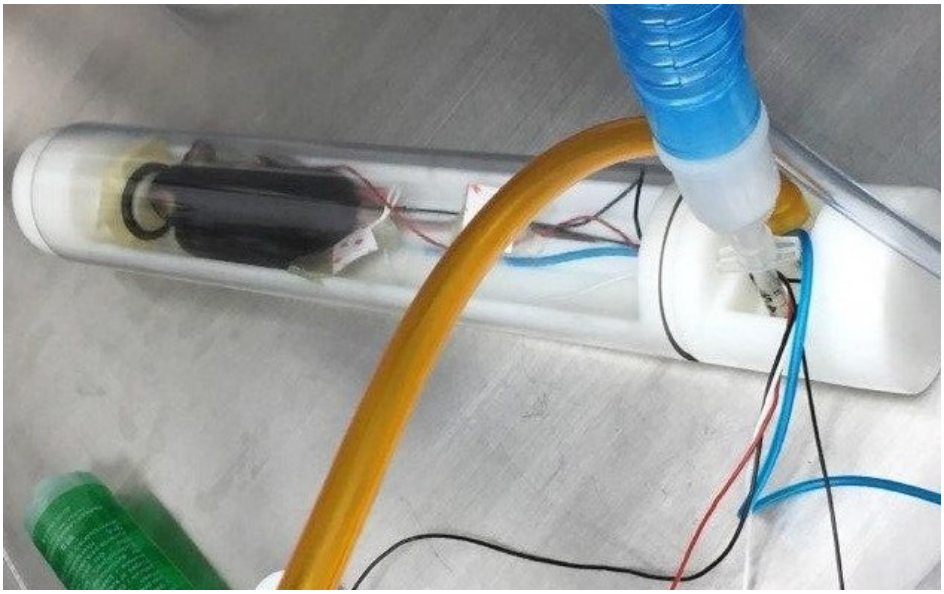

(b)

Figure 3.5: The 3D printed version 1 holder with an anaesthetised mouse in it. The 3D printed version 1 holder is shown in (a). The anaesthetised mouse placed inside the mouse holder is given in (b). The exiting cables and tubes from the connection space are the respiration sensor (narrow blue tubing), the three ECG cables (red, black and white insulated wires) and the temperature sensor (black insulated fibre optic cable). The smooth-walled yellow tube is the mixture of anaesthesia and oxygen incoming gas. The large corrugated blue tube is the exhaust.

Due to the impracticality of insulating the heater and the added benefit of removing the need for insulated supply tubing, it was decided to redesign the heater and move it into the mouse holder. This would improve the efficiency of heat delivery to the holder.

3.3 The version 2 mouse holder and heater

In the second version of the holder and heater, we mounted the heater inside the holder. This was done to reduce the heat loss observed in the previous version. In the following sections, details about heater and holder design and functionality tests are provided.

3.3.1 Holder design

In the second version of the holder design, to address issues experienced by the version 1 holder and provide enough space for mounting the heater inside the holder, we increased the diameter of the holder to 63 mm. The mounting end was redesigned to include a flattened bottom that stabilises the holder when it rests on the benchtop during scan preparations. The connection space was removed as it did not help with the passage or connection of cables and tubes. The number of physical restraint points increased to six on each side of the mouse to cover a broader range of mouse lengths.

The nose cone is now a cylinder with a diameter of 16 mm. The rectangular indentation below the nose cone now has a width of 25 mm and length of 50 mm. The distance between the centre of the respiration pillow to nose cone was reduced to 40 mm. The length of the nose cone was increased to 40 mm to bring the nose cone closer to the centre of the holder.

The diameter of the central passing hole in the mounting end of the holder increased to 12 mm to ease the difficulty of passing the cables through. This hole is used to pass the respiration tube and the temperature sensor. Two extra holes, each 8 mm in diameter, were designed in the right and left side of the central passing hole to transfer the ECG electrodes.

The gas entry and exit ports were 5 mm in diameter in both sides of the mounting end. A curved tube with the same diameter was designed to deliver the anaesthesia gas into the holder area directly when the nose cone is not being used. The second mouse holder design (version 2) is shown in Fig. 3.6. Fig. 3.7 shows the version 2

holder design with its mounting plate. The holder is glued to the mounting plate to prevent any rotation.

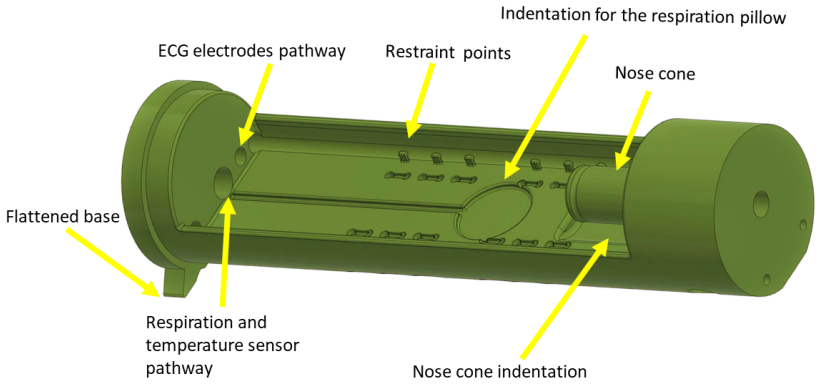

(a)

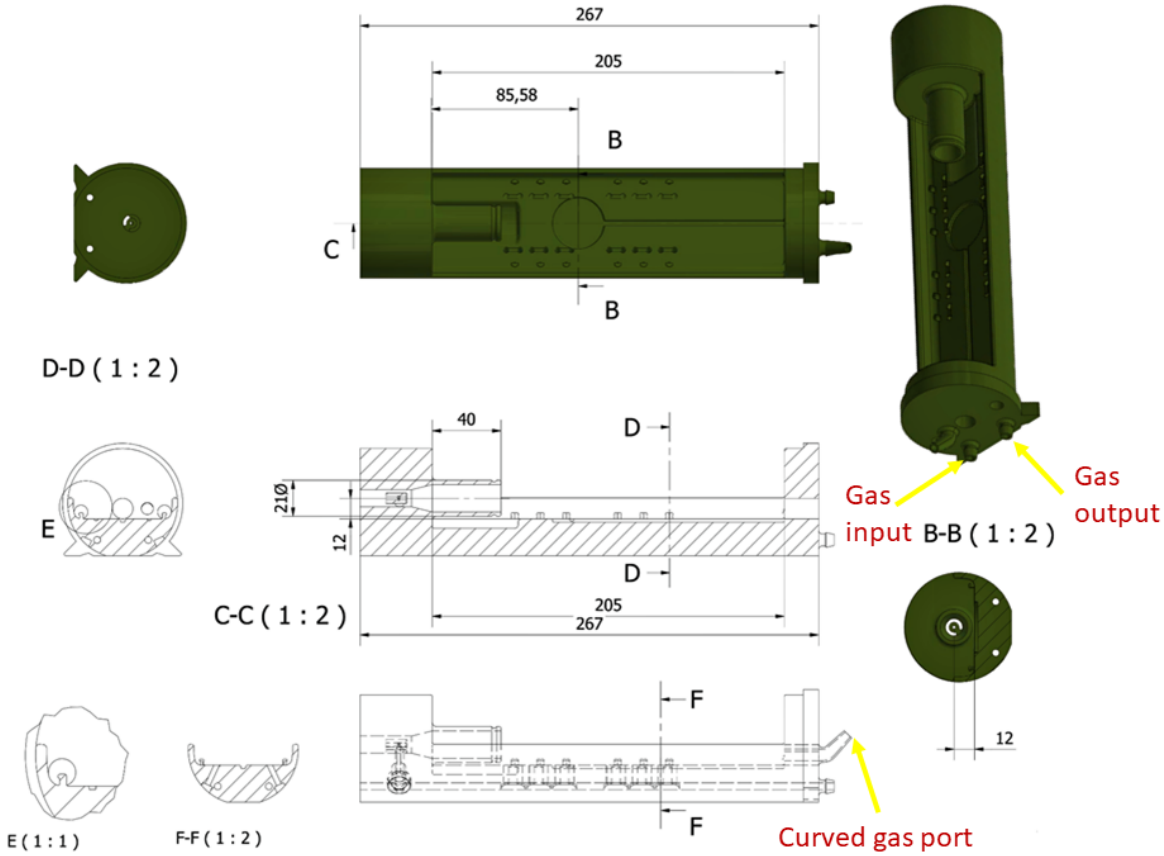

(b)

Figure 3.6: The second mouse holder design (version 2) is shown in (a) and (b).

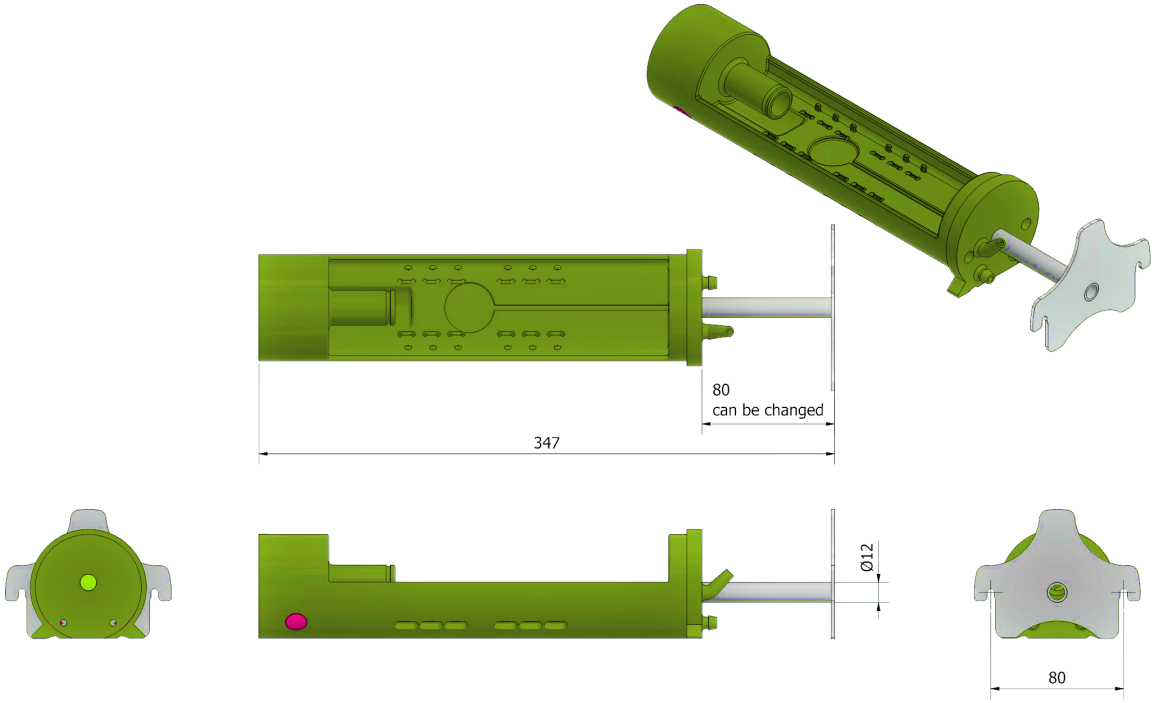

Figure 3.7: The version 2 holder and its mounting plate for the scanner.

Due to some technical difficulty in 3D printing the acrylic cover for the version 2 holder, we made a holder cover from a 250 micron thick sheet of acetate film. This clear cover in the version 2 holder is shown in Fig. 3.8.

3.3.2 Heater design

Based on the reported temperature drop in the version 1 heater, a change of plan was required. So it was decided to place a heater inside the holder to heat the gas contained inside. This new heater uses the same electronic control system. The heater itself consists of a 25 mm diameter copper tube that is 45 mm long, with heating resistors attached to the tube.

A small fan was attached to move gas around the holder to help create an even temperature. The thermostat will adjust the heat supply based on a temperature sensor positioned at the exit of the copper tube.

The heater's set temperature is manually adjusted in response to the monitored internal mouse temperature. The electronic design is the same as the version 1 heater discussed in the previous section. Fig. 3.8 shows the components of the version 2 heater and the mounted heater inside the holder.

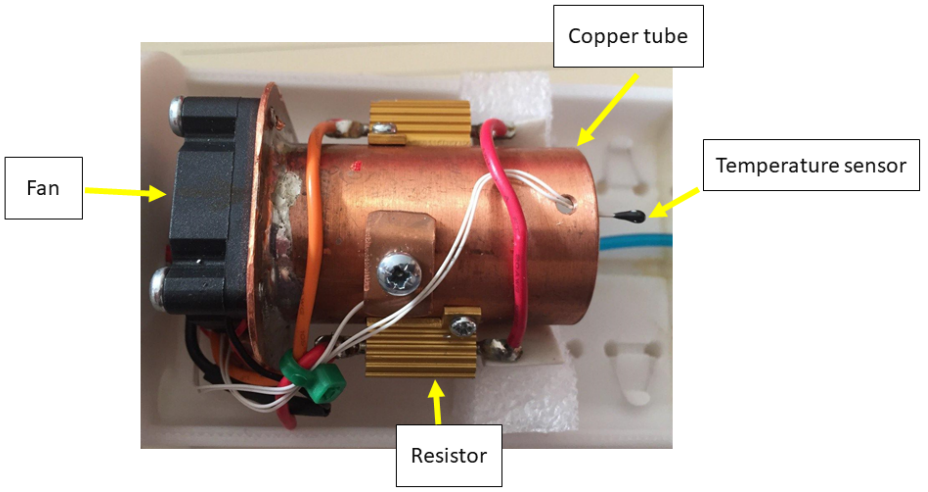

(a)

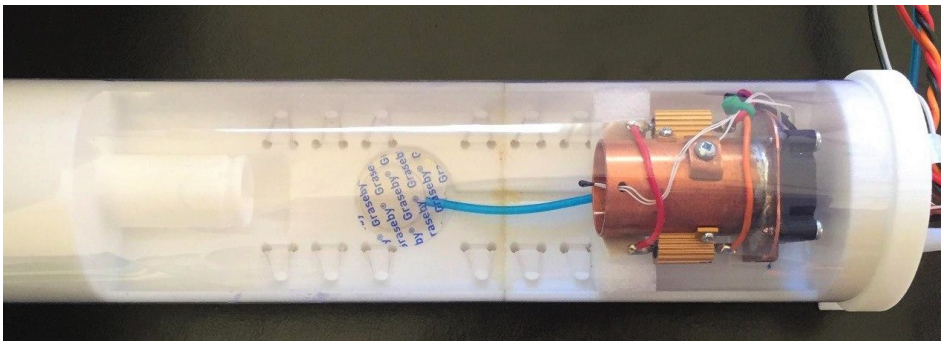

(b)

Figure 3.8: The components of the second version of the heater (a) and the installation of the version 2 heater in the version 2 holder is shown in (b). The holder is covered with a 250 micron thick sheet of acetate film.

3.3.3 Testing the quality of the version 2 heater

To test the functionality of the version 2 heater in the mouse holder, we initially performed a temperature test without the mouse, but with the oxygen supply flowing through the holder at 2 L/min. To measure the temperature variation inside the holder, we moved the 1025T temperature sensor from the nose cone area to the tail area inside

the holder. The set temperature on the heater's potentiometer was 37.1^oC. The room temperature in our experiment was 18^oC. Fig. 3.9 shows the measured temperature in the nose cone and tail area over a span of 10 minutes in room temperature. The measured average temperature at the nose cone was 33^oC, and at the tail area was 37.5^oC. In total, over a 5 cm distance, there was a 4.5^oC degree difference in the gas temperature in the holder.

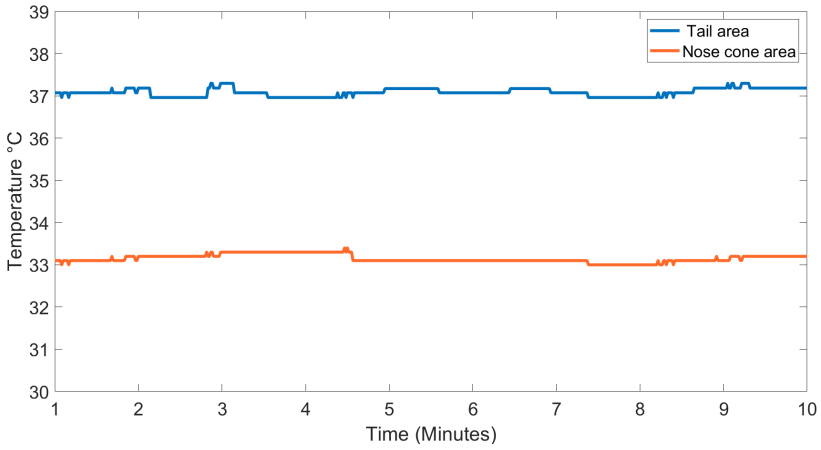

Figure 3.9: Measured temperature inside the holder in nose cone and tail area for 10 minutes. A 4.5^o difference between these two points was recorded.

One of our goals was to study the functionality of the heating system in a similar situation to the inside of the scanner. We had previously measured the MARS scanner's internal temperature during a few scans, and it was an average of 27^oC. To increase the temperature around the holder from 18^oC to 27^oC, we placed an available thin silicone heating pad (Argus Heating LTD, New Zealand) under the holder and set the temperature of its control unit at 32^oC.

The recorded temperature trend with the presence of the silicone heating pad over 10 minutes again showed a stable temperature trend with an average temperature of 33.7^oC at the nose cone and 38^oC at the tail area. In this test, over a 5 cm distance, there was a 4.3^oC degree difference in the gas temperature in the holder. This result compared to the test with the heating system confirmed the correct functionality of the heater in maintaining a stable temperature in the nose cone and tail area.

Fig. 3.10 shows version 2 heater mounted in the holder along with the temperature adjustment system as used. By getting an acceptable correlation between the heater's set temperature and the measured temperature in the absence and the presence of the silicone heating pad, we proceeded with our experiments to test the heater functionality with mice.

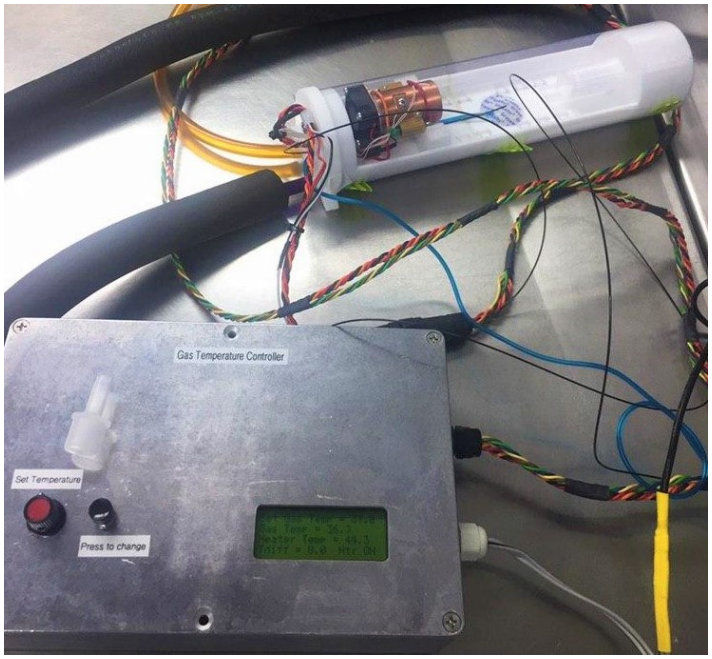

Figure 3.10: This figure shows the second version of the heater mounted inside the second version of the holder along with temperature controlling box.

3.3.4 Testing the quality of the version 2 holder

To test the functionality of holder version 2 with the mounted heater in it, two three-month-old C57BL6WT female mice were chosen: 24.3 grams and 25.4 grams respectively. They were first anaesthetised in the induction box and placed on the holder bed. 2% isoflurane with 100% oxygen flowing at 2 L/min was delivered to the holder through the gas input port.

The 1025T temperature sensor and the ECG electrodes were all easily attached. The extra space and the redesigned passthrough holes made wire and tube routing much more convenient. The mouse's forelimbs and hindlimbs were then secured by the implemented restraint points in the bed. The mouse's tail was also secured and placed

away from the heater to avoid possible harm.

The first issue we confronted in the first test was with the nose cone anaesthesia and oxygen mixture delivery. The delivery of the incoming gas to the nose cone exhaust tube was insufficient. In this version, the nose cone was lengthened to the central part of the holder, but, the narrow tube that accelerates the incoming anaesthesia mixture to the mouse's nose was not equally extended. Therefore, anaesthesia was not sufficiently delivered to the mouse to keep it anaesthetised. Consequently, we used a small tube as coupling to transfer the gas directly to the mouse nose. Still, the mouse started moving quickly after being sealed in the holder, meaning inadequate anaesthesia. The respiration and the heart rate of the mouse at the beginning of the test were 55 breaths per minute and 420 beats per minute and they increased to 100 breaths per minute and 590 beats per minute respectively when we terminated the experiment. Fig. 3.11 shows the temperature monitoring experiment with an anaesthetised mouse.

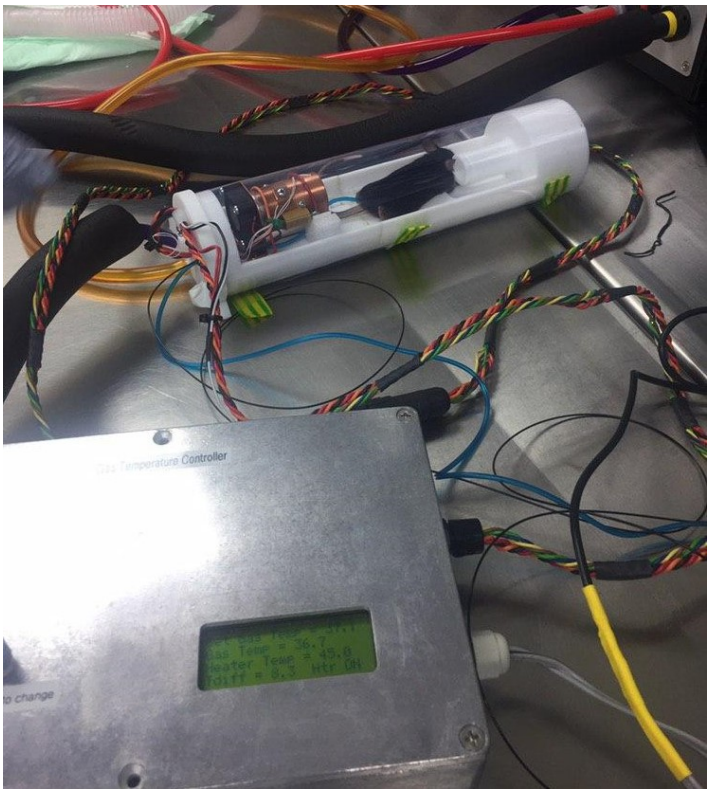

Figure 3.11: The second version of the heater mounted inside the second version of the holder with the anaesthetised mouse in it. The nose cone could not deliver the anaesthesia to the mouse, so the anaesthesia and oxygen mixture gas was infused inside the holder.

To keep the second mouse anaesthetised, the incoming anaesthesia/oxygen supply line was connected to the curved tube at the mounting end, meaning the entire holder was infused with the gas mixture. The exhaust was still routed from the printed nose cone. Therefore, the mouse was positioned appropriately over the respiratory pillow, but the mouse's head was laid to the side of the nose cone as can be seen in the figure. The temperature was measured for the mouse in this experiment.

The second mouse's core temperature at the beginning of the test was 35.5^oC. This mouse was completely unconscious during the 30 minutes of test time. The mouse core body temperature, measured by the 1025T temperature sensor versus the heater's set temperature is shown in Fig. 3.12. With a 2^oC change in the heater's set temperature over half an hour, there was a 1^oC increase in the mouse body temperature. The heater's set temperature was recorded every 5 minutes and the mouse's core body temperature was recorded constantly. There was a high correlation between the set temperature, the heater temperature inside the holder, and the core body temperature. The second mouse's respiration and cardiac rate were stable in this experiment with 51 breaths per minute and 430 beats per minute. The version 2 heater could support enough heat to keep the mouse core temperature in the range of 37^oC. However, there is a need for some modification in the holder for future designs. The zero dead space nozzle should be extended with the same length of the nose cone to allow the use of the nose cone.

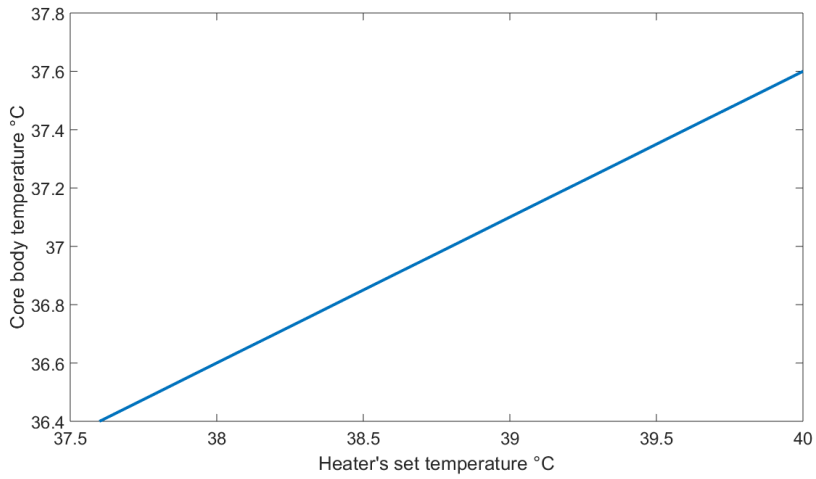

Figure 3.12: The measured mouse core temperature versus the heater's set temperature.

We could not proceed with measuring the mouse temperature inside the scanner as there were limitations to access the lab facilities. However, the result of the core body temperature confirmed the efficiency of the heat delivery and ease in connecting monitoring sensors to the mouse. In the future, after modifying the nose cone, further tests should be performed inside the scanner to study the temperature trend and the heat delivery of the heater.

The next steps for incorporating the version 2 mouse holder into the small-bore scanners are:

- Modifying the version 2 holder to fix the nose cone which did not sufficiently deliver the gas to the mouse.
- Monitor and record the respiration with external sensors as a ground truth for respiratory gating.
- The cover of the holder in future versions needs to be 3D printed.

3.4 Summary

- Two mouse holders with secure positioning, gas anaesthesia delivery, temperature control and physiological monitoring capabilities were designed and tested.
- Two heating systems were introduced and tested to keep the mouse warm during benchtop tests.
- The version 2 heater, mounted inside the version 2 holder, demonstrated a competent performance with a consistent core temperature around 37^oC.
- The version 2 holder needs modification in its anaesthesia gas delivery for future versions.

Chapter 4

Creating an intrinsic gating algorithm

The motivation for the work presented in this chapter was to develop a gating algorithm to improve the image quality of reconstructed slices that are degraded with motion artefacts. This method does not require any user intervention, interpolation, or presence of an expert. Finally, we aim to merge the proposed gating process into an automated commercial image processing software toolchain. This would prevent errors resulting from human involvement, and it would also speed up the entire process of gating.

The gating algorithm is constructed from five different algorithms. This includes an image pre-processing algorithm, a region of interest defining and tracking algorithm, a motion signal extraction algorithm, an exposure image sorting algorithm, and an iterative image reconstruction algorithm. A dataset collected from a live mouse, presented in chapter 2, from a MARS scanner was used to evaluate the function of the algorithms. The results and outcomes show improvements in the edges and feature detection after implementing our gating algorithm. The development of the gating algorithm presented in this chapter was done in collaboration with Dr. Ana Ortega-Gil from the University Carlos III de Madrid, Spain.

This chapter starts with section 4.1 which provides a brief overview of the MARS scanner and its features. Conventional methods for extracting a motion signal are presented in section 4.2. Section 4.3 provides an overview of the five steps taken in the developed algorithm for tracking motion from exposure images. Section 4.4 presents the results of the gating algorithm's evaluation. Lastly, a summary is provided in section 4.5.

4.1 MARS imaging requirements

The MARS imaging system and its properties were described in section 1.3. The points below summarise the key influential factors in developing a gating algorithm for MARS:

- The scans are helical scans. This means that the moving part of the subject may not always be in the field of view in the z-axis.
- The camera may translate across the subject between helices. This means that the moving part of the subject may not always be in the field of view in the x-y axis. Also, the subject may have moved between translations.
- The camera is made up of detectors with small gaps between them. We will need to deal with the complexity of the gaps hiding parts of the subject.
- Different cameras have different sizes. The algorithm must be flexible enough to be applied to any MARS camera.
- External equipment for measuring motion adds additional features to the subject e.g. wires, makes the animal handling more complex, and is not always reliable. We would prefer to target an intrinsic algorithm that only relies on the imaging data collected. This also offers an advantage that we can apply such an algorithm to a dataset where motion was not expected to be a significant problem and later determined to be an issue.

Given this understanding of how the data is collected, we next continue with a review of common motion tracking algorithms in the literature and discuss possible options

for MARS imaging.

4.2 Common motion signal extraction methods

Over the past few decades, researchers have been looking at intrinsic gating algorithms. Among these researchers, Chavarrías *et al.* (2008) proposed an image-based algorithm for stop and shoot type acquisitions in cone beam micro CT. In each angular position, several frames were acquired before the gantry was rotated. A difference image was obtained between each acquired frame and an average frame. This difference highlights the moving areas. The motion signal was obtained by analysing the histogram of the difference images. After using this signal to correct motion in the reconstruction, the results indicated a sharper transition in the moving edges after respiratory gating. This method is not applicable for MARS imaging as it requires the acquisition of several frames per angular position.

Zijp *et al.* (2004) introduced the Amsterdam shroud technique. In this technique, to enhance the oscillating structures in each exposure image, edge detection and thresholding were performed on scan data. These steps were followed by collapsing each enhanced exposure image into a column along the craniocaudal axis. The following step was combining all the columns to create a 2D image known as an Amsterdam shroud image. To detect regions with motion, a derivative overtime was applied on the Amsterdam shroud image. The breathing signal was acquired by plotting the absolute value of the derivative versus the exposure number. Finally, post-processing algorithms removed slow frequency components from the signal. The Amsterdam shroud technique is efficient when the moving structures are in the field of view of the exposure image (Yin *et al.*, 2007; Martin *et al.*, 2015).

The requirements of having moving structures in the field of view are a challenging concern with MARS imaging as helical scanning means that moving structures will likely enter and leave the field of view during the scan. Therefore, we would prefer to opt for a method that does not rely on moving structures always being present.

Rit *et al.* (2005) outlined a motion tracking method for 4D CT based on choosing thousands of feature points in each exposure image and following them in the sequence of exposure images in the time domain. Tracking feature points was done with the block matching algorithm. Motion analysis of the feature points resulted in sets of trajectories, which were later processed to generate the motion signal. The slow frequency motions were removed by applying a Fourier high pass filter. An almost 90% correlation between the gold standard signal and the acquired signal was observed in the final results. However, the accuracy of the method is dependent on the number of temporal bins that exposure images are sorted into for reconstruction.

Berbeco *et al.* (2005) first introduced an intensity analysis method for fluoroscopic imaging, and this was modified for CT imaging by Kavanagh *et al.* (2009). The intensity analysis method was established based on analysing the pixel value variations between sequences of exposure images. In an example of respiratory gating, they first summed the values from all pixels that covered the lungs for each exposure image. This step was followed by plotting these summed values to get a motion signal. Due to the different time scales between slow movements, such as the gantry rotation, compared to fast movements, such as breathing, applying a low-pass filter was the final step to remove the slowly varying signals. The intensity analysis method displayed a stable performance in the absence of moving structures in the exposure image (Yan *et al.*, 2013). In total, if a moving structure is out of the field of view, the intensity simply will not change other than what the scanner motion does. So it will easily work with lengthy helical scans.

Vergalasova *et al.* (2012) proposed a method based on applying the Fourier shift theorem to the exposure images. This approach is developed based on the fact that a change in Cartesian space would correspond to some shift in the frequency domain. This method has shown some success in respiratory signal extraction in cases where the diaphragm is not always in the field of view. The motion signal can be tracked either based on the phase or amplitude component of the Fourier transform of the image. They both produced similar results, yet also had a phase shift compared to the ground truth signal. The phase Fourier transform methods result's accuracy is

more dependent on the size and shape of the region of the interest while the amplitude method is less dependent on the region of interest selection. The respiratory signal derivation based on the amplitude of the Fourier transform produces similar results as the intensity analysis method introduced by Kavanagh *et al.* (2009).

Yan *et al.* (2013) investigated a feature extraction method based on the local principal component analysis to advance the Amsterdam shroud method. This method uses the Amsterdam shroud 2D images as the input for the algorithm. The local principal component analysis splits the input into background and foreground images. Then, the local principal component analysis algorithm will be applied to the foreground by a sliding window approach. This technique is built upon the fact that the oscillating structures should be present in all acquired exposures (Martin *et al.*, 2015). The results of this method showed an acceptable improvement to the overall performance over the Amsterdam shroud, intensity analysis and the Fourier transform method. In contrast, the intensity analysis method showed the highest stability in all experimental tests.

Among all the methods mentioned above, the intensity method has demonstrated an acceptable response, even with the absence of moving structures in the exposure image. It is applicable for continuous scanning with a helical trajectory. Therefore, we have decided to pursue a motion tracking method based on the photon count variation for MARS imaging.

4.3 Gating based on the image photon counts

In the breathing process the superior-inferior movements of the diaphragm and the lung's contraction and expansion lead to a change in the thoracic cavity volume. This change alters the amount of tissue and air in the beam path for a single pixel. Two bits of tissue that were observed in different pixels might now be aligned in the same pixel. Therefore, the sum of the attenuation of both bits of tissue in the same pixel changes, and hence, fewer or greater photons are measured. Therefore, the variation in a pixel's photon counts is the fundamental factor used in this method. For now,

we will use images acquired from the arbitration counter as it has the highest counts among all energy bins.

This method is made out of a combination of five steps after image acquisition:

- Step 1: Process the exposure image by masking malfunctioning pixels, applying the flatfield correction, ring artefact filtration, and inpainting the masked pixels. This is presented in section 4.3.1.
- Step 2: Define a window to cover a region of interest and then move it to track the region over the sequence of exposure images. This can be found in section 4.3.2.
- Step 3: Obtain the motion signal from the moving window by plotting mean photon counts versus exposure number. This is described in section 4.3.3.
- Step 4: Extract the phase signal out of the motion signal. Use this to label exposure images and sort them into a set of temporal bins (commonly called phases). This is presented in section 4.3.4.
- Step 5: Reconstruct each temporal bin, presented in section 4.3.5.

Fig. 4.1 is an illustrative explanation of the proposed algorithm for gating a MARS scan. The example shown is of a live mouse, where the data is split into eight temporal bins.

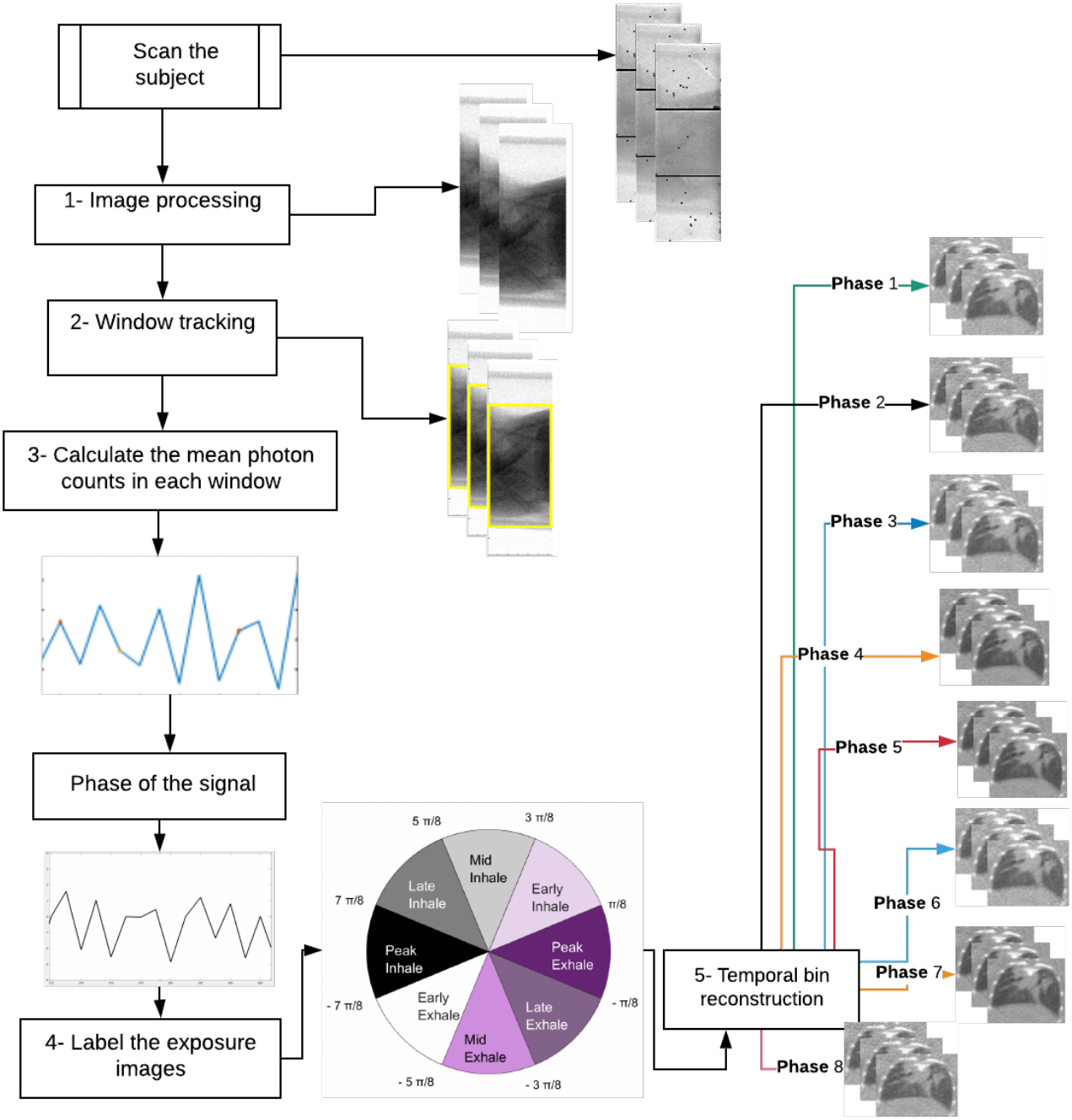

Figure 4.1: The steps in applying the motion tracking algorithm for the reconstruction of eight temporal bins. The process starts by scanning a subject with motion. The scan data is pre-processed in step 1. The detectors are shifted, and the gaps between detectors are removed to support step 2 when tracking a region of interest with motion. The motion signal is acquired in step 3 by plotting the mean photon count value of the region of interest versus the exposure image number. The motion signal's phase is used to label exposure images into eight temporal bins for reconstruction.

4.3.1 Step 1: Pixel masking, ring filtration, flatfield correction and inpainting

The MARS image processing toolchain is an automated set of image processing applications to process, reconstruct, and then quantify materials via decomposition. The first application performs some pre-processing including: pixel masking, flatfield correction, and ring filtration.

Malfunctioning pixels are defined as pixels that do not respond correctly to the presence of the X-ray photons. These pixels are to be masked before processing exposure images. Such pixels can have extreme values, which would distort any average calculations. Even if they do not have extreme values and are just noisy and jump around a bit, that behaviour can still reduce the relative strength of the motion signal against the background noise. In the case of breathing, the diaphragm moves a lot, but the top of the lungs and the ribs do not. If we want to pick up a subtle motion even at those places, it is best to try to strip away any pixels that could distort the motion signal.

The flatfield correction tries to correct for inter-pixel variation in the detector along with the X-ray beam profile. The flatfielding correction process is performed by dividing raw measurements by flatfield data and optionally scales back to photon counts using the average counts in the air from the flatfield data. Flatfield exposures are acquired with the absence of a subject in the scanner with the same acquisition settings as the primary scan. For MARS scans, the typical number of flatfield exposures is identical to the number of exposure images acquired over 360 degrees of rotation. Further details about MARS flatfield correction are available in chapter 3 of the thesis by De Ruiter (2015).

A defective or miscalibrated detector can produce ring artefacts around the centre of the rotation. The MARS ring filter algorithm uses a set of 1D median filters to estimate and correct static errors over the scan. This algorithm can remove most of the ring artefacts. For complete details of this algorithm, refer to chapter 6 of the thesis by De Ruiter (2015).

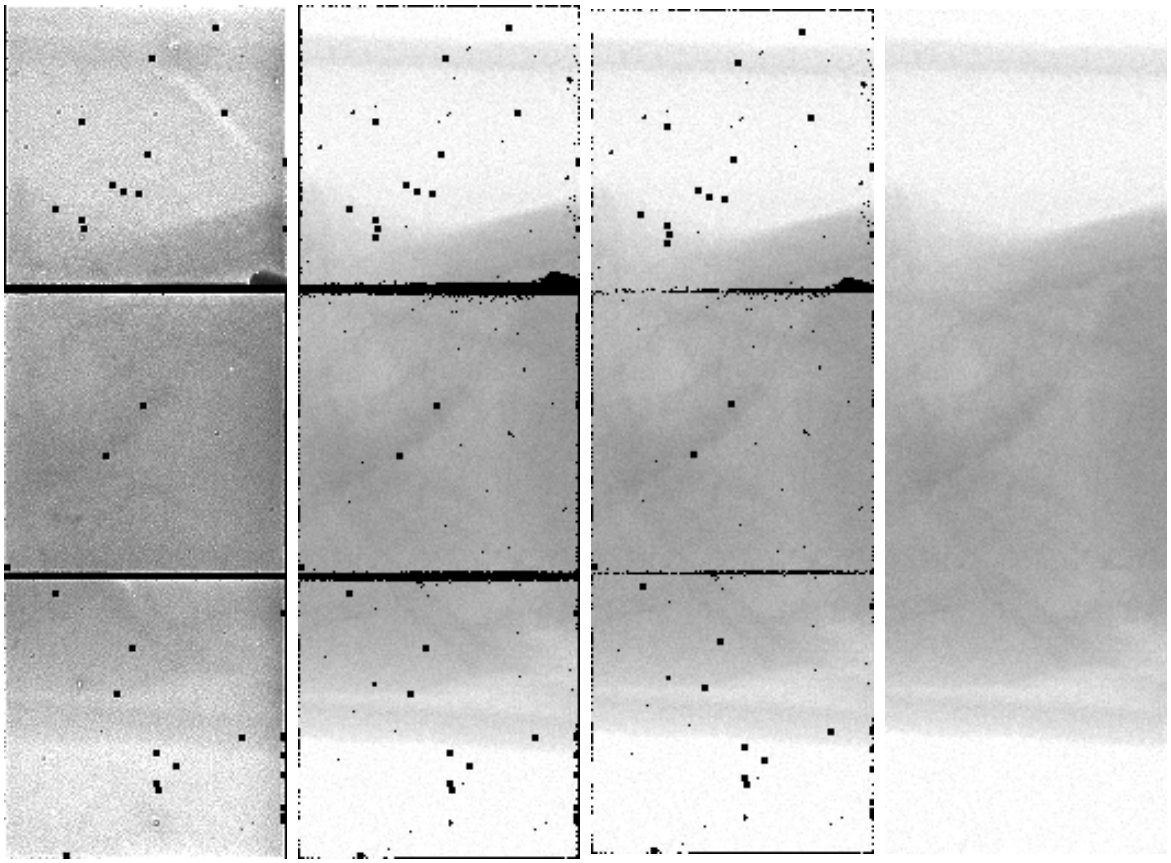

(a) (b) (c) (d)

Figure 4.2: An illustration of the processing steps on scan data on the live animal scan exposure image. The original exposure image is shown in (a). The result after applying applying flatfield correction, ring artefact, and pixel masking is given in (b). In (c), we have removed the detector gaps and artificially aligned the detectors. In (d) we have the final result after applying the inpainting algorithm on (c).

Fig. 4.2a shows an exposure image acquired from the live mouse scan. Fig. 4.2b shows the resulting image after applying the pixel masking, flatfield correction and ring artefact removal. The masked pixels have a value of zero and are shown in black.

To make processing easier, we want to extract 128 by 128 pixels from each detector. Afterwards, we artificially shift each detector so that they all start in the same column. Also, the row gaps between detectors are removed by placing the detectors directly next to each other. The number of rows that make up the gap we will call X_{G_p}. By removing missing data, depending on the number of the MARS detectors in the image,

N, a matrix with size N×128 rows and 128 columns will be generated for each exposure image. Fig. 4.2c shows an example of this process.

Inpainting is a method for compensating missing information based on its surrounding neighbours. Code was developed to inpaint the masked pixels. The algorithm is described in appendix A. This method locates and replaces such pixels with the closest good pixel of its predefined neighbours. This would result in a smooth image with no masked pixels left in it. Fig. 4.2d shows an example of the inpainted image.

4.3.2 Step 2: Automatically defining and tracking a region of interest

Large parts of the exposure data might be outside the subject or contain a non-moving rigid body. Adding those parts to the average would dilute the effect of the motion in the rest of the image. This reduces the sensitivity of the algorithm to motion in the subject. Therefore, a window that targets and tracks the moving regions should improve the accuracy of the extracted motion signal. In this section, we present an automatic method for tracking a moving edge of the subject over the exposures using a fixed window size.

The tracking algorithm requires the square pixel width (P_{size}) in millimetres, the diameter of the subject that the user sets for the scan (d) in millimetres and the magnification (m). The total number of rows X, and detectors D, covering the subject's shadow are computed in equation 4.1. The X value does not include the rows in the gaps between detectors. The width of the window is equal to equal to the number of columns C.

$$X \approx floor((\frac{d \times m}{P_{size}}) - (X_{G_p})) \tag{4.1}$$

$$Mx = (X - mod(X, 2)) + 2 \tag{4.2}$$

$$D = (\frac{Mx}{128}) \tag{4.3}$$

In the next stage, for the inpainted image with R rows and C columns, the average photon count along the superior-inferior direction (across the rows) is computed. The result is a 1D vector with R values; we call this vector A. Following that, the algorithm will locate the lowest value in A. The corresponding row that it belongs to will be labelled as the central row. The window that covers the subject is centred around the central row. Therefore, we rounded the value of X to its closest odd value (Mx), as shown in equation 4.2, to have (Mx/2) rows above the central row and (Mx/2) rows below the central row. The region of interest window then has a total height Mx+1. Fig. 4.3 shows an example of the central row tracking for placing the window around the moving subject.

For a camera with N detectors, the window size will consistently be (Mx+1) rows and 128 columns centred around the central row. In the case that the window will go past the boundary of the exposure image, the window will be translated so that it starts at the edge of the exposure. The size will remain the same.

In the final stage, the mean photon count will be calculated over the pixels in the placed window and saved in a vector with a value for each exposure image in the scan. This vector is called the z-axis profile and will be used for extracting the motion signal in the following step. The length of the z-axis profile array corresponds to the total number of exposures through the scan.

In this current region of interest tracking method, the window is designed to cover the whole subject so that it includes moving edges e.g. the diaphragm. This method may be further improved if the region of interest were designed in a way that only covers the moving edge and its neighbouring areas. The size and shape of the region of interest may also have an effect on the acquired motion signal. Therefore, in future studies, we aim to develop some methods for more precisely tracking the moving edge in the image.

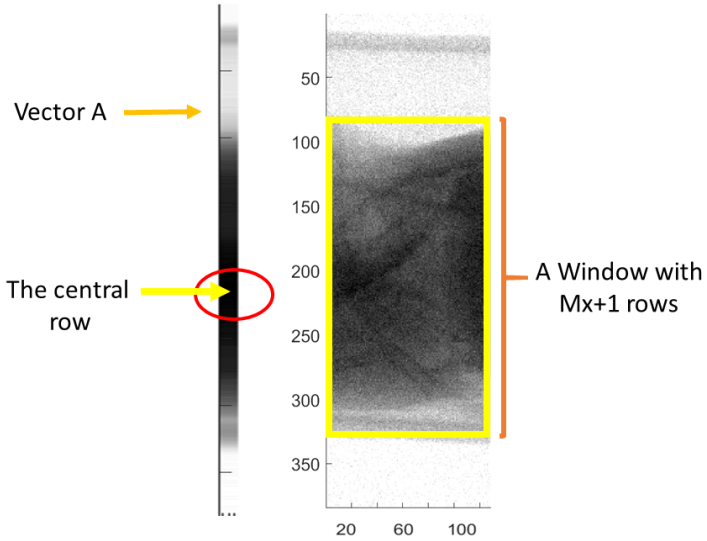

Figure 4.3: This figure shows the computed pixel mean value along the rows for targeting the central pixel on the left of the image. The figure on the right shows the placed region of interest window placed around the central row with Mx+1 rows and 128 columns.

4.3.3 Step 3: obtaining the motion signal

The motion in the scan can be split into two sources, the subject and the gantry. The z-axis profile vector (Z), that was introduced in the previous section, is a 1D vector incorporating the fast and slow movements in the whole scan. In equation 4.4, Z(t) represents the amount of motion-related distortion induced in the exposure image at time t. $S(t)$ is a function of slow movements, such as the scanner gantry rotation, and $F(t)$ is the function of fast movements, such as respiration. In equation 4.4, the unit of time is the exposure number. The distinct difference in the frequency of fast and slow components provides an opportunity to remove the slow varying movements from the overall motion Z(t). Removing slow movements from the global motion signal can be done by subtracting the $Z(t)$ signal from a smoothed version of itself resulting in the motion from the subject.

$$F(t) = Z(t) - S(t) \sim= Z(t) - smooth(Z(t)) \tag{4.4}$$

In our case, the $Z(t)$ signal is smoothed via a robust linear regression smoothing function 'RLOWESS' in MATLAB (The Mathworks, Inc. (2017)). Further information about this method is obtainable in the following reference by Cleveland (1979).

4.3.4 Step 4: Amplitude or phase binning for sorting

Once F(t) is acquired, the next step is computing the motion signal's phase and amplitude. The phase and amplitude from a motion signal by applying an analytical signal approach, further details can be found in chapter 4 of a book by Smith (2007). To start with, the Hilbert transform is applied on F(t) to derive the complex counterpart of the signal, Im(t). The analytical signal, R(t) is defined by complementing the F(t) with Im(t), as shown in equation 4.5. Schumann *et al.* (2010) reported for getting a robust phase and amplitude based on analytical signal approach, the motion signal should oscillate around zero. The phase and amplitude signal calculations of the R(t) are shown in equations 4.7 and 4.6 respectively. An example of the amplitude and phase of the live scan motion signal are presented in Fig. 4.4.

$$R(t) = F(t) + iIm(t) = A(t)e^{i\phi(t)} \tag{4.5}$$

$$A(t) = \sqrt{F(t)^2 + Im^2(t)} \tag{4.6}$$

$$\phi(t) = \tan 2\{F(t), Im(t))\} \tag{4.7}$$

Exposure images can be classified and sorted into temporal bins either based on the phase or the amplitude of the signal. Sorting based on the amplitude can result in more severe streaking artefacts compared to phase binning in 4D cone beam CT (T O'Brien *et al.*, 2014). Bartling *et al.* (2010) reported that the the low and high frequency jitters in the motion signal usually have less disturbance on phase based gating. The reconstructed volumes based on the phase signal have been shown to have a more reliable performance over amplitude binning (Fitzpatrick *et al.*, 2006). Becker *et al.* (2013) also reported that the reconstruction of the motion extremes in the exhale and the inhale phase was successful in phase binning while amplitude binning failed.

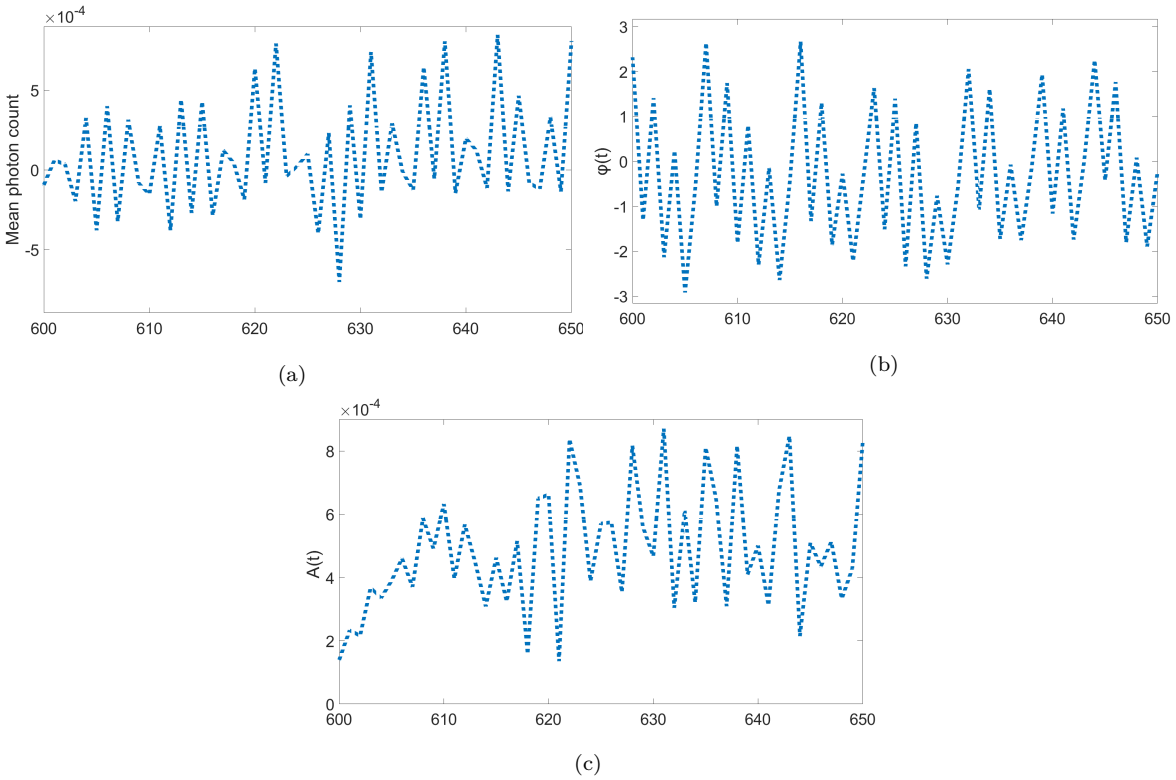

Figure 4.4: The presentation of the motion signal's phase and amplitude extracted from the mouse scan for 50 consecutive exposures. The motion signal F(t) is shown in (a). The phase signal $\phi(t)$ is illustrated in (b). The amplitude signal A(t) is shown in (c). The phase signal oscillates between -pi and pi. The x axis in all three figures is the number of exposure images.

In the developed algorithm, by considering the discussion and results obtained in the literature, we decided to apply temporal binning based on the phase signal for labelling the exposure images. To produce N temporal bins in a MARS scan, the phase signal $\phi(t)$ can be divided into N sections, each with an equal width of $2\pi/N$. Table 4.1 shows the phase assigning process for sorting the phase signal, $\phi(t)$ into two, four and eight equi-spaced temporal bins. The eight bin breathing phase labelling is performed based on the bins introduced by Vedam *et al.* (2002). Depending on the number of temporal bins requested by the user, the algorithm will calculate each exposure image's phase category and sort the exposure image to the corresponding temporal bin folder. For N temporal bins there will be N folders containing the labelled exposure images. Each temporal bin will then be reconstructed individually by running the in-house MARS iterative reconstruction algorithm. A text file is generated from the motion gating

algorithm, which contains the phase angle of each exposure image in radians for the entire dataset.

Table 4.1: Dividing a phase signal into two, four and eight equi-spaced temporal bins.

	8 bins	Phases	4 bins	Phases	2 bins	Phases
Phase 1	$\frac{-1\pi}{8} : \frac{1\pi}{8}$	Peak exhale	$\frac{1\pi}{8} : \frac{-3\pi}{8}$	Peak exhale	$\frac{1\pi}{8} : \frac{-7\pi}{8}$	Exhale
Phase 2	$\frac{-1\pi}{8} : \frac{-3\pi}{8}$	Late exhale	$\frac{-3\pi}{8} : \frac{-7\pi}{8}$	Mid exhale	$\frac{-7\pi}{8} : \frac{1\pi}{8}$	Inhale
Phase 3	$\frac{-3\pi}{8} : \frac{-5\pi}{8}$	Mid exhale	$\frac{-7\pi}{8} : \frac{5\pi}{8}$	Peak inhale	-	-
Phase 4	$\frac{-5\pi}{8} : \frac{-7\pi}{8}$	Early exhale	$\frac{5\pi}{8} : \frac{1\pi}{8}$	Mid inhale	-	-
Phase 5	$\frac{-7\pi}{8} : \frac{7\pi}{8}$	Peak inhale	-	-	-	-
Phase 6	$\frac{7\pi}{8} : \frac{5\pi}{8}$	Mid inhale	-	-	-	-
Phase 7	$\frac{5\pi}{8} : \frac{3\pi}{8}$	Late inhale	-	-	-	-
Phase 8	$\frac{3\pi}{8} : \frac{1\pi}{8}$	Early inhale	-	-	-	-

4.3.5 Step 5: Reconstruction

The MARS reconstruction software uses an iterative reconstruction algorithm developed in-house. This algorithm takes pre-processed exposure images (see section 4.3.1). The pixel counters in the raw scan data represent the number of photons detected over an energy range from the counter threshold to the common kVp of the X-ray source. This means that the energy ranges of the counters overlap e.g. photon counts over 15-120 keV, 45-120 keV, 55-120 keV, and 65-120 keV for four counters. The reconstructed attenuation volumes represent the effective linear attenuation for narrow energy ranges between these thresholds. They are adjacent to each other and non-overlapping e.g. 15-45 keV, 45-55 keV, 55-65 keV, and 65-120 keV for four attenuation volumes matching the counters in the example above. A low-resolution polychromatic Beer-Lambert law makes the link between attenuation volumes and the pixel counters (De Ruiter *et al.*, 2017). We used the in-house MARS reconstruction software individually for each temporal bin. In this case, as the gating process simply divides the data into different subsets, no further changes are required to the reconstruction algorithm.

4.4 Evaluating the quality of the reconstructed images.

A number of image quality measurements can be applied on the motion-gated and non-gated reconstructed volumes to evaluate the effect of implementing our gating algorithm. Among these methods, difference images and noise measurements such as the contrast to noise ratio (CNR) and the signal to noise ratio (SNR) have been applied on the reconstructed live mouse dataset. The evaluation metrics were applied to each of these reconstructed datasets.

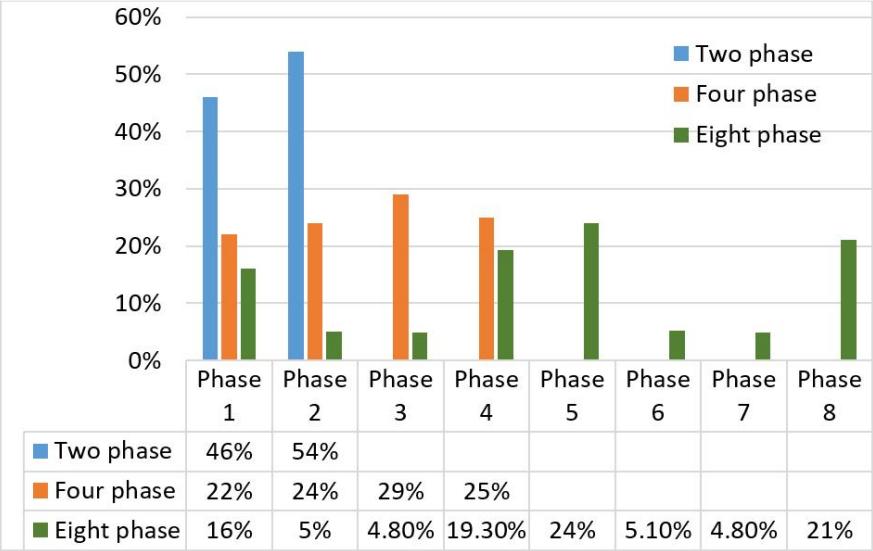

	Phase 1	Phase 2	Phase 3	Phase 4	Phase 5	Phase 6	Phase 7	Phase 8
Two phase	46%	54%						
Four phase	22%	24%	29%	25%				
Eight phase	16%	5%	4.80%	19.30%	24%	5.10%	4.80%	21%

Figure 4.5: The percentage of the exposure images that were sorted into two, four and eight temporal bins for reconstruction. For each condition (two, four, or eight bins), sorting the exposure data into temporal bins is exclusive, so each exposure image is placed into just one temporal bin. Therefore, this process reduces the data available for each reconstruction.

Together with the two, four, and eight temporal bin case, a reconstruction without any gating was also performed. The percentage of exposure images sorted into each temporal bin is presented in Fig. 4.5. A reconstructed slice of the non-gated data is shown in Fig. 4.6. Reconstructed slices for two, four and eight temporal bins are given in Fig. 4.7, 4.8 and 4.9 respectively. The evaluation metrics were applied to each of these reconstructed datasets.

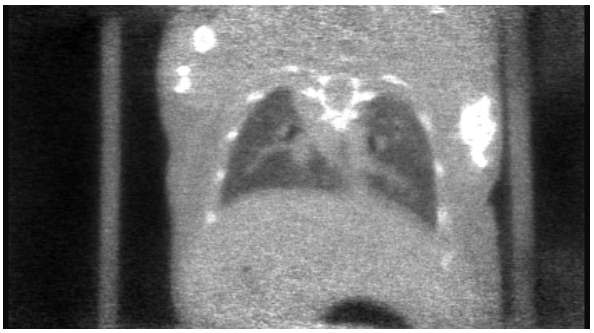

Figure 4.6: A reconstructed slice of non-gated data. This figure has blurry edges around the diaphragm. This image is reconstructed with all available exposure images.

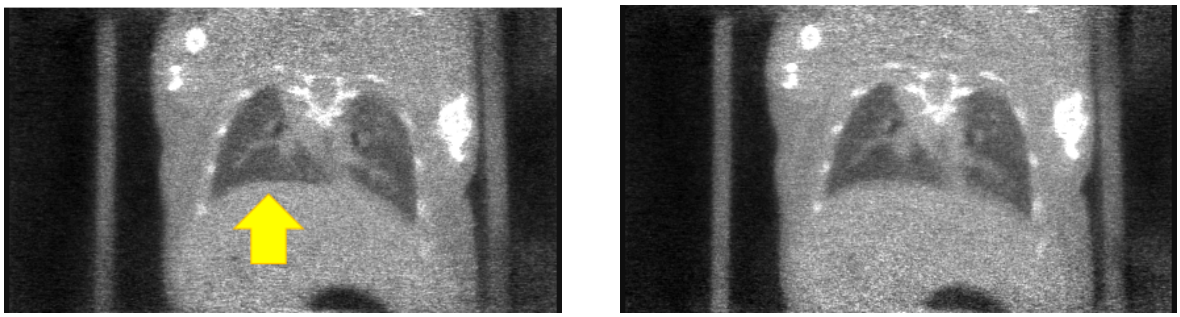

(a) (b)

Figure 4.7: A comparison of the quality of the reconstructions of the gated data in two temporal bins. A reconstructed slice of phase 1 (exhale) to 2 (inhale) are shown in (a) and (b) respectively. The diaphragm in (a), in the left lung has the more distinct edges compared to inhale phase in (b).

The two-phase reconstructed images are shown in Fig. 4.7. The exhale phase has sharper edges in the diaphragm area compared to the inhale phase. The inhale phase has blurry edges around the diaphragm area. Some sharper vessels in the lung are also visible in the exhale phase (a), compared to the non-gated and inhale phase (b). The noise contents of the exhale phase and inhale phase appear to be higher compared to the non-gated slice shown in Fig. 4.6, which looks smoother. This is to be expected as the reconstruction of phase 1 and phase 2 was performed using only around 50% of the exposure images.

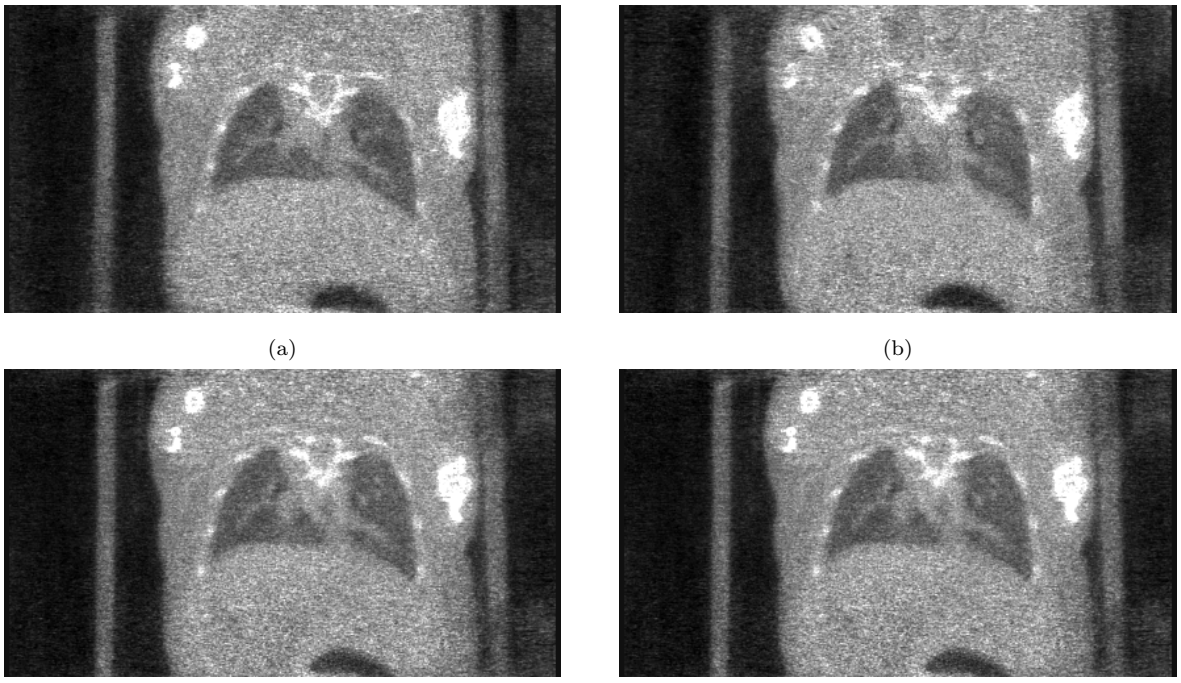

(a) (b)

(c) (d)

Figure 4.8: A comparison of the quality of the reconstructed data of the gated data in four temporal bins. Phases 1 to 4 (peak exhale, mid exhale, mid inhale, and peak inhale) in the gated dataset are shown in (a) to (d) respectively. All phases are reconstructed with around 25% of available exposure image and have similar image quality. Phases 1 and 3 have the sharpest edges.

The reconstructed slices for the four-phase images are shown in Fig. 4.8. The noise content of all four phases gated slices are higher compared to gated slice from two phases presented in Fig. 4.7, as they are reconstructed with almost one-fourth of the available exposure images. The diaphragm is sharper in phase 1 compared to the three other gated temporal bins.

The eight-phase temporal bins are illustrated in Fig. 4.9. The obvious reduction of the image quality by increasing the temporal bins number from two to eight, is quite distinctive. For example, the poor image quality of Fig. 4.9b, phase 2 of eight breathing phases is due to having only 5% of the available data. In contrast, Fig. 4.9e, which is reconstructed with 24% of the available data, shows more structures in the lungs to look at.

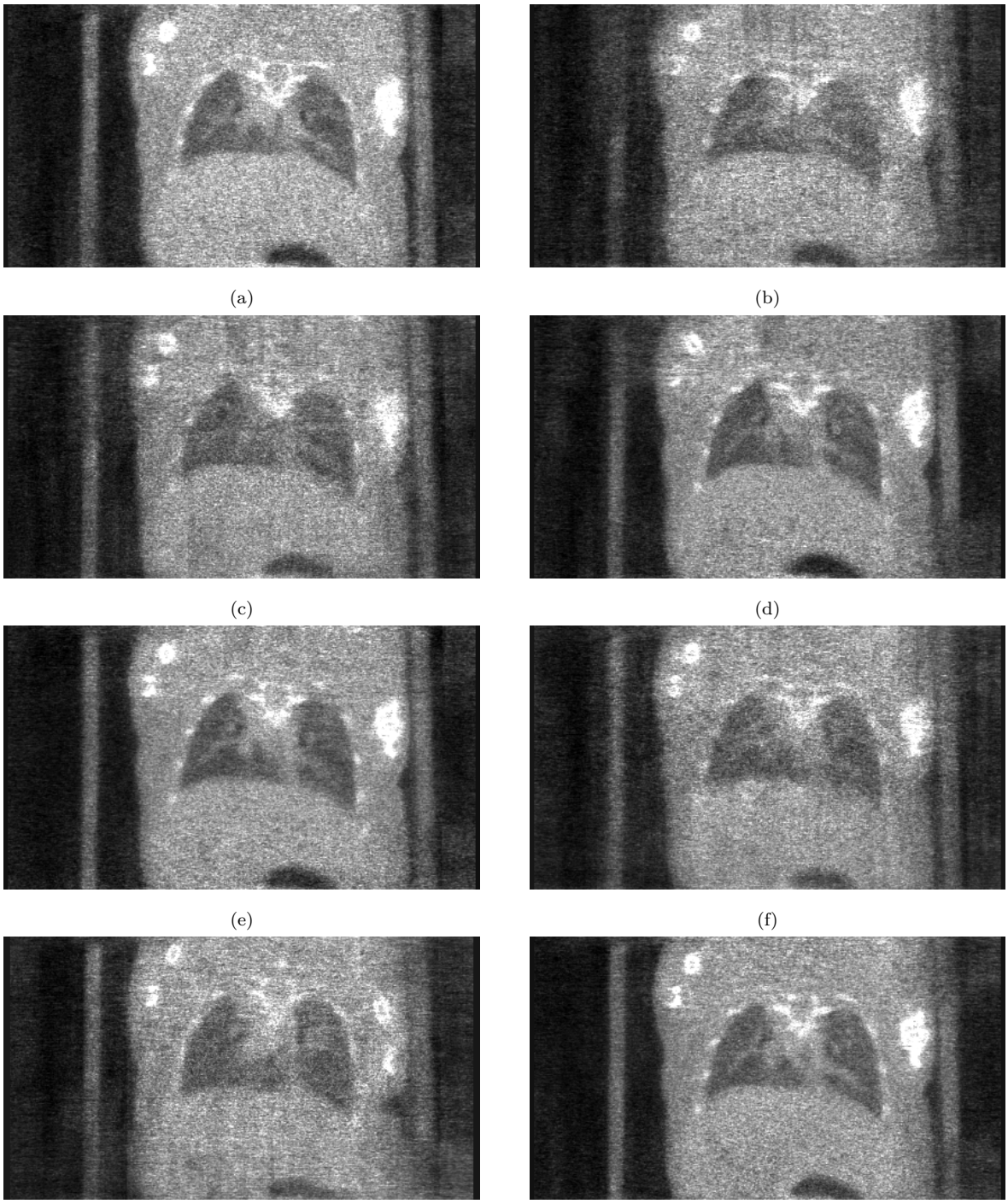

(a) (b) (c) (d) (e) (f) (g) (h)

Figure 4.9: A visual comparison of the quality of the reconstructions of the gated data in eight temporal bins. Phases 1 to 8 (peak exhale, late exhale, mid exhale, early exhale, peak inhale, mid inhale, late inhale, and early inhale) are shown in (a) to (h) respectively. Sorting the exposure images into eight temporal bins has reduced the image quality and increased the noise contents in reconstructed dataset in some bins. Some examples are shown in (b), (c), (f) and (g) which are reconstructed with only 5% of the available exposure images.

We have produced videos of the breathing cycle using live mouse scan data. These are shown using the coronal view by packing slices of all the temporal bins into the ImageJ (Rasband, W.S., ImageJ, U. S. National Institutes of Health, Bethesda, Maryland, USA) program. Here is the link to all three videos: two-phase video[1], four-phase video[2] and eight-phase video[3].

To create these videos, the scan data was packed into two, four and eight reconstructed temporal bins. The time frame in these videos is the number of temporal bins. In ImageJ, it is also possible to cycle between energy and coronal slices while the video is playing. In these videos, the slider C shows the energy bins. Slider Z is used for scrolling through the slices.

By increasing the temporal bins from two to eight, the transitions of the lung in breathing turn out to be more smooth. In two temporal bins, the movement is sharp and sudden; the diaphragm edge is a sharp edge in phase one and a doubled edge in phase two. While in the four temporal bin movie, the transitions are smoother, and finally, in eight temporal bins, the breathing phases are nice and smooth. The poor quality of most time frames in the eight bins case does make it difficult to know if the subtle motion in the upper portions of the lung are real or not. Given the poor quality, we did not try reconstructing more than eight temporal bins. Consequently, our question remains on how we could improve and measure the quality of this method.

4.4.1 Difference images

Difference images were acquired by computing the absolute value of the subtraction of the peak two images to be compared (in our case, this will be the peak exhale, and the peak inhale phases). This is a qualitative method of visual inspection. The difference can come from various sources such as motion, ring artefacts and noise. We expect to see a higher amount of difference in the areas that are prone to motion, such as the diaphragm in the case of breathing.

[1] https://youtu.be/eZRW4fC7_hc
[2] https://youtu.be/XyxKeNRWN6U
[3] https://youtu.be/dkM39dPF4rQ

Fig. 4.10 illustrates the difference image in the two phase case. As we were expecting, the region around the diaphragm has a white band, which highlights the presence of the motion. However, some areas with the bone are also highlighted in white. That could be due to the reconstruction algorithm, which uses a multiplicative correction factor against the current value of the voxel. This means that high-density voxels will have higher noise components than low-density voxels. Higher noise will result in brighter areas in the difference image.

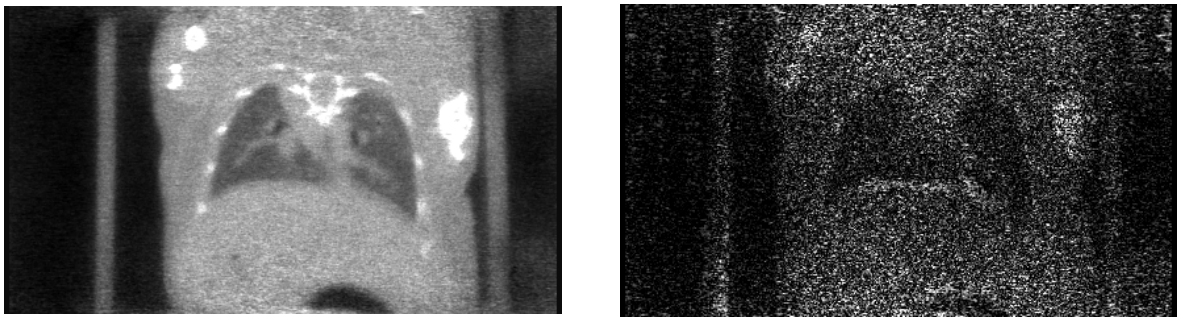

(a) (b)

Figure 4.10: The difference image acquired from the gated data in two temporal bins. The non-gated slice and the difference image are shown in (a) and (b) respectively. In the difference image (b), the diaphragm region is highlighted in white, emphasising the transition of the diaphragm from the exhale phase to the inhale phase. This white region corresponds to the diaphragm blurred region in the non-gated image. The bone areas are also highlighted.

The difference results for the four-phase case is shown in Fig. 4.11. The highlighted area in white is the diaphragm with the motion. Some areas with the bone are also highlighted in white. To test our hypothesis that the bright areas in bone are due to noise, and not motion, we can further process the difference images. We first compute the difference of each two consecutive phases; the difference in phases 2 and 1, phases 3 and 2, phases 4 and 3, and phases 4 and 1. Next, these difference images are summed together. This should show the similarity between these difference images and is shown in Fig. 4.11c. In the summed difference image the bones are area highlighted in white. This means the differences in the bone area areas are consistent over all phases. In contrast, the diaphragm area is reduced as the motion changes over the phases and cancels out. To suppress the subject's structures, we divided the peak difference image

by the summed difference image to get what we call the motion structure image shown in Fig. 4.11d. In this image, the diaphragm region is highlighted in white but the rest of the structure is gone. This supports our hypothesis that the bones in the original difference image should be the result of heightened noise and not motion. It is also evidence that the diaphragm is influenced by motion.

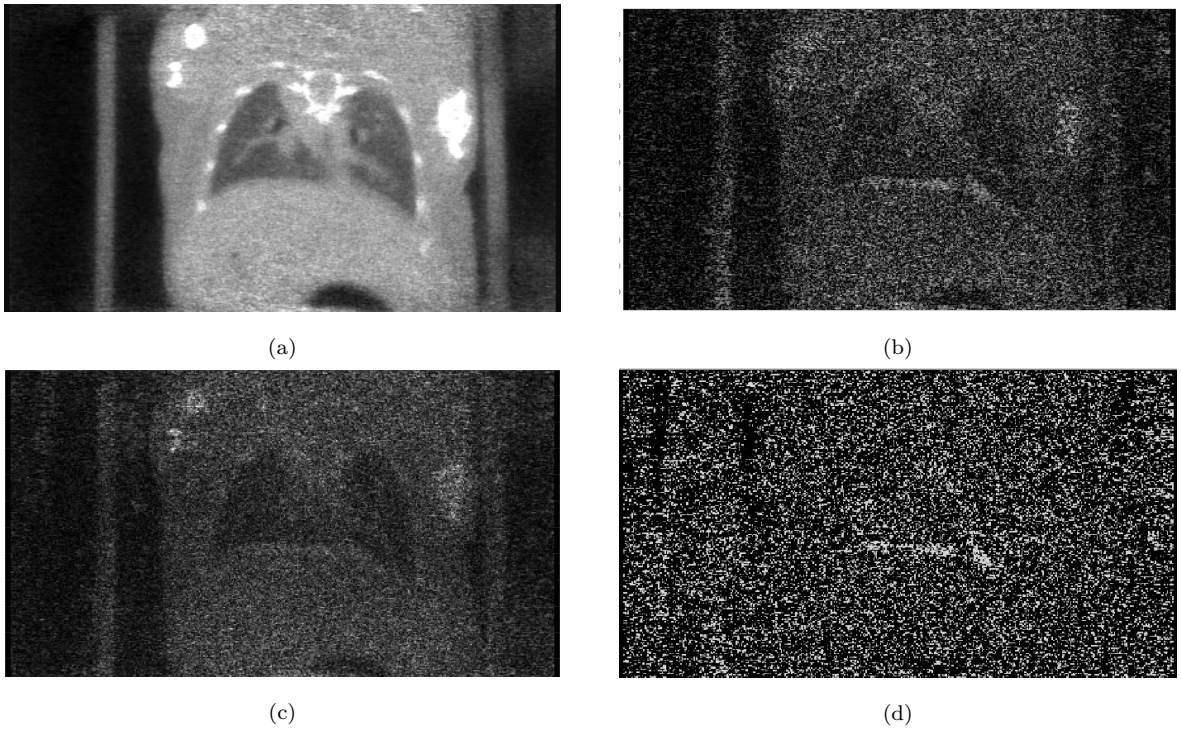

(a) (b) (c) (d)

Figure 4.11: An illustration of studying difference images on four phases of the live mouse dataset. The non-gated image is shown in (a). The peak difference image is shown in (b). The summed difference image acquired by summing every consecutive phases difference is given in (c). The summed image shows similar structures between all difference images. The extracted motion from the image is shown in (d); it is obtained by dividing the (b) by (c).

The peak difference image acquired for the eight phase case is shown in Fig. 4.12b. Fig. 4.12c shows the summed difference images acquired by summing each consecutive difference image to show the similarity between all difference images. The motion structure image is demonstrated in Fig. 4.12d. The results in the eight phase case match those observed in the four phase case.

In summary, the difference images prove that we were capable of detecting and extracting motion. As expected, the motion mostly presented itself around the diaphragm region. However, it is obvious that the current approach, which reduces the amount of data available for each temporal bin, has a heavy impact on image quality. Having a reconstruction algorithm that uses all the exposure images for reconstructing the temporal bins will help in increasing the quality of the images.

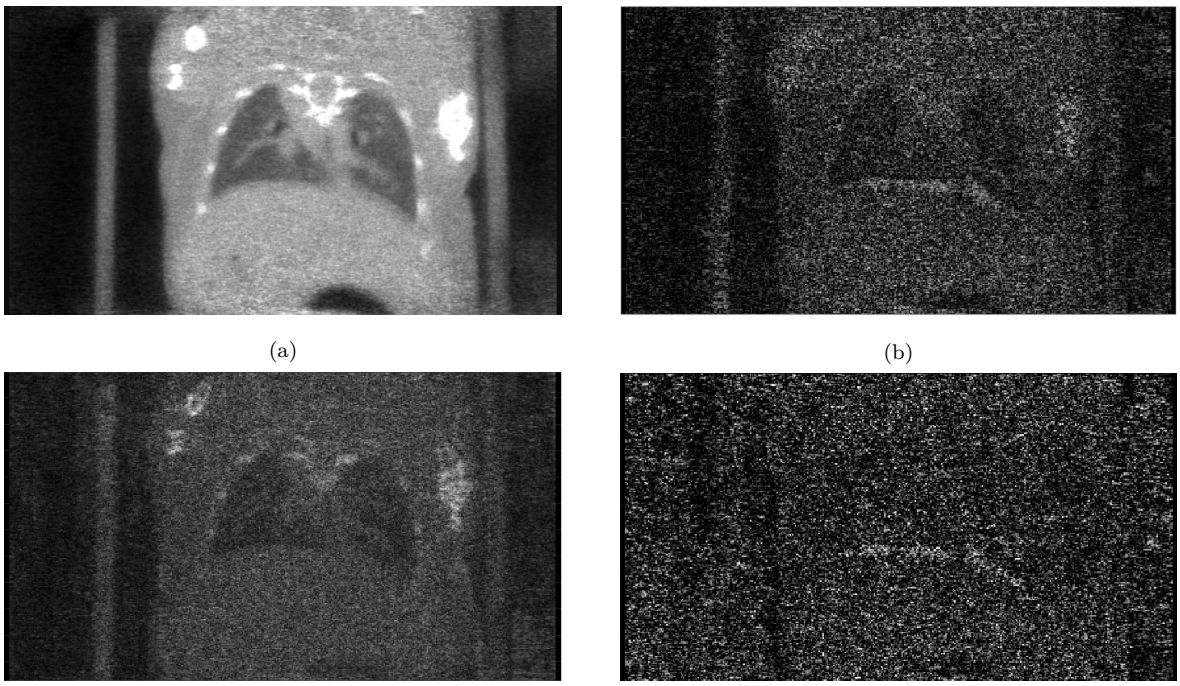

(a) (b) (c) (d)

Figure 4.12: An illustration of the study of difference images on eight phases of the live mouse dataset. The non-gated slice is presented in (a). The peak difference between the peak exhale and the peak inhale from eight temporal bins is shown in (b). The summed difference image is shown in (c) which is the summation of all consecutive phases difference images. The extracted motion structure from the image is given in (d). The motion is highlighted as white regions around the diaphragm.

4.4.2 Noise measurements

SNR and CNR values are mathematically delineated in equations 4.8 and 4.9 respectively. To calculate the standard deviation (σ), and mean (μ), five circular regions of interests (ROIs) within one slice were manually drawn over an area of 225 pixels and

then averaged. Several slices were used for computation of the SNR and CNR. The region of interest includes the lung tissue (ROI 1), the diaphragm tissue as soft tissue (ROI 2), and an air region (ROI 3) outside the sample (as background). These are demonstrated in Fig. 4.13. The ROIs were drawn away from the lung and diaphragm boundary to prevent slight errors in measurements.

$$SNR = \frac{\mu(lung)}{\sigma(lung)} \tag{4.8}$$

$$CNR = \frac{(\mu_{diaphragm} - \mu_{lung})}{\sigma_{air}} \tag{4.9}$$

High noise content leads to a low CNR and SNR and reduces the detectability of the structures. We are expecting the CNR and SNR of the gated volumes to be less than the corresponding values of the non-gated dataset as they are reconstructed with a fraction of the available exposure images, depending on the total number of temporal bins. What we want to know is by how much the signal and contrast is reduced relative to the noise. How much are these two are affected by the number of exposure images contributing to the reconstructions.

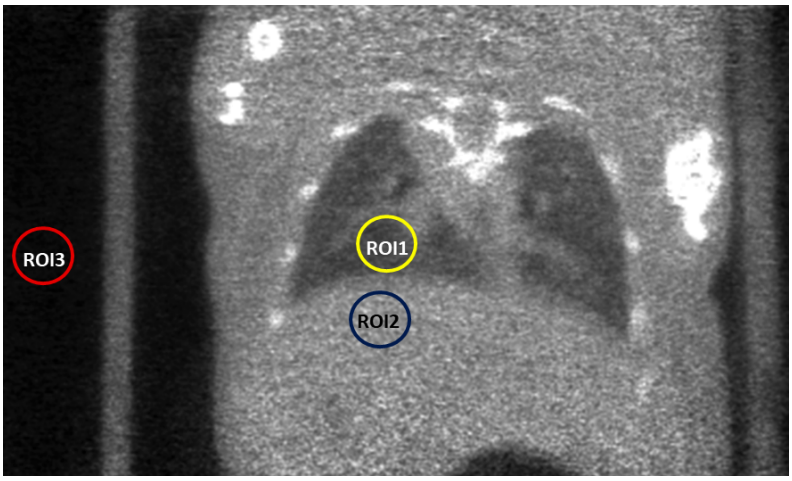

Figure 4.13: The drawn ROIs for calculating SNR and CNR ratio.

The measured SNR and CNR for the non-gated data were 9.73 and 22 respectively. Fig. 4.14 illustrates the measured results for two, four and eight temporal bins respectively along with the percentage of total exposure images contributing to the reconstruction

of each temporal bin. Table 4.2 shows the percentage ratio of SNR of each temporal bins to SNR of the non-gated dataset.

By comparing the gated and non-gated reconstructed volumes, a linear reduction in SNR and CNR is observed. The lowest SNR and CNR belonged to phase 2, 3, 6 and phase 7 from the eight temporal bins, which had used down to 5% of the available exposure images used for reconstruction. While the highest figures belong to phase 2 of two temporal bins with almost 50% of the available exposure images contributing to the reconstruction of the phase.

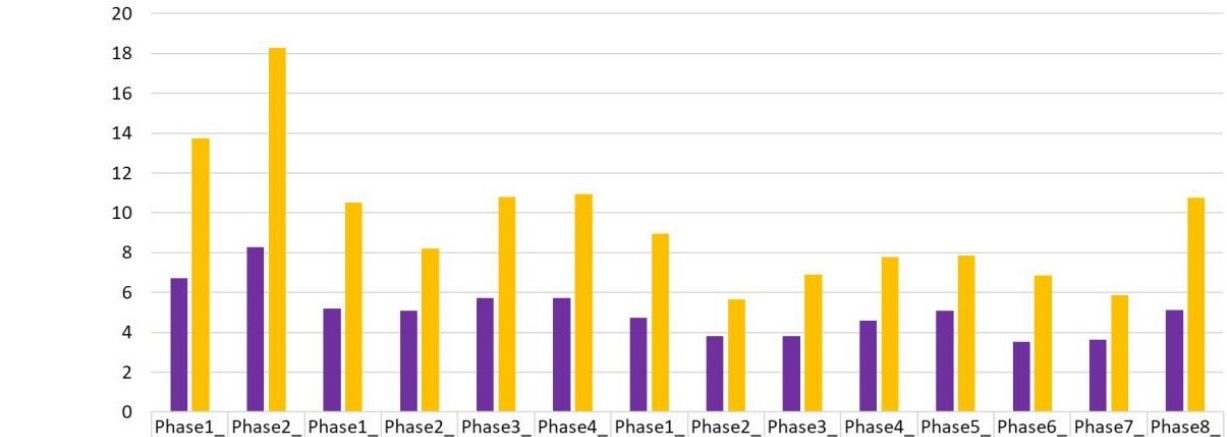

	Phase1_2	Phase2_2	Phase1_4	Phase2_4	Phase3_4	Phase4_4	Phase1_8	Phase2_8	Phase3_8	Phase4_8	Phase5_8	Phase6_8	Phase7_8	Phase8_8
SNR	6.73	8.28	5.2	5.08	5.71	5.72	4.72	3.79	3.8	4.6	5.09	3.54	3.62	5.13
CNR	13.73	18.27	10.5	8.2	10.8	10.93	8.94	5.66	6.88	7.78	7.84	6.84	5.88	10.75
Contribution%	46%	54%	22%	24%	29%	25%	16%	5%	5%	19%	24%	5%	5%	21%

Figure 4.14: SNR and CNR measurements for the two, four and eight temporal bins along with the percentage of exposures that contributed. The increasing number of temporal bins from two to eight has further reduced the measured SNR, CNR and the percentage of contributing data. Phase 2 out of two temporal bins has the highest SNR and CNR with the contribution of 54% of exposure images for the reconstruction of it. While the lowest values belong to phases 2, 3, 6, and 7 out of eight temporal bins reconstructed with almost 5% of exposure images.

The results from Table 4.2 shows that by doubling the number of temporal bins from two to four, there is a minimum of 13% and a maximum of 36% reduction in the SNR ratio of the gated to the non-gated data. By doubling the exposure images from four to eight a maximum of 19% and a minimum of 5% reduction in the ratio of the SNR

value of the gated to the non-gated data.

Table 4.2: The percentage of (SNR phase/SNR non-gated) for two, four, and eight temporal bins

	Two bins	Four bins	Eight bins
% of (SNR phase 1/SNR non-gated)	69%	53%	48%
% of (SNR phase 2/SNR non-gated)	88%	52%	38%
% of (SNR phase 3/SNR non-gated)	-	58%	39%
% of (SNR phase 4/SNR non-gated)	-	58%	47%
% of (SNR phase 5/SNR non-gated)	-	-	52%
% of (SNR phase 6/SNR non-gated)	-	-	36%
% of (SNR phase 7/SNR non-gated)	-	-	37%
% of (SNR phase 8/SNR non-gated)	-	-	52%

4.5 Summary

- Motion artefacts deteriorate the quality of reconstructed slices by inducing blurring and double edges.
- Direct and automatic extraction of the motion signal from the exposure images simplifies the acquisition since no extra instrumentation is needed. This reduces the number of signals that need to be acquired and analysed.
- An image-based gating algorithm that uses the average photon counts was developed for MARS datasets.
- A windowing algorithm that targets and tracks regions with motion was developed and described.
- A motion signal was acquired by plotting the mean photon counts within the window against exposure number. The low-frequency components (assumed to be scanner motion) were removed, leaving the motion of the subject.
- The exposure images were sorted into separate temporal bins. In the evaluation using a live mouse scan, this included two, four, and eight bins of the mouse's

breathing cycle.

- Evaluation metrics, including difference images and noise measurements were applied to the results of a live mouse scan.
- Results of the evaluation demonstrated the mitigation of motion in some reconstructed temporal bins such as exhale phases.
- The high noise content of phases that contain a low fraction of original exposure images caused streaking artefacts and increased noise.

Chapter 5

Evaluation of the gating method with motion phantom data

In this chapter, we investigate the performance of applying the gating algorithm from chapter 4 on varying amounts of movement. To simulate motion, a motorised motion phantom was designed and manufactured. This chapter also presents a solution to the issue of undersampling in temporal bins observed in chapter 4.

This chapter first starts with the design and development of a motion phantom to test the gating algorithm in section 5.1. Section 5.2 describes a phase-weighted reconstruction algorithm to improve the image quality of temporal bin volumes. Section 5.3 presents the results of applying the gating algorithm on the motion phantom data. The results of applying two quantitative metrics on the motion phantom data are presented in section 5.4. A summary concludes the chapter in section 5.5.

5.1 Multi-contrast motion phantom

A motorised motion phantom was designed and manufactured to produce controlled periodic motion. The goal was to use the scan of the motion phantom to quantitatively evaluate the intrinsic gating algorithm developed in chapter 4.

This phantom can be programmed to generate known periodic signals. It provides advantages, such as consistency and control over the size of the movement. A motion phantom also does not require ethics approval.

The motion phantom will be a substitute for soft tissues. Therefore, the materials of the phantom should have attenuation properties similar to soft tissue. Acrylic Poly methyl methacrylate (PMMA) is a common soft-tissue/water-equivalent material used in phantom studies. It has comparable mass attenuation, absorption coefficient and effective Z atomic number to water (Ferreira *et al.*, 2010).

We want to be able to test the effect of motion on material decomposition (MD). Therefore, it would be good if we could support adding a range of materials to the phantom. The designed motion phantom mounts a standard 'spectral phantom' to a motorised unit. The spectral phantom is a perspex holder (PMMA) that can have vials of substances added to it. Later the scan data can be used to study how MARS-MD is influenced by motion and the different amplitudes of the motion.

Furthermore, it can be used to generate different amplitudes to study the performance of the gating algorithm from chapter 4 on various movements. The goal is to program the phantom to have various amplitudes to simulate different motion conditions. From amplitude of a mouse breathing to human breathing for an example. Therefore, it will enable us to perform more quantitative tests. This will also provide us with an opportunity to investigate how gating algorithm will be influenced by the amplitude of the motion.

Hegazy *et al.* (2017) reports that subject movement that is parallel to the detector plane to have more substantial motion blurring effects. Therefore, we designed the phantom's arm to move forwards and backwards in the z-axis direction.

The motion phantom is programmed with a sine function to simulate simple periodic motion. A user sets the frequency, period, and amplitude of the motion phantom. Fig. 5.1 displays the motion phantom and its connection set up with a PC and an Arduino board (Arduino (2019)).

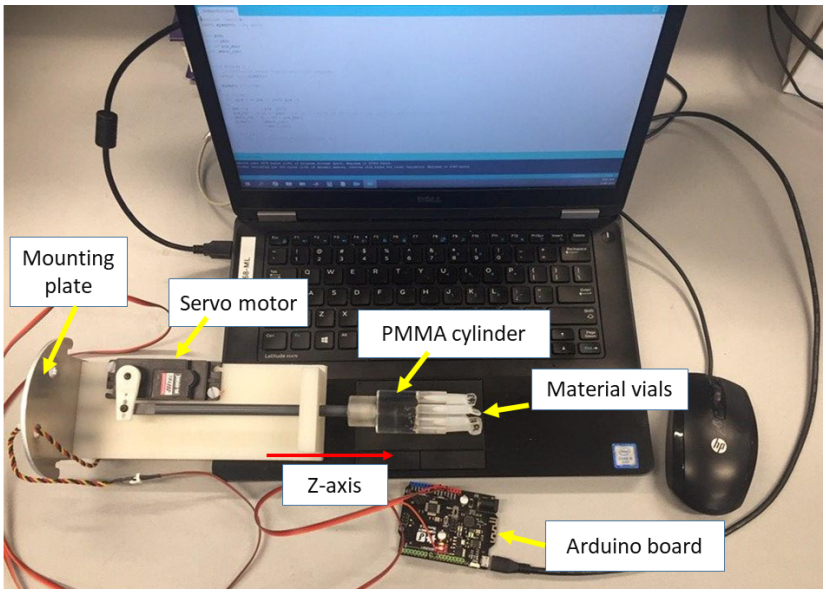

Figure 5.1: A multi contrast motion phantom setup with a PC and a controlling board.

The designed motion phantom is comprised of two parts: a movable part and control electronics. The movable section is placed within the scanner for imaging, while the control electronics are placed external to the scanner. The movable section is a PMMA cylinder with a diameter of 31 mm. Nine built-in 6 mm capillary tubes are included. This means that we can insert sealed 200 uL Eppendorf vials (which can contain solutions of different materials).

An HS-805BB servo motor is connected to the perspex via a plastic arm to produce linear 1D motion. The servo is mounted on a plastic rectangular plate that is connected to a customised sample holder adapter plate. A hole is in the adapter to conveniently connect the servo motor directly to an Arduino board.

A Bluno M0 unit model ARM Cortex-M0 is a micro-controller is used to control the servo motor functionality. The Arduino unit gets connected to a PC for power and controls the movements via a USB to serial adapter.

5.2 A weight-based reconstruction algorithm

By classifying the exposure images into several temporal bins, the number of exposures in each temporal bin will be a fraction of the total available. Depending on the selected number of temporal bins, the percentage of exposure images sorted into each bin may differ. Meaning that, in two-phase reconstructions, each phase would have approximately 50% of the total exposure images, while in eight temporal bins a phase may have less than 5% of the total images. The negative impact of this was clear in the results presented in chapter 4.

To improve the quality of the reconstructed images for all temporal bins, we found a solution by requiring a minor change to the reconstruction algorithm. Instead of sorting the exposure images into independent temporal bins, the improved method employs all the exposure images but applies a weighting factor to each.

The weighting factor uses the distance between a target phase angle of the temporal bin (selected by the user) and the predicted phase angle (by the algorithm) for each exposure image. The weight function used in this method is presented in equation. 5.1:

$$W = \epsilon + e^{-\alpha|d|} \tag{5.1}$$

In the equation presented, W, is the weight term and d is the normalised distance term (-1$\leq d \leq$1) between the estimated phase angle of each exposure and the target phase angle to be reconstructed[1]. In the range of d, a value of -1 or 1 corresponds to the target and predicted phase angles being 180 degrees apart.The exponential term reduces the effect of longer distances. The speed of decay (α) was experimentally chosen to be 15. A small offset term (ϵ) ensures that no weight will ever be zero (we used 0.001).

This equation is still preliminary and could be improved upon. In the future, a better approach may base this value on the amount of data available around the target phase

[1]This means that the algorithm tries to reconstruct a single phase angle as opposed to a discrete range

angle (more data means that we can use a larger value for the same image quality and vice versa). Time prevented testing changes to the equation during this thesis. However, it will be included in a manuscript in preparation.

The reconstruction algorithm uses ordered subsets. A subset is defined as all the scan exposures within a 1-degree range of the gantry rotation as well as the corresponding 1-degree range 180 degrees away. The update to a voxel is a weighted average of all the correction terms from all pixels in the subset. The weighting factor from gating is now combined into this weighted average of the correction terms.

There needs to be sufficient data contributing to each voxel for the weighted average to be effective for gating. This means the size of the subset needed to increase to include more angles of the gantry rotation. In this case, ten equally spaced 1-degree ranges around the gantry were picked. When the correction is applied to each voxel, each exposure image will have a different weighting based on the phase angle distance. The weighting will prioritise the exposures that are close to the target phase angle and reduce the impact of the exposures that are away from the phase angle. In that way, the motion should be suppressed while still using all available data to some extent.

This algorithm requires the scan to have a well-distributed set of time points i.e. there should not be any large arc segments of the scan with no data for a particular phase. Otherwise, all the data would be suppressed along with that arc segment, and it will not be possible to properly define the edges of the object coming from that arc segment. This condition should not happen if the speed of motion is significantly faster than the speed of the scan (or the opposite case).

This approach also offers fine-grain control over the target phase angle as it is a central value that the user can pick at any angle across the 360 degrees. If the quality of this technique is of a sufficient standard, there is the potential to have more time points than the 8 temporal bins computed so far. The downside to this is for the n phase angles, n reconstructions would be required. Thus, there is a significant increase in processing time needed to perform this method of gating when a high number of phases are used. Also, by increasing the size of the subset, each reconstruction will also be slower than

when no gating is applied.

5.2.1 Comparing the image quality of weighted-based reconstruction and temporal binning

In this section, the image quality of the gated images reconstructed by the temporal binning and the weight-based algorithms will be compared. The target and exposure image phase angles for both reconstruction methods were obtained based on the gating algorithm described in chapter 4.

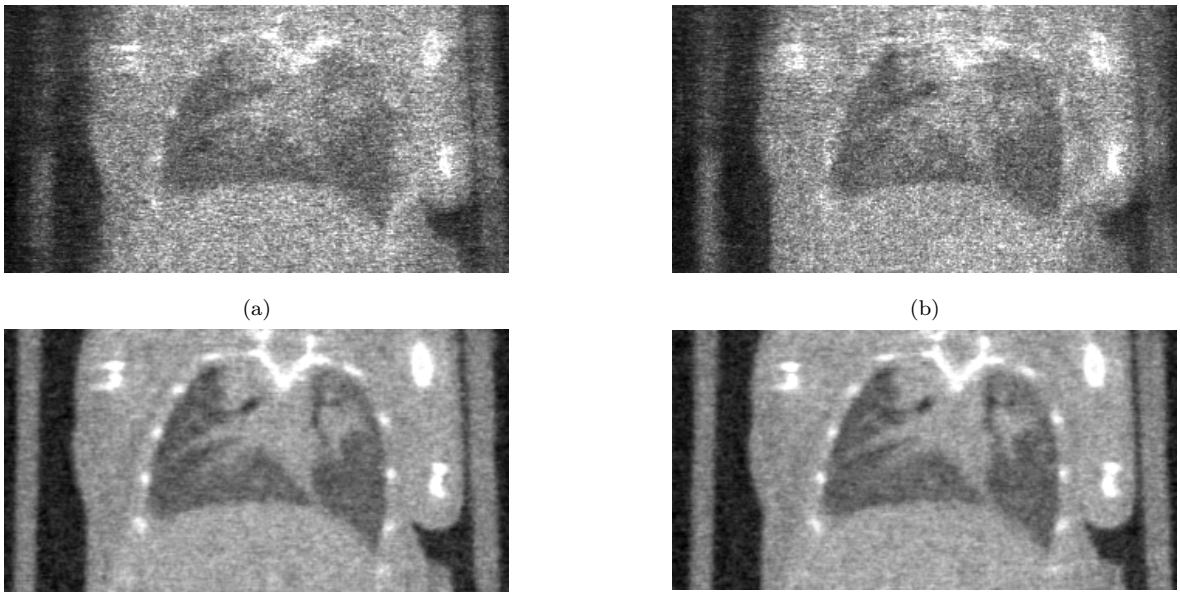

(a) (b) (c) (d)

Figure 5.2: A comparison of the quality difference between temporal binning (top row) and the weight-based approach (bottom row). Images (a) and (c) are from phase 2 (centered at 45^0) and images (b) and (d) are from phase 3 (centered at 90^0). In particular, the lung nodules are now visible. Also, the left boundary of the falcon tube is complete, while there is noticeable distortion in the temporal binning case.

As discussed in the previous section, the goal of the weight-based reconstruction method was to reduce the impact of the noise as a result of severe undersampling. The reconstructed image of the live scan in phase 2 and 3 of 8 temporal bins presented in section 4.4 are two cases of severe undersampling These images were reconstructed with only 5% (125 exposure images) and 4.8% (120 exposure images) of the total available ex-

posure images, respectively. Phase 2 and 3, based on Table 4.1 are centred around angles 45^0 and 90^0 respectively. Fig. 5.2 compares the image quality of the both reconstructed methods by targeting angles 45^0 and 90^0 respectively. The video of the breathing cycle using live mouse scan data reconstructed by the weight-based is available in the following link: weight-based video[2].

To compare the noise quantity in two methods, the SNR and CNR in the volumes reconstructed with the temporal binning and the weight-based method were computed based on the method described in section 4.4.2 and are presented in Table 5.1.

Table 5.1: The SNR and CNR of the gated reconstructed slices by the weight-based method and temporal binning method.

Reconstructed data	SNR	CNR
Phase 2 gated (weight-based)	6.7	13.9
Phase 3 gated (weight-based)	6.4	14.1
Phase 2 gated (temporal binning)	3.79	5.66
Phase 3 gated (temporal bining)	3.80	6.88

By applying the weight-based reconstruction method the image quality improved and SNR and CNR increased in both phases (2 and 3) compared to temporal binning. From this, we can conclude that the weight-based method could successfully mitigate the undersampling noise. Based on this result, we will use this reconstruction method in this thesis from now on.

Going forward from this chapter, we will not apply the inpainting algorithm on the exposure images. The inpainting by itself may inject some noise for the area with a large number of masked pixels. Therefore, to avoid inducing any further noise in this algorithm when computing the mean photon count in the defined region of interest, the masked pixels with zero values are simply ignored.

[2]https://youtu.be/4LnmHF_MCHA

5.3 Evaluation of the gating algorithm using the motion phantom

To evaluate the intrinsic gating method from chapter 4 and study its performance for varying amounts of motion, we performed a few scans with the motion phantom in MARS-10. Three known concentrations of iodine (as a contrast agent), three known concentration of calcium (as bone), water as a soft tissue-equivalent material, and lipid as a fat-equivalent material, were inserted into the motion phantom's nine built-in capillaries. Details about these materials and their order will be given in chapter 6 when we study the effect of motion on MD.

Under optimal anaesthesia, the respiration rate of a mouse is in the range of 55-65 bpm (Ewald *et al.*, 2011). Therefore, to simulate the breathing pattern of an anaesthetised mouse, the sine wave frequency of the motion phantom was set to 1. This meant one full cycle occurred per second or 60 cycles per minute. Equation 5.2 describes the sine wave applied to the motion phantom. In this equation O is an offset and A is the amplitude. The value of O and A were measured experimentally to produce scans with amplitude's of 1 mm to 5 mm.

$$Y = O + Asin(2\pi \times t) \tag{5.2}$$

To perform the scan, the scan protocol for live imaging given in Table 5.2 was used. To further avoid issues with undersampling, we increased the number of exposure image acquisitions to 1800 images in 360 degrees (the typical number is 720). To have a reference to evaluate the improvement after applying gating algorithms, the motion phantom was scanned in a stationary state as a ground truth. Fig. 5.3 shows the motion phantom and a reconstructed slice in the stationary scan.

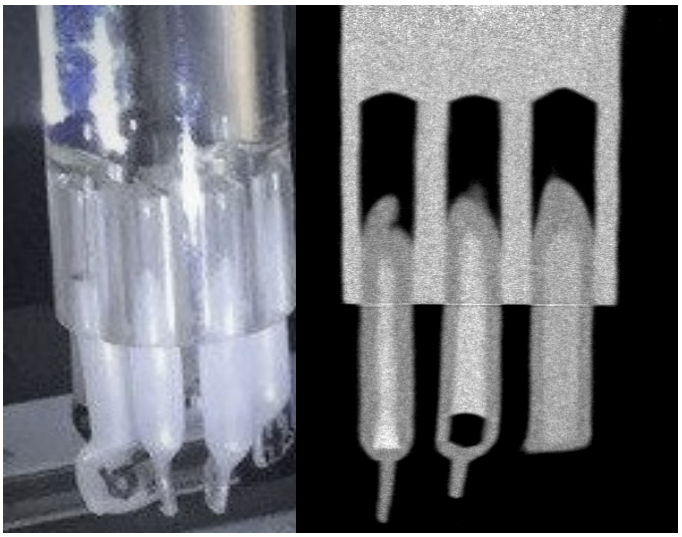

(a) (b)

Figure 5.3: The motion phantom with its material solutions are shown in (a) and one reconstructed slice (coronal view) in the stationary state is given in (b).

Table 5.2: The motion phantom scan parameters with an amplitude of 0 to 5 mm.

Scanning parameters	**Set values**
Scan type	Helical
Tube voltage	120 kVp
Tube current	28 µA
Exposure time	220 ms
SDD, SOD	291.95 mm, 211.95 mm
Field of view	32 mm
Circular exposure flatfields	1800 over 360 ^{0}
Voxel size	0.11 mm
Filtration	1.96 mm Aluminium
Energy bins (CSM)	15-30, 30-45, 45-60, 60-70, 70-120 keV
Pixel spacing	0.11×0.11

The motion signal was acquired by applying the gating algorithm on the motion phantom scan data for amplitudes of 1 mm to 5 mm. When we considered what phase angles to target, we found the peaks to be at 0^0 and $180,^0$ instead of the expected -90^0 and 90^0. The reason why was that the Hilbert transform applied in section 4.3.4 for computing the phase signal, induces a 90 degree phase shift for the imaginary component, and that translates to a 90 degree phase shift in the signal. Therefore, the peaks of the motion signal instead of being identified at 90^0 and -90^0, were found to be around angles 0^0 and 180^0.

The peak difference images were acquired by computing the absolute value of the subtraction of the two peak images to be compared. In the peak difference image, the perspex and the material vial's edges are highlighted in white, emphasising the transition of the phantom from two-time points at phase at 0^0 to 180^0. This white region corresponds to the phantom's blurred region in the non-gated image.

The non-gated, the gated reconstructed slices in both target phases, and the peak difference image for 1 mm to 5 mm scan data are given in figures 5.4, 5.5, and 5.6 respectively. It is important to note that these images are not shown in their real size due to limitations in space.

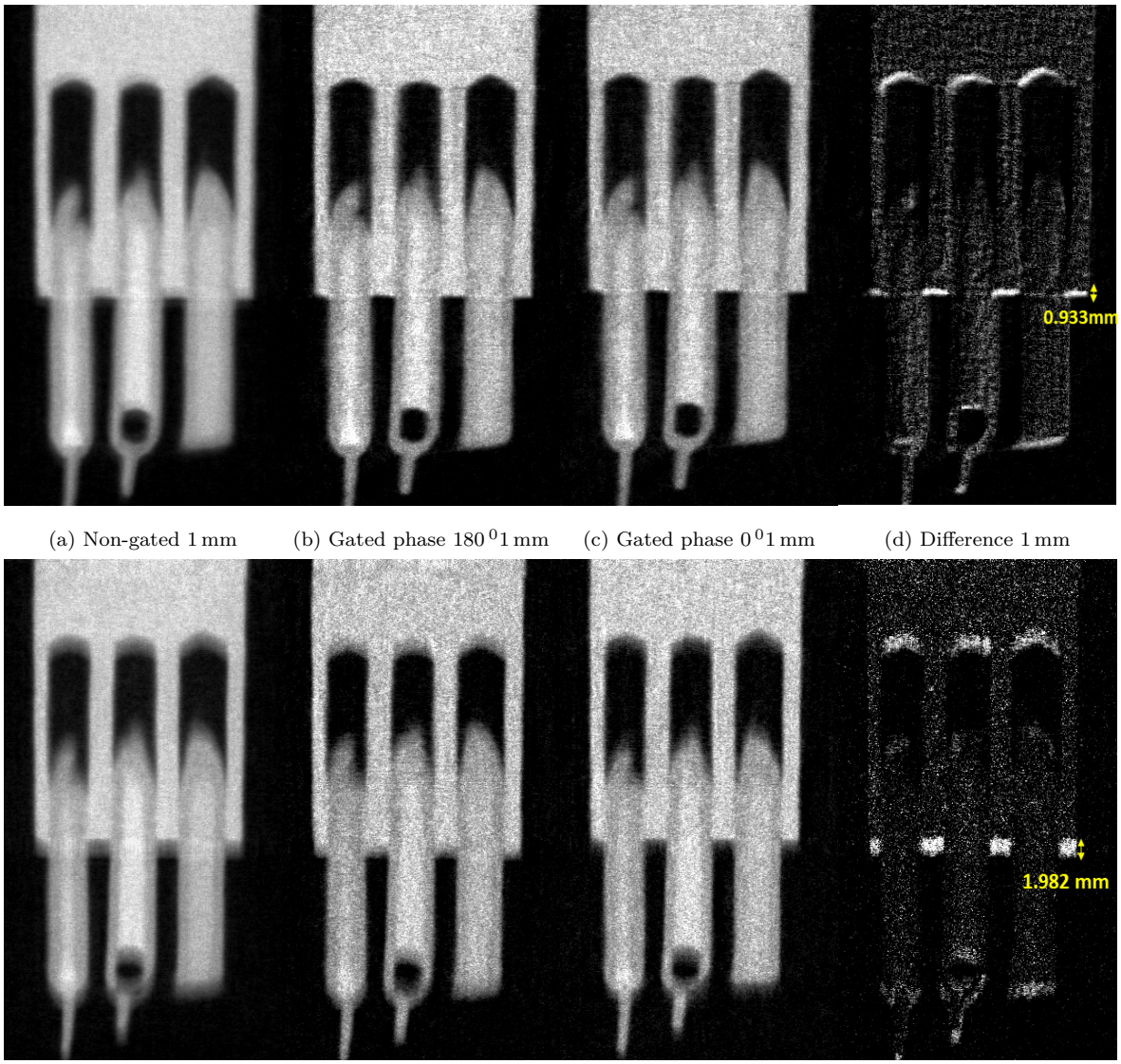

(a) Non-gated 1 mm (b) Gated phase 180^0 1 mm (c) Gated phase 0^0 1 mm (d) Difference 1 mm

(e) Non-gated 2 mm (f) Gated phase 180^0 2 mm (g) Gated phase 0^0 2 mm (h) Difference 2 mm

Figure 5.4: An illustration of the results of applying gating on amplitudes of 1 mm and 2 mm. The first row shows the 1 mm scan's non-gated, the gated images in phase 180^0 and phase 0^0, and the peak difference image in (a) to (d). The second row shows the corresponding images in the 2 mm scan in (e) to (h). There are double edges around the air hole particularly visible in the 2 mm non-gated image in the central material solution. Blurring is also visible at the perspex edges in the non-gated images. By applying gating, the structures in the images, such as air holes inside the material solutions turn out to be sharper, though minor blurring remains in the 2 mm gated images. The peak difference image shows the motion affected area with movements. The measured amplitude of movements in each peak difference image is shown in yellow and are close to the set amplitude.

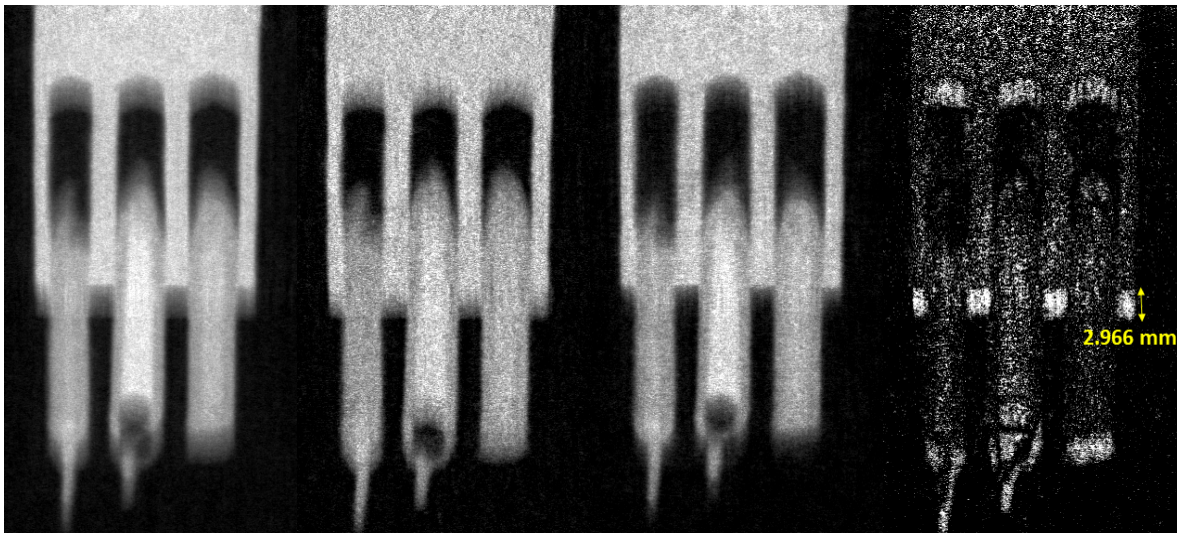

(a) Non-gated 3 mm (b) Gated phase 180^0 3 mm (c) Gated phase 0^0 3 mm (d) Difference 3 mm

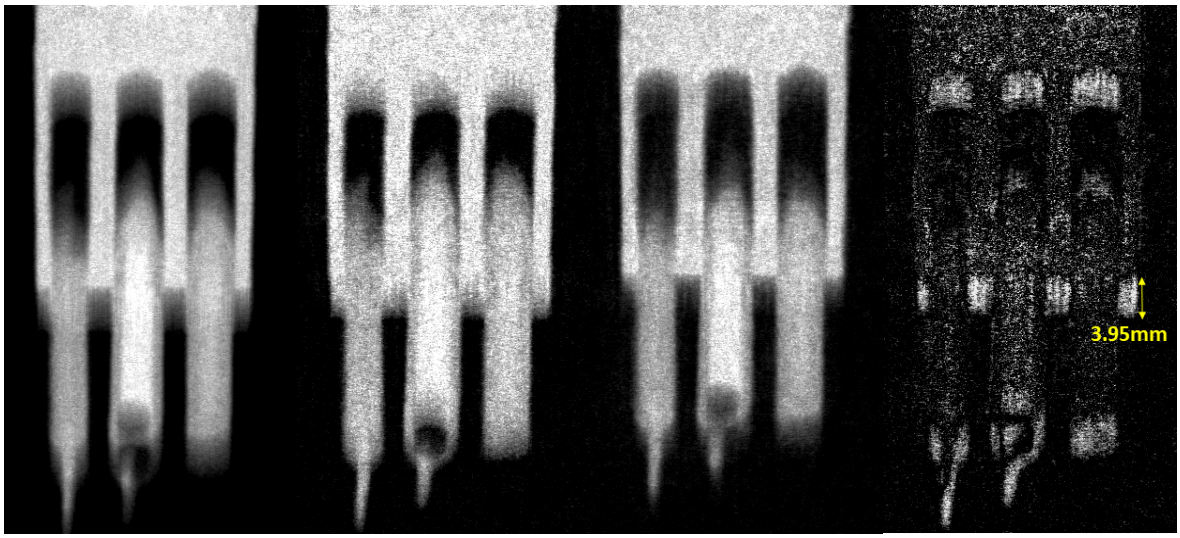

(e) Non-gated 4 mm (f) Gated phase 180^0 4 mm (g) Gated phase 0^0 4 mm (h) Difference 4 mm

Figure 5.5: An illustration of the results of applying gating on amplitudes of 3 mm and 4 mm. The first row shows the 3 mm scan's non-gated, the gated images in phase 180^0 and phase 0^0, and the peak difference image in (a) to (d). The second row shows the corresponding images in the 4 mm scan in (e) to (h). There are double edges around the air hole in the central material solution and the perspex edges in the non-gated images. The central air hole in the central vial turn into two holes by increasing the amplitude to 3 mm and 4 mm in (a) and (d). By applying gating, the structures in the images, such as air holes inside the material solutions turn out to be sharper though some blur still remains and clearly is visible in (c) and (g). The peak difference image shows the motion affected area with movements. The measured amplitude of movements in each peak difference image is shown in yellow and are still close to the set amplitude.

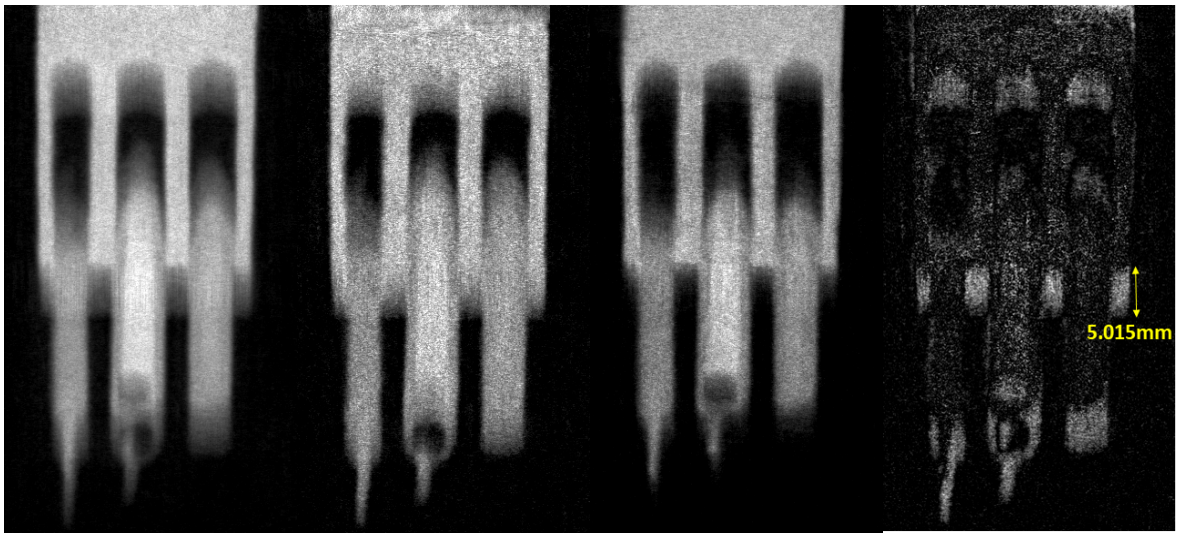

(a) Non-gated 5 mm (b) Gated phase 180^0 5 mm (c) Gated phase $0^0$5 mm (d) Difference 5 mm

Figure 5.6: An illustration of the results of applying gating on the amplitude of the 5 mm motion phantom scan. The non-gated, the gated image in phase 180^0, phase 0^0 and the peak difference image is in (a) to (d). In (a) the blurring is significantly visible in the perspex edges and the material vials and air hole. Two distinct air holes are clearly seen in the central material solution in the non-gated images. By applying gating, the structures in the images, such as air holes inside the material solutions turn out to be sharper and the extra air hole is removed. However, still some blurring is presented in the perspex edge and air holes. In the peak difference images the motion amplitude is measured and is shown in yellow, which shows 5.015 mm of motion between time points.

The amount of blurring in the reconstructed non-gated images is more visible by increasing the amplitude of movements from 1 mm to 5 mm. A clear air hole in the stationary image turned out to be smeared out with double edges in 1 mm and 2 mm scans and in 3 mm to 5 mm two holes were observed instead of one in the non-gated slices. Although the gated images are closer to the stationary scan there is still some blurring around the perspex vial and edge. The gated image in phase 0^0 in 1 mm is sharper than the gated image in phase 0^0 in 2 mm to 5 mm. For example, phase 0^0 in the 5 mm scans, has a blurred hole in the material vial while the image phase 0^0 in 4 mm has sharper hole compared to 5 mm. Therefore, by increasing the amplitude of the signal from 1 mm to 5 mm the capability of the algorithm for removing all blurring and motion artefacts reduces. However, it still can detect peak phases correctly.

Increasing the amplitude of the signal from 1 mm to 5 mm increased the thickness of white bands in the peak difference images. When the thicknesses were measured, they were roughly the 1 mm to 5 mm we expected. The gated images in all scans are closer in shape to the stationary scan shown in Fig. 5.3. We can conclude that the gating algorithm accurately tracked peak phases in the range of 1 mm to 5 mm.

The algorithm showed its improvements on the reduction of blurring in subject with the smallest structure of 2.5 mm (the maximum diameter of the air holes). In the live animal scan by a mouse, the movements were in the range of 1 mm to 2 mm. Based on measurements made by Studinger *et al.* (2003) the changes in a humans' carotid artery's radius in the systolic phase were about 3.68 mm and in the diastolic phase was 3.26 mm in the resting phase. These values were measured after exercising for 55 minutes. Therefore, the algorithm should be potentially good enough based on the observation of the motion in the motion phantom amplitude's in this range to generate a reconstructed image with limited artefacts in both of these cases.

In humans, when a patient breathes, the net movements of the diaphragm between the inhale and the exhale phases is between 3 cm to 6 cm (Sutton, 1987). If we want similar spatial resolution of 110 μm wide cubic voxels, then we will need to further improve the gating techniques as this is at least around 10 times more than what we studied here.

5.4 Quantitative image quality assessment

The motion phantom provides a chance to compare stationary reconstructed volumes with motion-gated volumes and non-gated volumes for quantitative image quality measurements.

In this section, mean squared error (MSE) and Jaccard distance ($J_{distance}$), two full-reference image quality assessment metrics, will be applied on the gated and the non-gated volumes by using the motion-free volume as a ground truth.

5.4.1 Mean squared error (MSE)

The mean squared error (MSE) is a common image quality metric in full-reference methods. The MSE between two images, including the reference image R(x,y) and the distorted image D(x,y), is defined as averaging the pixel intensity difference between them (Sara *et al.*, 2019; Wang *et al.*, 2004). This is demonstrated in equation, 5.3. MSE measures how close the estimated value is to the actual value. Being closer to zero means that the two images are better matched.

$$MSE = \frac{\sum_{i=0}^{J} \sum_{j=0}^{I} (R(i,j) - D(i,j))^2}{IJ} \tag{5.3}$$

Based on the image quality of the gated images from 1 mm to 5 mm, we expect to see lower MSE in the gated images compared to the corresponding non-gated images when using the stationary scan as a reference. The gated images with higher amplitude, such as 4 mm and 5 mm, are still slightly blurry. However, they are closer to the stationary image compared to the highly distorted non-gated images. Therefore, we expect to see a higher difference between the MSE of the non-gated and the MSE of the gated images by increasing the amplitude.

5.4.2 MSE results

The MSE of the gated and the non-gated volumes were measured on a per-slice basis for each scan from 1 mm to 5 mm. The average MSE was acquired by averaging all the MSE values in slices in the volume. The results are shown in Fig. 5.7.

The MSE increased as the amplitude went from 1 mm to 5 mm in the both the gated and non-gated volumes. Applying gating in both phase volumes resulted in a very close noise reduction.

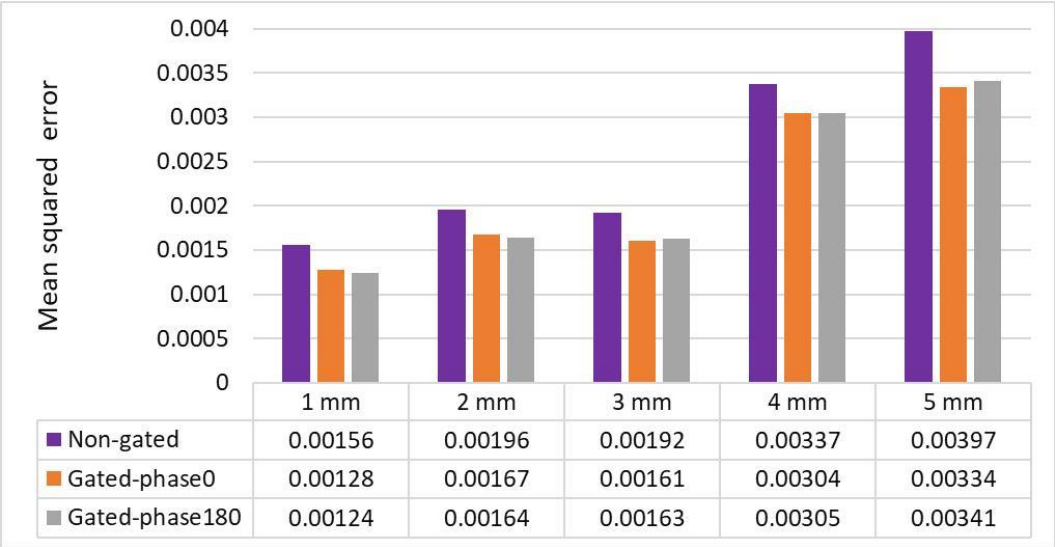

	1 mm	2 mm	3 mm	4 mm	5 mm
Non-gated	0.00156	0.00196	0.00192	0.00337	0.00397
Gated-phase0	0.00128	0.00167	0.00161	0.00304	0.00334
Gated-phase180	0.00124	0.00164	0.00163	0.00305	0.00341

Figure 5.7: The averaged mean squared error (MSE) in two phases of the gated and the non-gated volume in regard to stationary volume. Increasing movements length from 1 mm to 5 mm increased the MSE in both the gated and non-gated volumes. The measured MSE was reduced by applying gating on both phases.

The relative MSE difference between phase 0^0 and the non-gated images in the amplitude of 1 mm to 5 mm were 17.9%, 14.7%, 16.1%, 9.7% and 15.8% respectively. Similarly the relative difference between MSE of phase 180^0 and the non-gated image in 1 mm to 5 mm were respectively 20.0%, 16.3%, 15.1%, 9.4% and 12.5% closer to the stationary scan. These values show gating helped to reduce the distortion induced in the images by a minimum of 9.4% and a maximum of 20.0% and made gated images closer to the stationary images. Increasing the amplitude of the movements fluctuated the values of the MSE, so no clear trend was observed.

5.4.3 Jaccard distance

Vedam *et al.* (2002) applied the Jaccard distance or relative index of distortion, exhibited in equation 5.4, to evaluate and quantify the dissimilarity between two volumes (the stationary and the gated). In this equation, the first volume (V1) is the non-gated or the gated dataset, and the second volume (V2) is the stationary dataset as the reference. The $J_{distance}$ has a value between zero and one. One means that volume V1

and volume V2 have 0% overlap, and the dissimilarity percentage is 100%. Zero means that the two volumes have 100% overlap and are identical.

$$J_{distance} = \frac{|V1 \cup V2| - |V1 \cap V2|}{|V1 \cup V2|} \tag{5.4}$$

The $J_{distance}$ for a binary volume is computed based on equation 5.5. N_{01} is the total number of pixels where V1 was zero and V2 was one. N_{10} represents the total pixel where V1 was one and V2 was zero, and N_{01} is the total number of pixels where both V1 and V2 are one.

$$J_{distance\ binary} = \frac{N_{01} + N_{10}}{N_{01} + N_{10} + N_{11}} \tag{5.5}$$

5.4.4 Jaccard distance results

To apply the Jaccard distance on the grey-scale volumes, the gated, the non-gated, and the stationary data were first converted to binary volumes. This was done by calling the function 'imbinarize' in MATLAB. The same threshold was applied for all volumes as the scan conditions for all volumes were similar to the attenuation values were expected to be similar. All the voxel values above the threshold were replaced by 1, and all other values were set to 0. Fig. 5.8 shows an example of a binary image and the binary volume of the 5 mm scans. The 3D images were created by importing the binarised volumes into the 'Volume Viewer' application in MATLAB.

The Jaccard distance was applied to the reconstructed images in full size. This means when comparing the gated and the non-gated volumes to the stationary images, most of the image structures are similar except from the induced motion in the axial axis. Therefore, we expected to see a high similarity between the gated and stationary images. In contrast, the gated images should have lower Jaccard distance values as they are closer in shape to the stationary scan. The Jaccard distance result of scans in 1 mm to 5 mm in phase 0^0 and phase 180^0 volumes and the non-gated volumes by referencing the stationary scans are shown in Fig. 5.9.

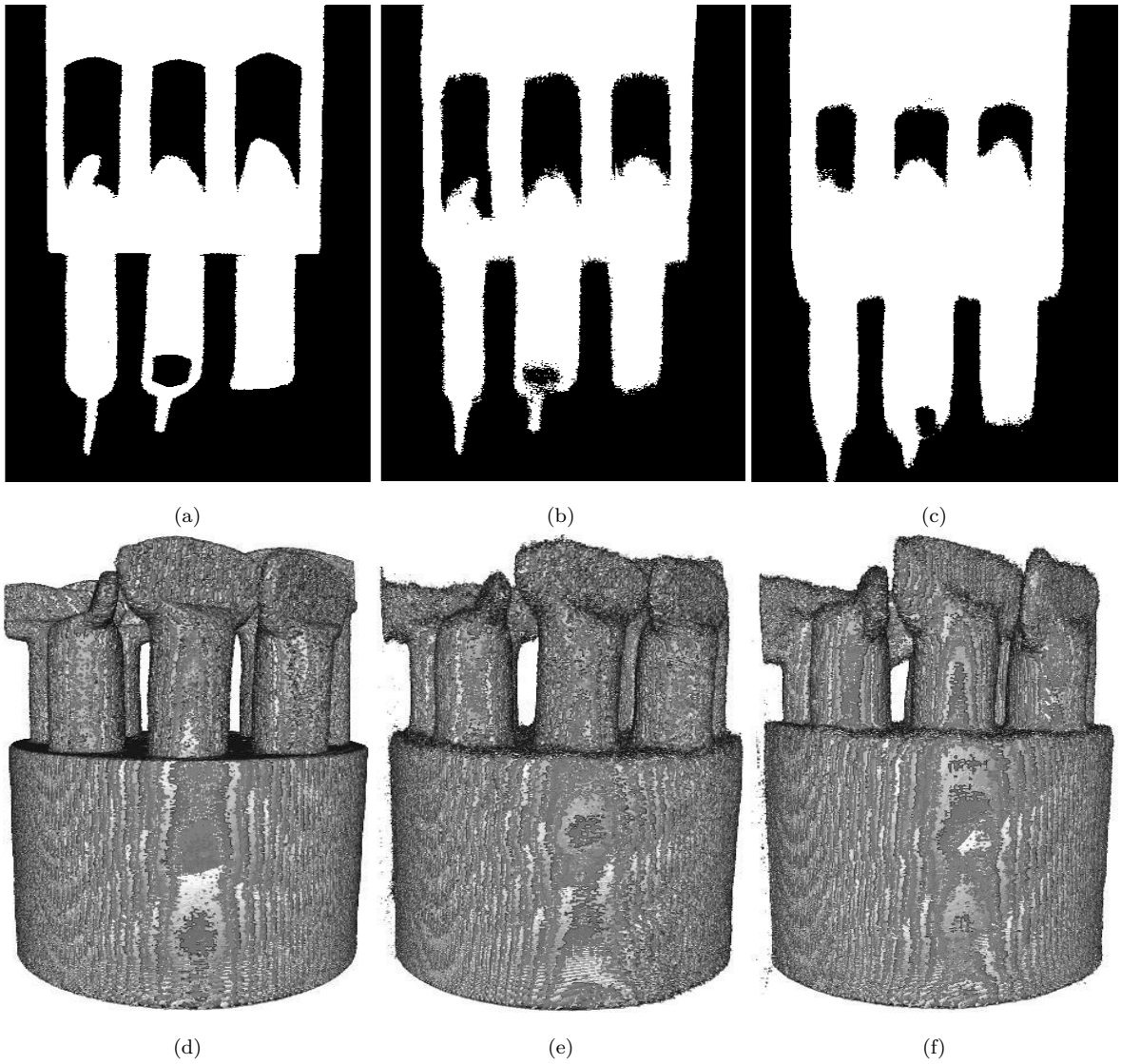

Figure 5.8: The visual presentation of the binarised images and volumes of the stationary, the gated and the non-gated data for an amplitude of 5 mm. The stationary, gated in phase 0^{0} and the non-gated image are given in (a) to (c). The corresponding binarised volumes of the stationary, gated and the non-gated of 5 mm scan are shown in (d) to (f). Applying gating reduced the distortion in the non-gated images, for example, (b) and (e) are closer in shape and structure to the stationary scan in (a) and (d).

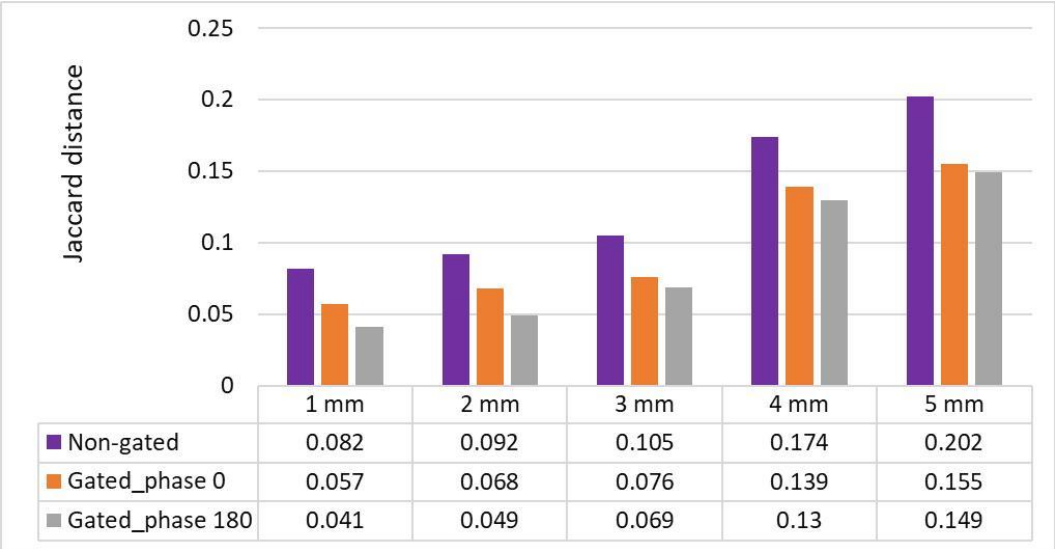

	1 mm	2 mm	3 mm	4 mm	5 mm
Non-gated	0.082	0.092	0.105	0.174	0.202
Gated_phase 0	0.057	0.068	0.076	0.139	0.155
Gated_phase 180	0.041	0.049	0.069	0.13	0.149

Figure 5.9: The measured $J_{distance}$ values between the non-gated, the two gated volumes by referencing the stationary volume. Increasing the movements from 1 mm to 5 mm, increased the dissimilarity percentage up to 20.2% between the stationary and non-gated volumes in 5 mm. By applying gating the distortion in the reconstructed images reduced by a minimum of 4.1% in 1 mm.

Increasing the amplitude of the sine wave from 1 mm to 5 mm increased the dissimilarity between the gated and the non-gated volumes against the stationary volume. Both gated volumes reduced the distortion, while the phase 180^0 relative differences results were up to a maximum of 20.4% more similar to the stationary scan. Based on the Jaccrad distance results, the gated volumes in phase 0^0 improved the distortion with relative differences of an order of 30.4%, 24.0%, 27.0%, 20.0%, and 23.0% in 1 mm to 5 mm scan respectively. Similarly phase 180^0 compared to the non-gated volume showed improvements in the relative differences of an order of 50.0%, 46.0%, 34.0%, 25.0%, and 26.0% in 1 mm to 5 mm scans respectively.

Based on the values of the relative differences results (gated and non-gated), the relative improvement of the gating algorithm decreased by increasing the amplitude of the movements from 1 mm to 5 mm. In the future, we need to investigate methods that enable us to increase the improvements in the distortion reduction of the gating algorithm in higher amplitudes as well.

5.5 Summary

- A motorised motion phantom for producing controllable periodic motion was designed and manufactured.
- A weight-based method for reconstruction of the gated volumes was introduced and applied to improve the undersampling artefacts observed in the temporal binning method. In this reconstruction, all the exposure images contribute to the reconstruction of the temporal bins depending on their distance from the predicted phase angle by the gating algorithm.
- The motion phantom was scanned with amplitudes of 0 mm to 5 mm with 1 mm increments. The scan data were gated based on the intrinsic gating algorithm and the weight-based reconstruction. The phase angles chosen to study were the two peaks located at 0^0 and 180^0.
- Gated volumes in both peak phases showed improvements in the reduction of blurring in the perspex and the material vial's edges.
- The result of evaluation metrics, MSE and Jaccard distance both confirm the reduction of distortion in the gated images compared to the non-gated images.

Chapter 6

Material decomposition and motion

The purpose of this chapter's work was to investigate the impact of motion on the accuracy of the MARS material decomposition algorithm. Applying MARS-MD on the motion phantom datasets in this chapter was done with the assistance of Aysouda Motanaghi a fellow PhD student from the University of Otago.

The chapter starts with a brief review of the MARS material decomposition algorithm in section 6.1. The details of the contrast motion phantom scans for the stationary and moving states are given in section 6.2. The MARS-MD's results for the non-gated images in the central region of the material solutions are presented in section 6.3 and section 6.4 investigates the effect of motion on the gated and non-gated images in the top edge region of the material vials. A summary is included in section 6.5.

6.1 Material decomposition for MARS imaging

Material decomposition is defined as a process of converting a set of linear attenuation coefficients into a set of material densities (Alvarez and Macovski, 1976). Material decomposition provides the quantitative information of tissue components and contrast

agents present in the reconstructed images.

As mentioned before, MARS imaging uses the Medipix3RX detectors, which measure up to eight energies simultaneously. This allows better material decomposition for more materials when compared to dual-energy CT systems (two energies). Previous researchers showed that MARS scanners could differentiate and quantify various materials and contrast agents simultaneously in their studies (Moghiseh *et al.*, 2018; Lowe *et al.*, 2018).

The process of performing MD on MARS scan data is divided into three main parts. First, the reconstructed images are acquired by applying the MARS iterative reconstruction algorithm on the scan data (see section 4.3.5 for details about the reconstruction algorithm). The next step is computing the material's basis vectors as part of MD calibration, and the final step is running the MARS-MD program.

Mass attenuation coefficient values are available from National Institute of Standards and Technology website National Institute of Standards and Technology (NIST). However, due to reconstruction results not being truly monochromatic and inaccuracies in the physical model, NIST mass attenuation coefficients can not be used. There is too much distortion. So we need experimentally derived effective mass attenuation coefficients. To get effective mass attenuation coefficients experimentally, the user is required to set up a particular scan. We call the subject a spectral phantom, and it contains a series of vials with known concentrations of substances we want to perform MD for in the real scan later.

The effective mass attenuation values can later be computed by using both the reconstruction of the spectral phantom and the known concentration values in each vial. The relationship between linear attenuation, material density and mass attenuation for a single voxel is linear and is shown in equation 6.1. Where M is a matrix of mass attenuation coefficients, P is a vector of material densities, and L is a vector of linear attenuation values.

$$M \times \vec{\mathbf{P}} = \vec{\mathbf{L}} \tag{6.1}$$

The calibration process itself is a little complicated. As each vial is a solution, the

materials are a combination of water and the other material. To separate the effects, multiple vials with different concentrations of the same materials are needed. The linear trend between the concentration and the linear attenuation values then can be used to derive the effective mass attenuation coefficients. An in-built MATLAB program called 'Data analysis' is then used to implement this process (Moghiseh *et al.*, 2016).

This program uses the reconstructed data and requires some inputs from the user including the number of materials in the scan and the number of vials for each material, the slice numbers to get data from, and the number of energy bins. From there, the user will manually place the same size and shape region of interests (ROIs) over each material vial for all selected slices. The algorithm then generates the effective mass attenuation coefficients file that includes the basis vectors for all the materials for each energy bin.

To accurately compute basis vectors, some factors needed to be considered. All material solutions should be homogeneous. The ROI around each material should be chosen carefully to avoid any edges in computing the mass attention. To get effective mass attenuation values that represent the majority of values in the vials, it is beneficial to sample values from various locations. The linear attenuation values can change depending on the surroundings around the vials, the noise properties, and the presence of artefacts. We determined that sampling around five slices where each slice is at least five slices apart from the others led to a decently balanced set of samples to work with. This is done to normalise the possible noise in the slices statistically. It is preferred that slices be free of beam hardening and ring artefacts. In cases where these artefacts are present in all slices, the ROI should be selected small enough to avoid the highly affected area.

Commonly, material basis vectors are computed based on slices in the middle of full vials to guarantee accurate measurements of the mass attenuation. However, the key is that we want to pick regions that are representative of the location we want to perform MD on. For example, if we are studying the material decomposition in areas around the top of the material vials, then the material basis values should be calculated from that region instead. In another example, if the goal is to perform MD in a scan of a

mouse, then you want to calibrate the MD where both the vials and the perspex holder are visible. The perspex holder has properties between lipid and water and makes for a decent surrogate of the effect of the mouse's body. In that way, the calibration tries to replicate the conditions that are likely to occur in the real scan. The location of the vials in the perspex, e.g. in an outer hole or inner hole is also important for this reason. The effective mass attenuation coefficients should then be used to run the MARS-MD software to test on the calibration scan and can then be applied in any real scans that uses the same scan protocols.

The X-ray linear attenuation and the material concentration are linked together based on the linearity. The linearity is a determining factor in the detection of the presence or absence of the materials. One reason to have misidentification and wrong quantification of unknown content could be due to poor linearity.

The accuracy of the linearity between the linear attenuation and concentration of each material within each energy bin can be established using least-squares linear regression (R^2). When the R^2 values are close to 1, it certifies the linearity and the data can be used as calibration to compute the unknown mass attenuation coefficients. Typically, we want R^2 values to be above 0.8 when running MD. The linearity plots of spectral responses, which shows the linear attenuation of each material versus the material concentrations in all energy bins is part of the outputs of the 'Data analysis' program.

The MARS material decomposition algorithm (called MARS-MD) is a post-reconstruction algorithm based on a constrained non-negative linear least square algorithm. As a result, one or two materials with the best fit are allocated to each voxel. The MARS-MD program output is then a set of material channels representing material density in mg/mL. The technical details about the MARS-MD algorithm are available in a paper by Bateman *et al.* (2018) and in his thesis in chapter 4 (Bateman, 2015).

The sensitivity of the material identification can be measured by analysing the resulting material images generated by the MARS-MD. This is done by calling a post MD analysis program called 'Identification measurements', a standalone MATLAB application. The output of this program illustrates the percentage of accurately identified voxels in a given region of interest for each material concentration based on the calibration scan vial's concentrations. An identification percentage below 100% is an indicator of the material's misidentification (Moghiseh *et al.*, 2016).

6.2 MARS-MD and its sensitivity to motion

In this section, we aimed to learn how motion influences the material identification and quantification. Which parts of the reconstructed volumes are more susceptible to higher distortion by motion. If the motion resulted in the material identification and quantification deduction, then can gating improve the lost information?

Highly attenuating or high-density materials cause beam hardening artefacts, which can affect the image quality of surrounding materials/tissues. Therefore, the order of material solution tubes in phantom should be chosen in a way to keep the low concentration material separated from high concentration material. This helps prevent basis vectors values being affected by the attenuation of high concentration materials.

The length of the motion phantom's vial is aligned along the z-axis, and the motion also happens mainly along the z-axis. Therefore, we expected to see a minimal effect of motion on the identification and quantification results for most of the vial. The only major effects are expected to be seen at the top or bottom edge of the material vials.

In chapter 5, we presented the result of running the intrinsic gating algorithm on the motion phantom data. It was shown that gating could reduce the distortion in reconstructed volumes. The non-gated data has higher SNR and CNR values, while they are more blurry, compared to the gated volumes. We will now study how the gated data with higher noise content affects the material identification and quantification result. The results of running the MARS-MD algorithm on the non-gated and the

gated volumes of the motion phantom scan in all six cases will be given in the next section.

6.2.1 MARS-MD and contrast motion phantom

We converted the motion phantom introduced in section 5.1 to a contrast motion phantom. We decided to study the response of calcium as a bone-like material, iodine as a contrast agent, water a soft tissue-equivalent material, and lipid as a fat-equivalent material. These are common materials in *in vivo* scans. To increase the success rate of material identification, three concentrations of each solution were chosen to be inserted in the motion phantom. This enables correct linear interpolation of the values between two consecutive concentrations. Therefore, the contrast motion phantom contained three known concentrations of iodine solutions (Visipaque (270 mg/ml) contrast agent), 18, 9 and 4.5 mg/mL and three known concentrations of calcium solutions (calcium chloride), 140, 70 and 35 mg/mL. The layout of the materials in the contrast motion phantom is shown in Fig. 6.1.

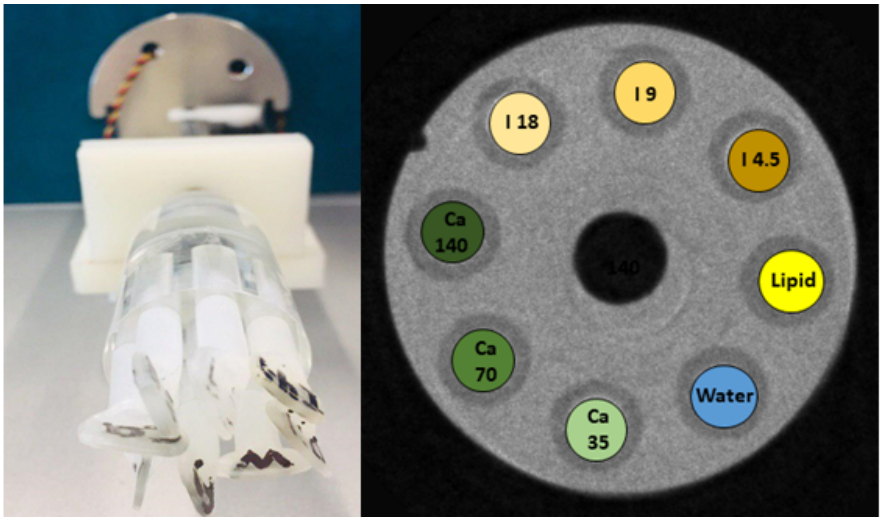

Figure 6.1: The contrast motion phantom material positioning including three concentrations of the calcium 35, 70, and 140 mg/mL, three concentrations of iodine 18, 9, and 4.5 mg/mL, water and lipid.

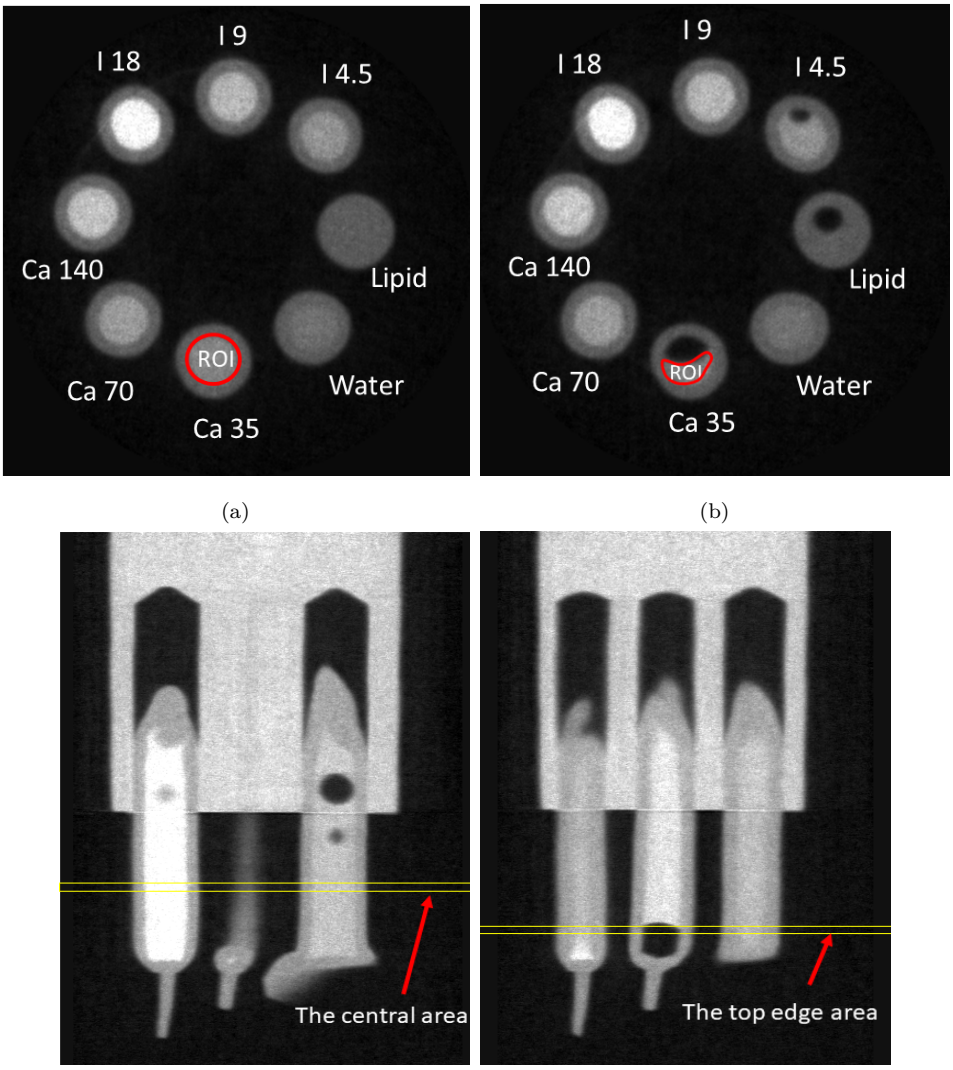

Figure 6.2: The axial and cross-sectional images of the stationary scan in the centre and the top edge region of the material vials. The axial images of in the central and edge region are shown in (a) and (b) respectively. The corresponding coronal images in the centre and top edge are shown in (c) and (d). The manually selected ROI around calcium 35 mg/mL in energy bin 1 is shown in red in (a) and (b). To prevent the presence of the air bubbles in the vials in the edge area, the ROI was chosen smaller than in full vial.

To study the effect of motion in different regions of the material solution vials, the material basis values were measured for the centre and the top edge regions in the stationary scan dataset. Fig. 6.2 shows a slice of the stationary data in the axial and the coronal views in the centre and the top edge of the material vials. The yellow

horizontal lines in the coronal view images show where the slices are chosen from.

The linearity of the spectral responses of the material solution vials in the stationary scan was measured by plotting the linear attenuation values against the concentration values of each material in the centre and the edge region. For example, we have illustrated the linearity performance of iodine and calcium in the stationary scan in the central region in Fig. 6.3. This figure shows the linear relationship between concentration and attenuation. The R^2 value was calculated for each material. All the material in the stationary scan in both regions (centre and edge) had demonstrated a suitably linear performance.

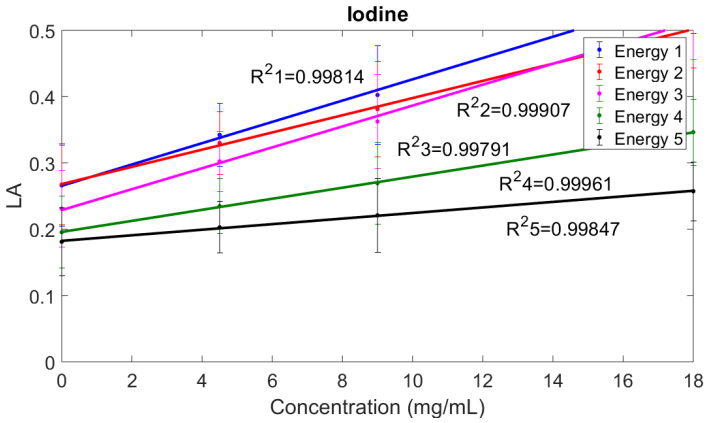

(a)

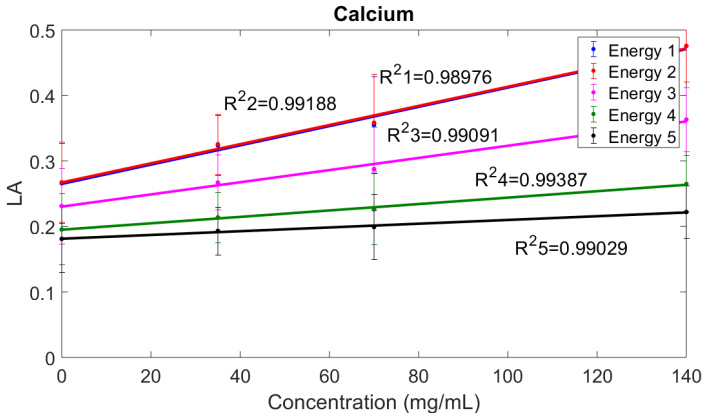

(b)

Figure 6.3: The linearity plots of spectral response of two materials, iodine and calcium, in the motion phantom within the stationary state is given in (a) to (b) respectively. The linear fitted lines for iodine and calcium show an average correlation. The error bars at concentrations of zero belong to water. The coefficient of determination, (R^2), was greater than 0.99 in all material concentrations in all energy bins, which confirms the linearity.

The spectral response trend of all materials in the phantom across all energies in the stationary scan was measured for the edge and the central region. Both spectral responses in the edge and central region showed a similar trend. Fig. 6.4 shows the spectral trend of all materials in the edge region. Three concentrations of iodine experience their element-specific K-edge in the energy range of 15-35 keV. The calcium's K-edge is about 4 keV, which is not detectable. The reason for its peak in the calcium attenuation profile at the energy range of 15-35 keV, could be due to fluorescence effects on the detector sensor layer that inflate the number of photons in the lower energies. Otherwise, the attenuation trends for all materials are as expected.

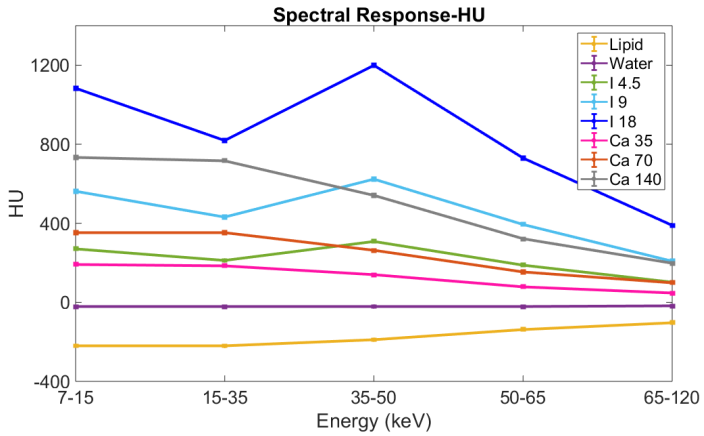

Figure 6.4: The spectral responses of various materials (iodine, calcium, lipid and water) in HU versus the multiple energies (keV) for the stationary scan in the edge region. The difference in the spectral response of all material is higher at lower energies. The K-edge of calcium is not in the diagnostic range but for iodine; it is clearly visible.

The MARS-MD algorithm is highly sensitive to noise. Each of these six scans is a new event, therefore the random aspects of the noise will change and each scan will have its own noise pattern. So based on this, it was expected to see bigger differences in the misidentification in the lower concentrations of iodine and calcium between the six scans.

The materials in all six scans were the same. Therefore, the basis values acquired from the stationary scan in the edge and the central regions were re-used to evaluate the concentrations of all materials for all scans. MARS-MD was run on all scans both

at the centre and at the top edge regions of the material vials. In the final step, the post MD analysis program was carried out using the MARS in-house identification program. To run this program on each scan, a similar region of interest was chosen in five different slices in the edge and centre of scan data.

6.3 Results of MD on the non-gated slices in the centre of the material solution vials

Three concentrations of iodine, three concentrations of calcium, water and lipid were able to be identified and quantified by applying MD on all six scans. In this experiment, we did not expect to see significant distortion in the material identification and quantification accuracy as the central region should not be highly influenced by motion. The percentage of identification success of each material in the central region of the material vials in the non-gated images is shown in Fig. 6.5.

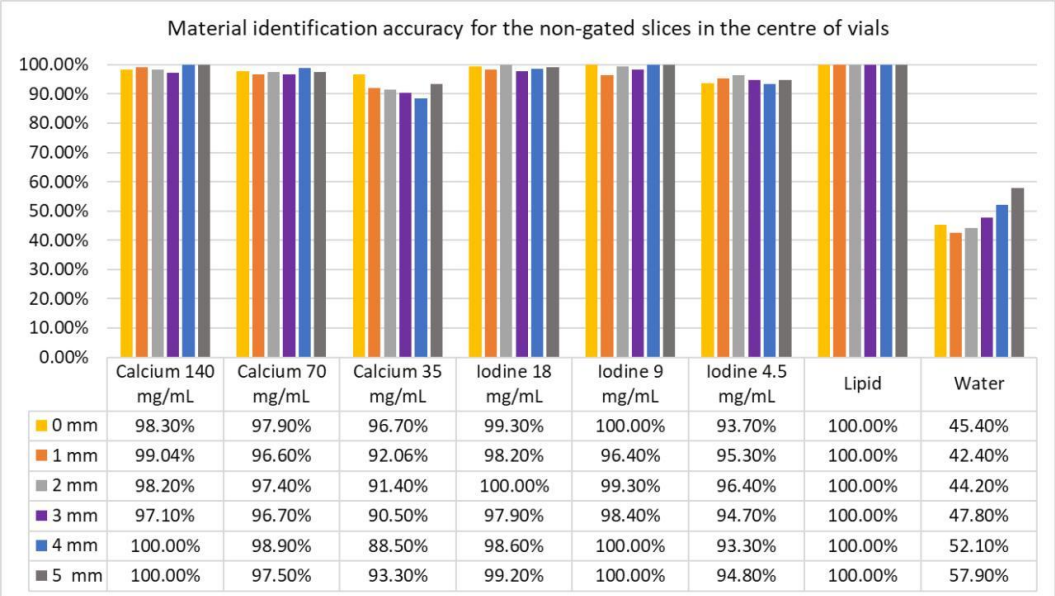

	Calcium 140 mg/mL	Calcium 70 mg/mL	Calcium 35 mg/mL	Iodine 18 mg/mL	Iodine 9 mg/mL	Iodine 4.5 mg/mL	Lipid	Water
0 mm	98.30%	97.90%	96.70%	99.30%	100.00%	93.70%	100.00%	45.40%
1 mm	99.04%	96.60%	92.06%	98.20%	96.40%	95.30%	100.00%	42.40%
2 mm	98.20%	97.40%	91.40%	100.00%	99.30%	96.40%	100.00%	44.20%
3 mm	97.10%	96.70%	90.50%	97.90%	98.40%	94.70%	100.00%	47.80%
4 mm	100.00%	98.90%	88.50%	98.60%	100.00%	93.30%	100.00%	52.10%
5 mm	100.00%	97.50%	93.30%	99.20%	100.00%	94.80%	100.00%	57.90%

Figure 6.5: The MARS-MD material identification success percentage for the motion contrast phantom with 0 mm to 5 mm of movements. No clear trend was observed in all materials by motion as there was a fluctuation in the identification in different scans. Lipid had the highest identification of 100% in all scans.

In the stationary scan, after lipid and iodine 9 mg/mL with 100% identification accuracy, iodine 18 mg/mL had the highest number of voxels correctly identified (99.3%). Increasing the motion amplitude slightly fluctuated the identification percentage in the central region. However, a consistent relationship between the amount of movement and the correct identification was not observed.

The lowest concentration of calcium had the highest reduction in the number of accurately identified voxels by motion. An 8% increase in misidentification was observed in calcium 35 mg/m by moving from 0 mm to 4 mm. Interestingly, its identification increased in 5 mm by 4.8%. Even in the stationary scan, its identification accuracy was less than 94%. This can be due to its low concentration that was distorted by the noise.

To answer the question of how motion influenced the material quantification, the concentrations of each material in the material decomposition images were measured. We manually selected five slices for each material volumes (calcium and iodine) in each of the six scans. The mean and its standard deviation for the concentration values of each region of interest were measured and then averaged by using ImageJ. We did not expect to see distortion in the quantification values as the material solutions are homogeneous and the ROIs are drawn away from the vial's edges. We did expect to see average values higher than the true known values as it is common in MARS-MD results. Fig. 6.6 shows the measured concentration values for material solutions in all six scans.

The quantification measurements for all materials in all scans were higher than their true values. Iodine 4.5 and 18 mg/mL had the same value in all scans. Some fluctuation in all concentrations of calcium was observed when increasing the amplitude from 0 mm to 5 mm. In calcium 70 mg/mL, a 4 mg reduction in concentration was observed by moving from 0 mm to 5 mm. However, in general, there was no clear trend to be reported. Motion did not negatively distort the quantification.

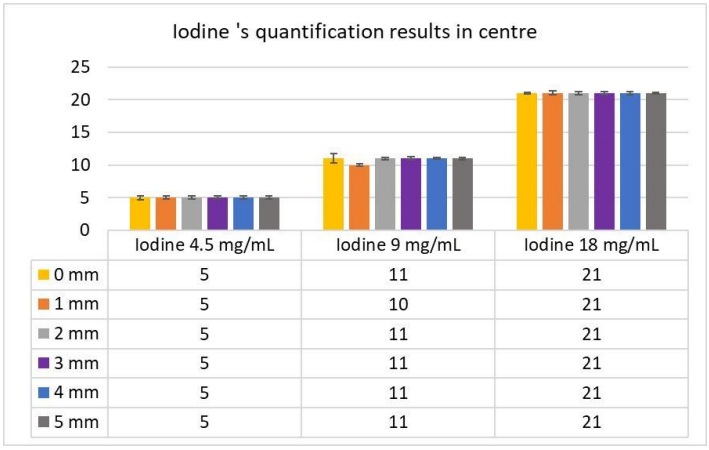

	Iodine 4.5 mg/mL	Iodine 9 mg/mL	Iodine 18 mg/mL
0 mm	5	11	21
1 mm	5	10	21
2 mm	5	11	21
3 mm	5	11	21
4 mm	5	11	21
5 mm	5	11	21

(a)

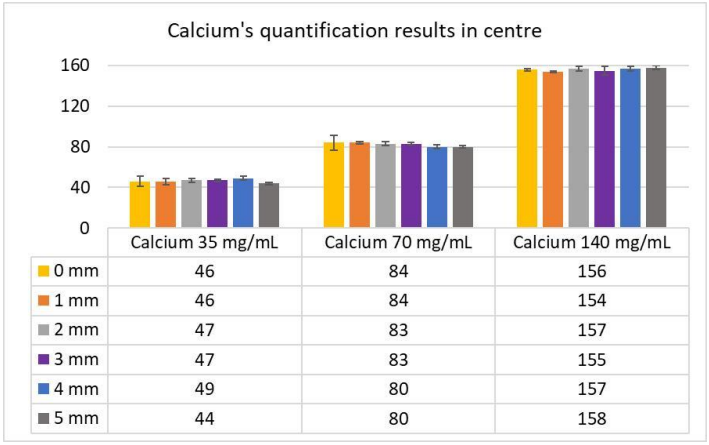

	Calcium 35 mg/mL	Calcium 70 mg/mL	Calcium 140 mg/mL
0 mm	46	84	156
1 mm	46	84	154
2 mm	47	83	157
3 mm	47	83	155
4 mm	49	80	157
5 mm	44	80	158

(b)

Figure 6.6: The measured material concentration values for the motion contrast phantom with 0 mm to 5 mm of movements. The y-axis represents measured concentration. The black thin error bar in the top of each coloured bar represents the standard deviation of measured mean concentrations. The measured concentrations for all materials were higher than their true value.

The results of identification and quantification in the central slices support our hypothesis that the motion has a low effect in this region. Therefore, we will not apply the MARS-MD on the gated data in this region. In the next section, we will study the impact of MD on the non-gated and the gated images where motion is expected to affect the results.

6.4 Results of MD on the phantom solution tube's edge slices

In this section, we present the results of performing MARS-MD on the non-gated data in the top edge area of the material vials. These results are given for all six scans. The top edge region of material vials is expected to be highly influenced by motion. Therefore, the identification and quantification accuracy is expected to be disturbed by increasing the motion amplitude from 0 mm to 5 mm. Figures 6.7 and 6.8 respectively illustrate the material identification and quantification values for all materials in the non-gated reconstructions from all six scans in the edge region.

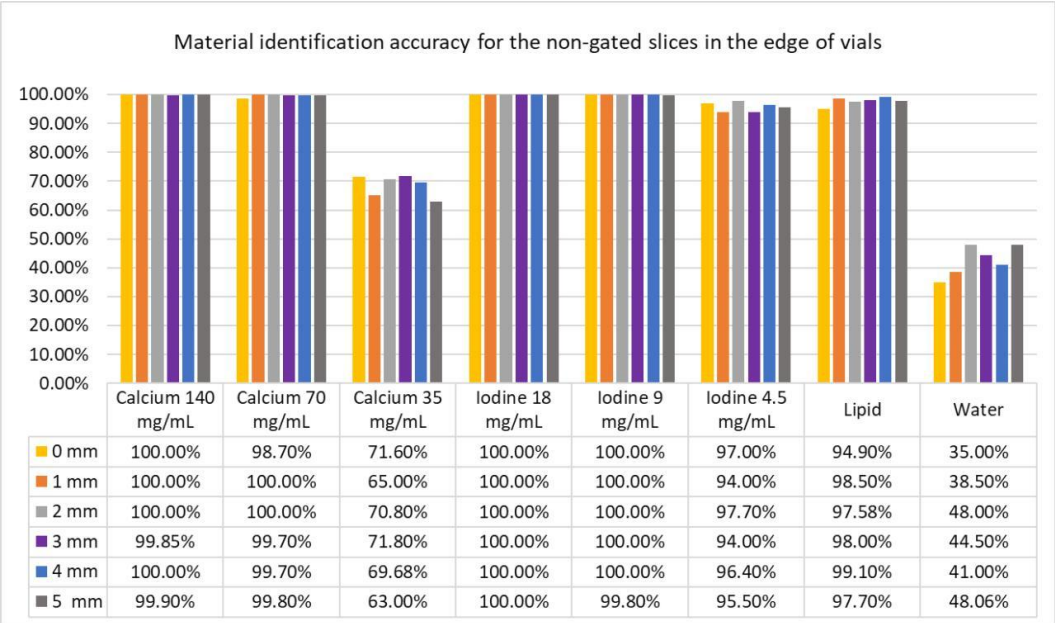

	Calcium 140 mg/mL	Calcium 70 mg/mL	Calcium 35 mg/mL	Iodine 18 mg/mL	Iodine 9 mg/mL	Iodine 4.5 mg/mL	Lipid	Water
0 mm	100.00%	98.70%	71.60%	100.00%	100.00%	97.00%	94.90%	35.00%
1 mm	100.00%	100.00%	65.00%	100.00%	100.00%	94.00%	98.50%	38.50%
2 mm	100.00%	100.00%	70.80%	100.00%	100.00%	97.70%	97.58%	48.00%
3 mm	99.85%	99.70%	71.80%	100.00%	100.00%	94.00%	98.00%	44.50%
4 mm	100.00%	99.70%	69.68%	100.00%	100.00%	96.40%	99.10%	41.00%
5 mm	99.90%	99.80%	63.00%	100.00%	99.80%	95.50%	97.70%	48.06%

Figure 6.7: The material decomposition success percentage for the motion contrast phantom with 0 mm, to 5 mm of movements. The identification percentage in the water and lipid increased as the amplitude went from 0 mm to 5 mm. Calcium 35 mg/mL with 8% percent reduction in identification had the highest misidentified voxels by moving from 0 mm to 5 mm.

In all six scans, calcium 140, 70 mg/mL and iodine 9 mg/mL were accurately identified with almost 100% accuracy. Water with 35% of accurately identified voxels in 0 mm, and 48% in 5 mm was the most misidentified material. Lipid in the stationary scan

in the edge area compared to the central region (see Fig. 6.5) had lower identification from 100% in the centre region to 94.9% in the edge region. No noticeable trend by increasing the motion amplitude from 0 mm to 5 mm was seen.

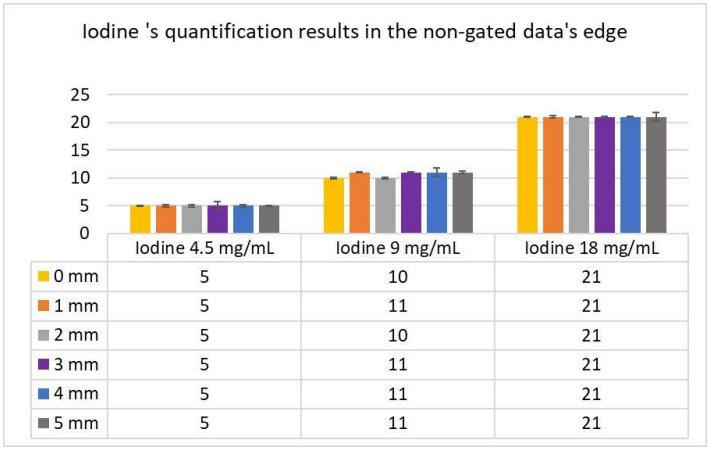

	Iodine 4.5 mg/mL	Iodine 9 mg/mL	Iodine 18 mg/mL
0 mm	5	10	21
1 mm	5	11	21
2 mm	5	10	21
3 mm	5	11	21
4 mm	5	11	21
5 mm	5	11	21

(a)

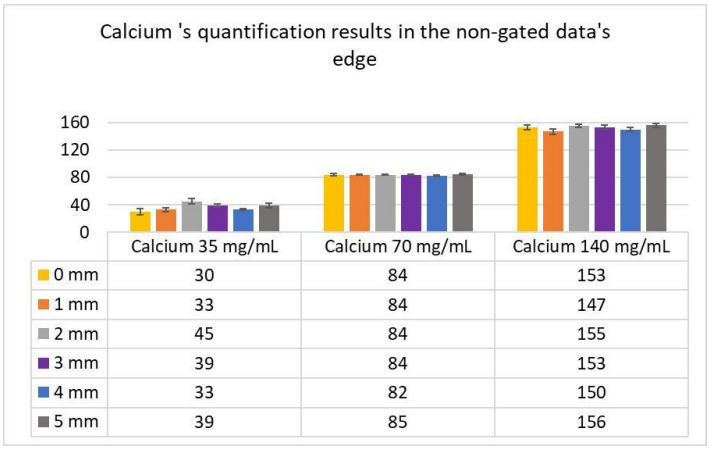

	Calcium 35 mg/mL	Calcium 70 mg/mL	Calcium 140 mg/mL
0 mm	30	84	153
1 mm	33	84	147
2 mm	45	84	155
3 mm	39	84	153
4 mm	33	82	150
5 mm	39	85	156

(b)

Figure 6.8: The measured material solutions concentrations in the motion phantom with 0 mm to 5 mm of movements in the top edge area. Some fluctuation in the measured concentration was also observed.

The measured concentrations for all materials were higher than their true values except for calcium 35 mg/mL in 0 mm, 1 mm, and 4 mm scans, which were lower than its true value. The concentrations of iodine 4.5 and 18 mg/mL in all six scans did not change when increasing the amplitude of the motion. Some fluctuations in the measured concentrations of other materials were observed by increasing the amplitude from 0 mm to 5 mm. In the presence of the motion, particularly in the materials with low atten-

uation and low concentrations such as calcium 35 mg/mL some misidentification and lower quantification than material's true value are inevitable. This misidentification can be worsen depending on the region the material decomposition is processing. As it is shown, images in the top edge, more vials showed higher sensitivity to motion in lower attenuating and lower concentration materials.

As it was shown in Fig. 6.2b, calcium 35 mg/mL had an air bubble inside its vial. The ROI used for calibration was much smaller to prevent having air in its ROI. However, the ROI may also have been closer to the edge voxels of the vial and air bubble than other ROIs. This also can be a factor contributing to the lower identification in calcium 35 mg/mL in the edge area.

In total, no clear trend between the motion amplitude and the material identification and quantification accuracy was observed. The main reason that can influence these results is the direction of the motion and the view of the MD images, which may prevent the motion effect from being visible. In addition, the presence of air bubbles due to manually filling the material solutions in the top edge area, stopped us from selecting slices that were at the very edge of the material vials. These two reasons put some shade on the result of identification and quantification in the non-gated images by increasing the motion's amplitude. In the next section, we will apply MARS-MD on the gated data to investigate if there are any improvements.

6.4.1 Result of MD on the gated slices

In this section, the results of MD on the gated images in all six scans are presented. By noting that the MARS-MD algorithm is highly sensitive to the noise, we will study how gating images with higher noise quantity and sharper edges will influence the material decomposition results. The material identification and quantification results of the gated slices in the edge area are displayed in Fig. 6.9.

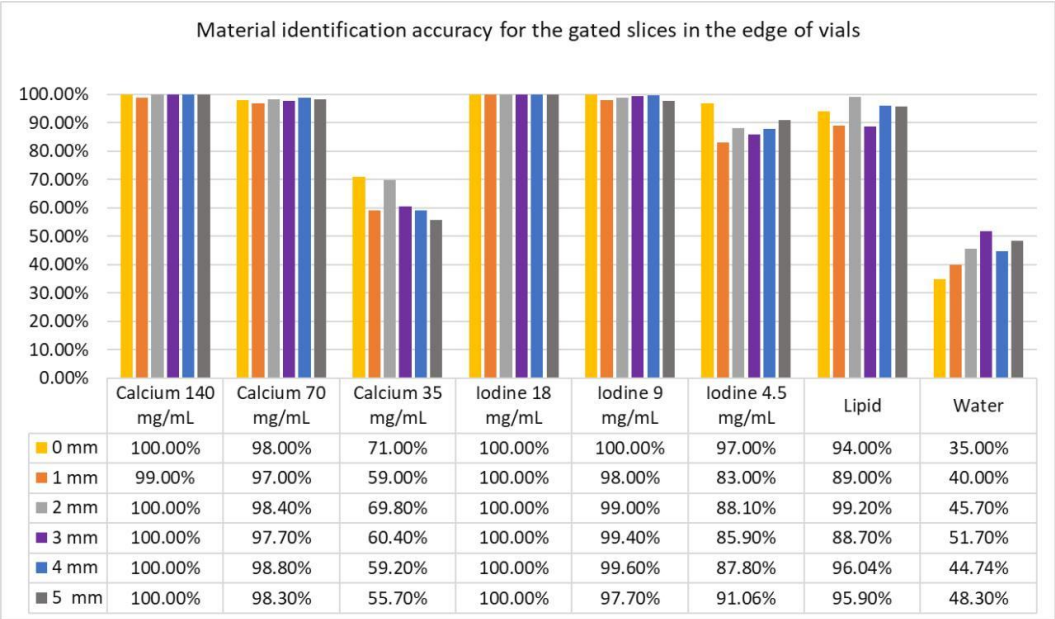

	Calcium 140 mg/mL	Calcium 70 mg/mL	Calcium 35 mg/mL	Iodine 18 mg/mL	Iodine 9 mg/mL	Iodine 4.5 mg/mL	Lipid	Water
0 mm	100.00%	98.00%	71.00%	100.00%	100.00%	97.00%	94.00%	35.00%
1 mm	99.00%	97.00%	59.00%	100.00%	98.00%	83.00%	89.00%	40.00%
2 mm	100.00%	98.40%	69.80%	100.00%	99.00%	88.10%	99.20%	45.70%
3 mm	100.00%	97.70%	60.40%	100.00%	99.40%	85.90%	88.70%	51.70%
4 mm	100.00%	98.80%	59.20%	100.00%	99.60%	87.80%	96.04%	44.74%
5 mm	100.00%	98.30%	55.70%	100.00%	97.70%	91.06%	95.90%	48.30%

Figure 6.9: The material identification percentage for the motion phantom with 0 to 5 mm of movements. There is no consistent trend between materials that clearly indicates better or worse performance from 0 mm to 5 mm.

Contrary to our expectations, gating did not improve the accuracy of material identification. Identifications of calcium 35 mg/mL, water, lipid, and iodine 4.5 mg/mL were less in the gated images compared to the non-gated data in all six scans. The other materials did not have a significant change and kept their previous values.

The quantification results of the gated data are shown in Fig. 6.10. They showed a similar trend to the non-gated results (see Fig. 6.8). In fact, there is no noticeable trend between 0 mm to 5 mm scans. Gating did not improve the misidentification and low quantification in materials with low concentration and low attenuation such as calcium 35 mg/mL.

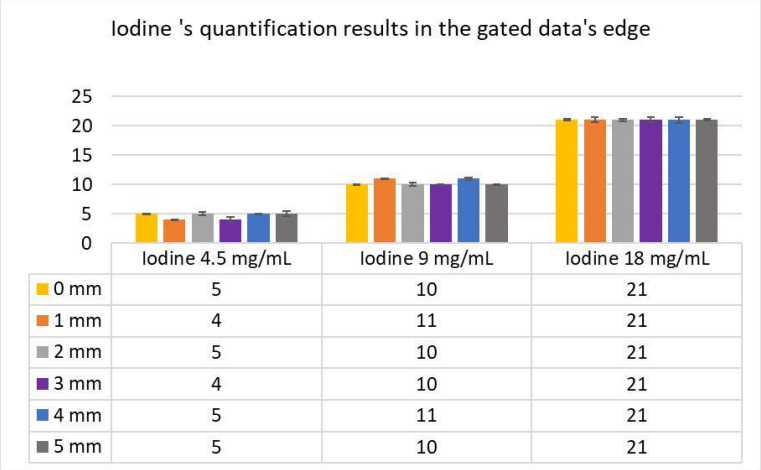

	Iodine 4.5 mg/mL	Iodine 9 mg/mL	Iodine 18 mg/mL
0 mm	5	10	21
1 mm	4	11	21
2 mm	5	10	21
3 mm	4	10	21
4 mm	5	11	21
5 mm	5	10	21

(a)

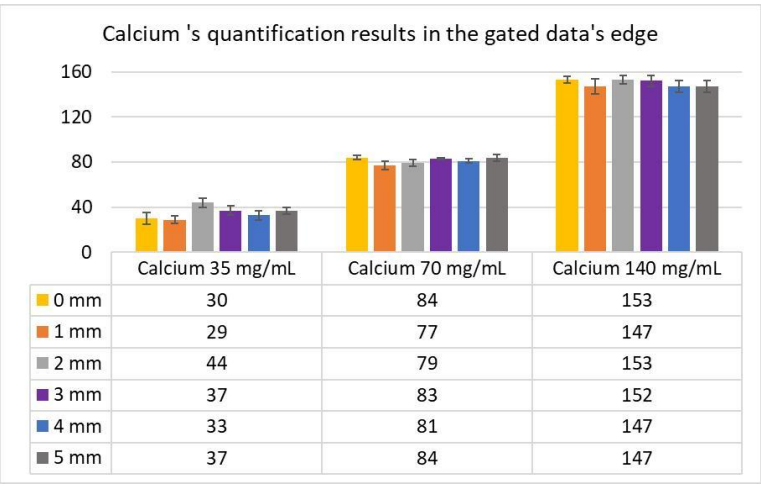

	Calcium 35 mg/mL	Calcium 70 mg/mL	Calcium 140 mg/mL
0 mm	30	84	153
1 mm	29	77	147
2 mm	44	79	153
3 mm	37	83	152
4 mm	33	81	147
5 mm	37	84	147

(b)

Figure 6.10: The measured concentrations for the material solution in phantom with 0 to 5 mm of movements. The y-axis represents measured concentration. All materials except for the lowest concentrations of iodine and calcium were measured higher than their true values.

6.4.2 Image quality and the MD results

The identification accuracy of a spectral system is normally limited by SNR (Taguchi *et al.*, 2020). Higher SNR in material images enables the spectral response to be computed more precisely. Lower SNR means a higher noise content in the image, and therefore, the spectral response will be limited by it. MARS-MD is also sensitive to noise, particularly at low concentrations.

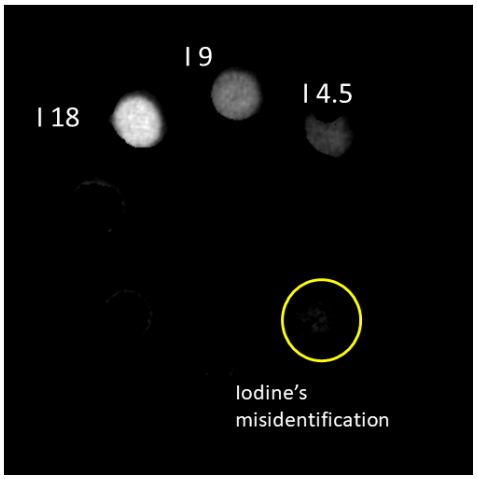

(a) Iodine stationary

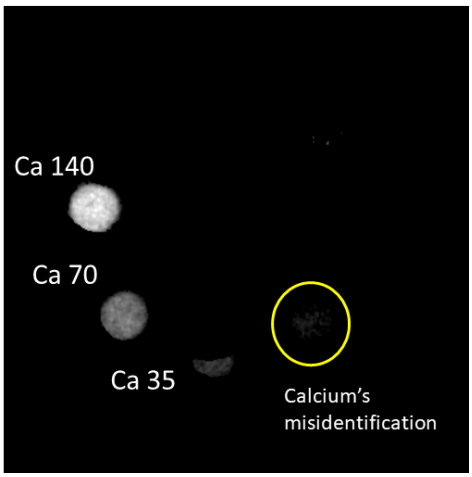

(b) Calcium stationary

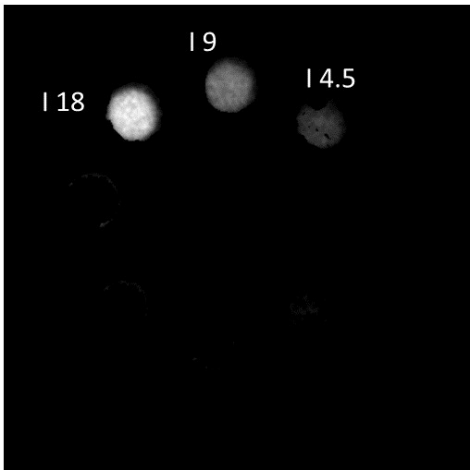

(c) Iodine non-gated 5 mm

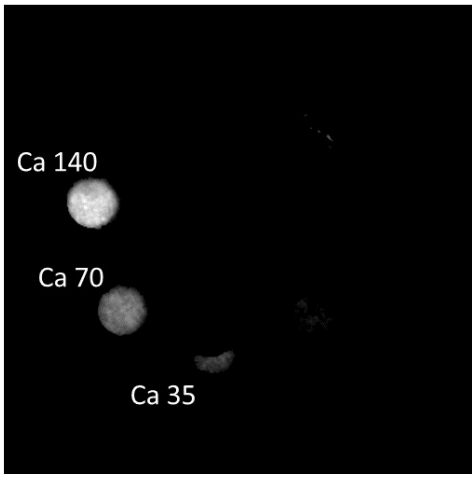

(d) Calcium non-gated 5 mm

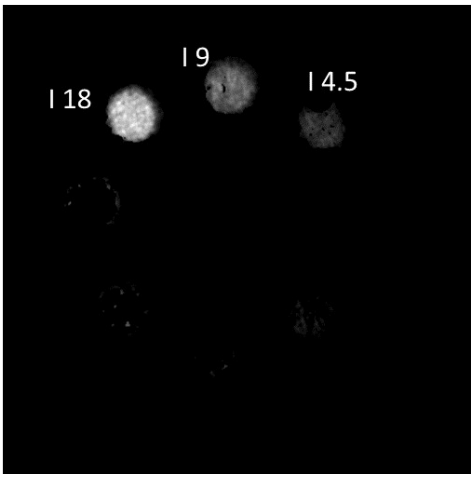

(e) Iodine gated 5 mm

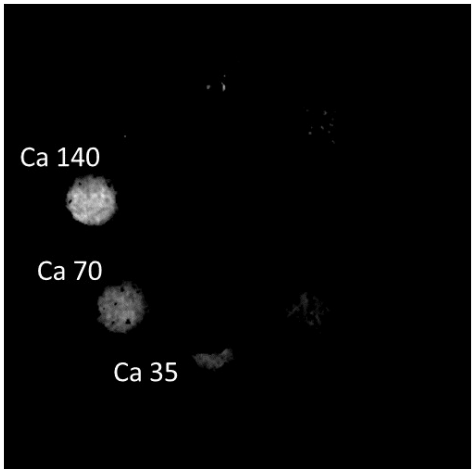

(f) Calcium gated 5 mm

Figure 6.11: Iodine and calcium's material images for the stationary (a and b), the 5 mm non-gated (c and d) and the 5 mm gated image (e and f) in the edge region. The gated images with lower SNR have higher inhomogeneous texture on them.

The stationary and the non-gated images were reconstructed by contribution of all exposure images in the scan data with equal weight. Therefore, the stationary and the non-gated images compared to the gated images have a higher SNR. To investigate the difference between the SNR in the gated and non-gated and the stationary images, the SNR values for these three datasets was measured in the stationary and the non-gated and gated images of the 5 mm scan. Five ROI square shapes with 200 pixels within one slice in the perspex holder were chosen to compute the SNR of the slice. The results for the stationary, the non-gated and the gated slices in 5 mm scans were 17.6, 16.56 and 10 respectively. Fig. 6.11 shows the material images of the stationary, the non-gated and the gated of 5 mm scan in the edge area.

Calcium and iodine concentrations in the gated images (e and f) compared to the stationary and the non-gated images have visible holes and are noisier. In contrast, the texture of the material vials of the non-gated images compared to the stationary image did not significantly worsen even by having 5 mm of motion. This result indicates the motion in the axial direction did not considerably alter the quantification and identification of the materials. At the same time, the lower SNR of the gated images negatively influenced the quantification and the results of the identification of MARS-MD.

The test we performed to study the effect of motion on the material decomposition accuracy had some limitations. First, the material solutions were filled manually; therefore, some air bubbles were inevitable to be inside the material vials. The presence of these air bubbles prevented us from selecting the very top slices to perform MD on them. The direction that the motion was generated from the motion phantom was in the same direction as the length of the vial. That limited the parts of the vial that were affected by it. The ROIs in both the centre and the edge area were selected away from the edges of the vials, which are expected to have some blurring due to motion.

In future, we will need more care when filling the material solutions to prevent having air bubbles in them. We want larger surfaces to be affected by motion. This could be done by rotating the vials 90 degrees. One possible solution to reduce the noise in the gated images could be changing the distribution weights in the reconstruction

algorithm to a wider distribution. This highlights that future developments in gating for MARS data must hold image quality as a high priority.

6.5 Summary

- Material decomposition represents the process of converting the spectral attenuation information into material information.
- MARS spectral CT can identify and quantify several materials.
- MARS-MD algorithm can differentiate and quantify materials, but its functionality is limited when the material has lower attenuation and low concentrations.
- There was no noticeable trend between the stationary scan results and the identification and quantification of the non-gated image by motion in the centre area.
- In the edge area, the identification of the lowest concentration of calcium in the stationary scan was reduced compared to the centre result. Still, no recognisable trend was observed between the motion and identification accuracy in the edge area.
- The quantification of all materials was not significantly distorted with motion in both the centre and the edge area.
- Gated data did not help improve the MD results. In fact, the opposite was true. We suspect this may be due to the increased noise in the gated data results. Further investigation is required to confirm this issue.

Chapter 7

Conclusion

In this chapter, the major results presented in this thesis are briefly outlined in section 7.1. In section 7.2, research topics that were investigated during the course of this thesis that requires further investigation are presented. The future goals of this PhD project are described in section 7.3. Finally, the conclusion is given in section 7.4.

7.1 Key points

This section reviews the main achievements and results over the scope of my PhD study with regards to performed research and investigation.

7.1.1 Live animal imaging requirements

In chapter 2, a study was performed to report on the main factors contributing to live animal imaging with regards to MARS spectral scanners. The importance of gating methods, anaesthesia delivery, free-breathing and temperature monitoring were investigated.

An anaesthetised mouse was scanned with MARS-11, and its core temperature trend was monitored during the scan time. A heat loss of 4.5 degrees in 18 minutes of scan time was observed when no heat source was applied.

A third party's mouse holder was modified to be compatible with MARS scanners, with a hand warmer as a heating source. A benchtop experiment and a scan with a phantom as a subject were conducted. The result showed the hand warmer could not deliver enough heat to keep the mouse core temperature around 37^oC.

7.1.2 Designing a mouse holder for live imaging with MARS

In chapter 3, two mouse holders with thermoregulating devices were designed and manufactured. The main features of these holders are: restraints to secure the animal's position, heat delivery and temperature regulation, anaesthetic delivery, physiological monitoring, and a simple design/setup for ease of animal handling. The version 2 mouse holder, with a heater mounted inside it, could keep the mouse core temperature around 37 degrees in benchtop experiments.

Further work is required to make the version 2 holder fully functional with MARS scanners. Performing an in *in vivo* MARS scans with the version 2 holder, to test its functionality inside the scanner room is the next step.

7.1.3 Creating an intrinsic gating algorithm for MARS data

In chapter 4, an automatic image-based gating algorithm, was introduced and evaluated by a live mouse scan dataset. Scan data were pre-processed by applying a malfunctioning-pixel mask, flatfield correction, and ring artefact filtration. A pixel inpainting algorithm was developed and used to fill masked pixels. The motion signal was acquired based on the mean photon counts within a window that automatically tracked where motion occurred over time.

Exposure images were sorted into 2, 4, and 8 temporal bins based on the phase of the motion signal. Videos of the breathing cycle were produced in all three cases. Gated reconstructed volumes showed improvement in motion affected areas by having sharper edges around the diaphragm during the peak exhale phase.

The gating algorithm was evaluated using difference images and noise measurements. The motion structure obtained by using difference images highlighted the regions with

motion around the diaphragm. Increasing the number of temporal bins from two to eight significantly reduced the image quality of the gated images as the percentage of available exposure images for reconstruction was reduced from 50% to 5%. The SNR and CNR of the gated data were lower compared to the non-gated data as it used a fraction of available exposure images for the reconstruction of each temporal bin.

Testing the functionality of the gating algorithm on a few more datasets was an established goal for later chapters. We also want to improve the undersampling noise by using a higher number of exposure images contributing to the reconstruction of each temporal bin.

In the future, the intrinsic gating algorithm will be incorporated into the post-acquisition MARS imaging chain software. The motion gating algorithm will be applied to MARS human scans, acquired by MARS point-of-care scanners. In particular, the algorithm will be useful for cardiovascular disease studies involving carotid artery imaging to determine plaque vulnerability.

7.1.4 Evaluation of the gating algorithm with motion phantom

In chapter 5, a motorised motion phantom was designed and manufactured to simulate controllable periodic motion. This phantom was used to perform six scans by simulating a mouse's breathing frequency and setting the amplitude of the motion from 0 to 5 mm.

A weight-based reconstruction method for improving the undersampling artefacts of the temporal binning method was introduced and applied. Instead of temporal binning, this method assigns a weight to each exposure image based on the target phase selected by the user. All exposures contribute to the reconstruction of each temporal bin. It was shown that the weight-based reconstructed method improved the undersampling noise in the reconstructed images.

The gating algorithm was applied on the motion phantom data with amplitudes of 1 mm to 5 mm. The exposure images were reconstructed targeting the two peak phases

angles at 0^0 and 180^0. The reconstructed images in the stationary scan were considered to be a ground truth.

To evaluate the improvement in image quality by reducing the distortion, the Jaccard distance was measured for all volumes. The mean squared error was also measured for all reconstructed gated volumes by referencing the stationary volumes. The results of both methods showed that by applying gating motion artefacts and blurring reduced. The volumes of the gated data were more similar to the stationary scan compared to the non-gated data. By increasing the amplitude from 1 mm to 5 mm the visible blurring in the non-gated images increased. The gating improved the delineations of the edges and structures in the image particularly in motion affected areas such as perspex edge and vials. In gated data the perspex edge was sharper in the amplitude of 1 mm compared to the amplitude of 5 mm. The gated images in the amplitude of 1 mm were 50% and in 5 mm were 26% more similar to the stationary scan than the non-gated images, based on the Jaccard distance results.

In the future, we want to modify the weight-based reconstruction method to improve the low SNR to reduce the noise quantity of the gated images compared to the stationary and non-gated images. If the amount of motion is determined on a per-pixel basis, the weight term W could be unique to each pixel. That would allow the suppression of pixels with motion in one part of an exposure image while pixels without motion could be used to their full extent. As a result, the noise quantity of the gated images will be reduced. Prior Image Constrained Compressed Sensing (PICCS) method could also be used in parallel with the weight-based reconstruction algorithm to reduce the noise in gated data. The non-gated data or one of the temporal bins with an acceptable image quality could be used as prior image dataset.

A study needs to be done to improve the accuracy of the motion signal extraction method to enhance the accuracy of phase prediction in higher amplitudes such as 5 mm. This will consequently increase the image quality and reduce the remaining motion blurring in the gated images.

7.1.5 Material identification and motion

In chapter 6, we investigated the influence of motion on the results of MARS-MD's material identification and quantification accuracy. This was done by converting the motion phantom into a contrast motion phantom by inserting material solution vials of iodine, calcium, water, and a lipid. The MARS-MD algorithm was applied on the stationary scan, non-gated and gated scan data with amplitudes of 1 mm to 5 mm. The effect of motion on the material decomposition accuracy was tested on the images that were not expected to be highly distorted by motion (the centre of the material vials) and around the top edge of the material vials where it was expected to be profoundly affected by motion.

There was a fluctuation in identification and quantification in different scans, but mostly motion did not significantly alter the results in the central region. In the centre region of the material vials, the quantification values were higher than the true value for all materials. In the edge area, some fluctuation was also observed in identification and quantification in all materials in all six scans and no clear trends were observed.

The direction of the phantom's movements was parallel to the direction of the material vial's length. As a result, the parts of the vial that were affected by motion were limited and prevented us from observing the effect of motion in the majority of the vials. The gated images were sharper but, compared to the non-gated images, were also nosier. As a result, applying gating did not improve the material decomposition accuracy of the non-gated images. The presence of high noise interferes with achieving an acceptable material decomposition result.

The presence of air bubbles in the material vials prevented us from studying the MD at the very top edge slices as there was no available data. In the future, we need to take better care to eliminate all air bubbles when filling the material solutions. This can also be done by rotating vials 90 degrees. This means that the motion itself is still along the z-axis, but this is orthogonal to the direction along the length of the vials. As a result, the surface affected with motion will have a bigger area. This will also help to reduce the issues with the air bubbles.

These experiments were performed on the large material vials which were filled homogeneously. At the same time, the real-world problems investigate the effect of motion in a small feature such as lung nodules. The result of the experiments in 1 mm and 2 mm of movements can be a good example of such small movements in real-life problems. However, it is essential to repeat the test with live samples as the concentrations and texture of the materials are not as large as in our experiments. This may alter the results for the gated and the non-gated images. Modifying the frequency of the motion signals to be faster or slower to what we have examined can also be one of the next investigations in the future.

7.2 Research to be continued in the future

In this section, we will point out some research performed during this thesis but which require some further investigation in the future.

7.2.1 Extracting the motion signal based on the MARS scanner's geometrical information

The geometric model of the MARS scanner provides parameters for how the detectors in the camera and the X-ray source are positioned, oriented, and how they move relative to the volume. We used a tracking window where the tracking studied the pixel data to try to determine where it should be. Given that the scanner motion is known from the geometric model, we should not need any kind of tracking. Given a starting position, we could use the known geometric data to move the window as required. To accomplish this task, we developed an algorithm based on extracting some positional information from the MARS geometric model.

This algorithm is semi-automatic and requires user intervention to label the exposure images where a moving edge enters and exits from the exposure images. This algorithm uses the geometric z values of the detector position to predict what column the moving edge (such as diaphragm edge or perspex edge in the motion phantom) is when it is in the view of the exposure images, and the x and y values of the detector position are

used to move the window.

In the future, this algorithm should be applied on the live scan and the motion phantom data to investigate its performance in the accuracy of motion signal based on the ground truth signal. The correlation between the predicted phase angle and the ground truth signal's phases should be investigated. Finally, the image quality of the gated images with this method should be compared with the intrinsic gating method by using the evaluation metrics applied in this thesis.

7.2.2 A study on the effect of gaps between detectors on the motion signal

An investigation was performed to study how much of the motion signal originates from or is distorted by the gap between adjacent detectors. This was important as in new generations of the MARS camera the number of detectors increased to 14, and this will consequently increase the number of gaps present. To study the effect of detector gap on the acquired motion signal, the exposure image had whole rows and columns of the detectors masked out to simulate having more detector gaps. The effect was like splitting the detectors into virtual detectors that were either square or rectangular shapes. The motion direction goes across the image (horizontal). So the row gaps are parallel to the motion, and the column gaps are orthogonal to the motion.

The scan from 2 mm motion phantom was used in this study. The motion signal acquired by applying the intrinsic gating algorithm was taken as ground truth. The frequency of the motion signal from the virtual detectors was obtained by applying the Fast Fourier Transform (FFT) on each motion signal. The frequency of the virtual detector's signals was compared with the frequency of the ground truth.

The horizontal gaps and the vertical gaps, despite having different masked pixels along rows and columns, resulted in getting the same dominant frequency. The result showed the masked columns orthogonal to the motion direction could negatively alter the motion signal by adding some distinct patterns in the signal when the moving edge crossed into the gaps. In contrast, the masked gaps parallel to the direction of the

motion had minor effects on the signal.

This study needs to be further continued to compare the predicted phase angles acquired by having various virtual pixel gaps to the phase angles of the ground truth signal. We also need to investigate the effect of image quality improvements by using either of these motion signals. This will result in understanding the dependency of the motion signal on the gap between detectors.

7.2.3 A weight-based method to extract the motion signal from a region of interest

We have developed a method for assigning some weights to each pixel to suppress the effect of the presence of the air in the mean photon count calculation. An average can be biased if the majority of the values in the average come from one source. In gating, air can have such an effect, which is why we use windowing, to begin with. Air has the highest photon counts and does not show any motion from either the scanner or the subject. So suppressing air could help strengthen the motion signal in an intensity-based gating algorithm.

This idea was applied to the live animal dataset, and a motion signal was acquired based on it. However to study its effectiveness, the data needs to be reconstructed based on the acquired motion signal, and its image quality should be compared with the image quality of the motion signals acquired from the intrinsic gating algorithm. It is also recommended that this method be applied to the motion phantom so there is a ground-truth motion signal. The standard least-square between the predicted phase angles in both methods should be acquired and be compared by the phase angles of the ground truth signal. This will also help investigate which method can provide us with the most accurate motion signal.

7.2.4 A gradient weight-based gating method

Localising and tracking the outlying areas in the image that are under the influence of the motion is a primary step in gating algorithms. Accurately tracking and tracing a

region of interest will increase the accuracy of the motion signal. Therefore, we have developed a fine grain motion measurements algorithm that follows complex structures in exposure images and precisely locates and tracks the moving structures. This method compared to the intrinsic gating algorithm is free of any influence of the region of interest size and shape on acquiring the motion signal. It uses all the information available in the exposure image.

This algorithm is based on the per-pixel gradients between consecutive exposure images. Those gradient values are then smoothed over a large number of exposure images to try to identify areas with greater change i.e. more motion. Each pixel in an exposure image will be assigned a weight, based on the gradient value, and the motion signal is acquired as a weighted average over the whole image instead of the tracking window we used.

This method was tested on the motion phantom datasets of 1 mm and 5 mm. The reconstructed data in the peak phases showed improvements by the reduction of noise and blurring in motion affected areas. In the future, we will further investigate the functionality and performance of this method by applying it on different scan datasets such as the motion phantom with various amplitudes and frequencies. It is also recommended to apply this method on the live scan dataset and see its performance in detection of fine structures in the lung. This will provide a reliable reference to compare the potential improvements upon the intrinsic gating algorithm, which was not able to be completed in the time of this thesis.

7.3 Future goals

In this section, we recommend the future goals and directions for live animal imaging with MARS scanners, based on the major findings in this thesis.

7.3.1 Short term outlook

In the short term for the small animal imaging, by modifying the 2nd version of the mouse holder with a temperature regulating system based on the recommendations in

chapter 3, this holder will be available for all MARS users in the team, collaborators, and customers. This will facilitate *in vivo* longitudinal imaging with MARS small-bore scanners.

In the short term for the gating algorithm, we need to modify the weight-based image reconstruction algorithm to further improve the image quality of the gated images by reducing the noise. This will help us to more accurately investigate the difference between the MARS-MD results on the gated and non-gated images by having the same amount of noise quantity.

It is necessary to study methods to further increase the accuracy of the motion signal, which then is used to generate the predicted phase angles for each exposure image. As it was shown in chapter 5, by increasing the amplitude of the motion the accuracy of predicted phases was reduced, which resulted in some blurring around the perspex vials and edges. We hope to acquire more accurate motion signal based on the gradient weight-based gating method as it utilises all the information available in the exposure images compared to the current gating method which tracks a fixed size ROI around the moving edge.

The effect of motion of the MARS-MD needs to be further investigated by preventing air bubbles in the vials and modifying the direction of the material vials to have a larger surface area to investigate the effect of motion on the material decomposition. Ultimately, new scans with live samples can be done with having contrast agents administered in them to study how MARS-MD is influenced by a live mouse cardio-respiratory motion and how gating can improve it.

7.3.2 Mid term outlook

In the mid term, for live imaging, a magnetic plug can be used to easily connect the physiological cables to their extensions. Extension cables can be permanently placed inside the scanner. The whole design needs to be more commercially appealing in order to make it commercially available for the market. Instead of having a heater inside the holder, an infrared lamp could be installed inside the MARS scanners to keep the

mouse warm during the scan time. A camera can be added to the mouse holder with a FOV over the upper body of the mouse. The video can later be used in some algorithms such as feature tracking and motion vector extraction.

The subject continuously moves while the scanner acquires the exposure images. During the dead time, the shutter closes and no scan data is acquired. From the scanner point of view, a further reduction of the dead time will help to capture each motion phase closer to its previous one without losing some data in between. It will also reduce the total scan time. This will also contribute to the accuracy of the acquired motion signal as the time interval between each two acquired exposure image is shorter.

One other possibility will be the reduction of the exposure time to be small enough to capture one motion phase interval during each acquisition. For example, if an average breathing cycle of a mouse is 60 breaths per second, with the common 220 ms exposure time, in a one second interval only 4.5 exposure images are acquired. By further reducing the exposure time the number of acquired images will be increased, which will further help in reducing the undersampling noise and accurately tracking the motion phases. However, there is a trade-off between the image quality and exposure time of the MARS scanners that need to be considered.

The mid term goal for gating is to study the functionality of the algorithm on the MARS human data. This can first be done on the human's carotid artery wall movements as it has motion in a similar range to that which we studied in this thesis. Videos of carotid arteries movements can be generated for diagnosis purposes. The next step is applying the finalised gating algorithm for human breathing. This would require further investigation and improvements on the current gating method as based on the results shown in this thesis there would still be motion blur if we keep the same voxel size.

7.3.3 Long term outlook

MARS imaging using Medipix3RX detectors has shown that it can provide more informative images for diagnosis and treatment compared to conventional CT images. For

example, previous researchers showed that preclinical MARS scanners enabled them to distinguish physiological structures of the cardiovascular disease in *ex vivo* samples (Prebble *et al.*, 2018). MARS researches have published the first human image acquired by MARS scanners and in the near future, the human scanner will be available for clinical trials (Panta *et al.*, 2018).

In the future, the long term goal of the MARS team for *in vivo* small animal imaging is performing cardio-respiratory functional imaging to investigate cardiac and lung diseases. Administering contrast agents will also assist in getting higher soft-tissue contrast with the spectral imaging. The mouse holder will assist in longitudinal imaging for studying the disease progression and drug delivery in real-time.

In human imaging, gating will suppress the motion artefacts and reduce blurring in the motion affected area. The implementation of gating in the MARS system will also assist in performing studies in lung cancer for better depiction of the tumour and measurements of lung tumours volumes. Based on the results presented in this thesis, gated images reduce motion artefacts and blurring and improve the visibility of the lesions and structures in the lungs. This will assist in accurately delineating the volume and the location of the tumours for diagnosis and treatment planning.

7.4 Conclusion

The first aim of this project was facilitating live imaging for the preclinical research being conducted by the small-bore MARS spectral CT scanners all around the world. This goal was achieved by designing and manufacturing a MARS compatible mouse holder with a thermo-regulating system.

The second aim was improving the image quality of the motion affected images by developing a gating algorithm applicable to both small-bore and the human-scale dataset. This increases the accuracy of the diagnosis and consequently, the efficiency of the treatment, which bring health benefits to the broad range of MARS users. This goal was also achieved by the development and evaluation of a gating algorithm for all MARS scanners.

The author hopes the output of this thesis contributes to advancing MARS spectral CT imaging systems by facilitating live animal imaging in the small-bore scanner. Also, improving the diagnostic accuracy of motion-affected images in both MARS preclinical and human-scale scanners.

References

Alvarez, R. E. and Macovski, A. (1976). Energy-selective reconstructions in x-ray computerised tomography. *Physics in Medicine & Biology*, **21**(5), 733.

Anjomrouz, M. (2017). *Investigation of MARS spectral CT: X-ray source and detector characterization*. Ph.D. thesis, University of Otago.

Arduino (2019). https://www.arduino.cc.

Badea, C., Drangova, M., Holdsworth, D. W., and Johnson, G. (2008). In vivo small-animal imaging using micro-ct and digital subtraction angiography. *Physics in Medicine & Biology*, **53**(19), R319.

Barrett, J. F. and Keat, N. (2004). Artifacts in ct: recognition and avoidance. *Radiographics*, **24**(6), 1679–1691.

Bartling, S. H., Dinkel, J., Stiller, W., Grasruck, M., Madisch, I., Kauczor, H.-U., Semmler, W., Gupta, R., and Kiessling, F. (2008). Intrinsic respiratory gating in small-animal ct. *European Radiology*, **18**(7), 1375.

Bartling, S. H., Kuntz, J., and Semmler, W. (2010). Gating in small-animal cardiothoracic ct. *Methods*, **50**(1), 42–49.

Bateman, C., Knight, D., Brandwacht, B., Mc Mahon, J., Healy, J., Panta, R., Aamir, R., Rajendran, K., Moghiseh, M., Ramyar, M., *et al.* (2018). Mars-md: rejection based image domain material decomposition. *Journal of Instrumentation*, **13**(05), P05020.

Bateman, C. J. (2015). *Methods for material discrimination in MARS multi-energy CT*. Ph.D. thesis, University of Otago.

Becker, N., Quirk, S., Kay, I., Braverman, B., and Smith, W. L. (2013). A comparison of phase, amplitude, and velocity binning for cone-beam computed tomographic projection-based motion reconstruction. *Practical Radiation Oncology*, **3**(4), e209–e217.

Berbeco, R. I., Mostafavi, H., Sharp, G. C., and Jiang, S. B. (2005). Towards fluoroscopic respiratory gating for lung tumours without radiopaque markers. *Physics in Medicine & Biology*, **50**(19), 4481.

Brahme, A. (2014). *Comprehensive biomedical physics*. Newnes.

Brey, E. M. (2014). *Vascularization: regenerative medicine and tissue engineering*. CRC Press.

Burk, L. M., Lee, Y. Z., Wait, J. M., Lu, J., and Zhou, O. Z. (2012). Non-contact respiration monitoring for in-vivo murine micro computed tomography: characterization and imaging applications. *Physics in Medicine & Biology*, **57**(18), 5749.

Burleson, S., Baker, J., Hsia, A. T., and Xu, Z. (2015). Use of 3d printers to create a patient-specific 3d bolus for external beam therapy. *Journal of Applied Clinical Medical Physics*, **16**(3), 166–178.

Carlsson, C. A. and Alm Carlsson, G. A. (1973). *Basic physics of X-ray imaging*. Linköping University Electronic Press.

Caro, A. C., Hankenson, F. C., and Marx, J. O. (2013). Comparison of thermoregulatory devices used during anesthesia of c57bl/6 mice and correlations between body temperature and physiologic parameters. *Journal of the American Association for Laboratory Animal Science*, **52**(5), 577–583.

Chavarrías, C., Vaquero, J., Sisniega, A., Rodríguez-Ruano, A., Soto-Montenegro, M., García-Barreno, P., and Desco, M. (2008). Extraction of the respiratory signal from

small-animal ct projections for a retrospective gating method. *Physics in Medicine & Biology*, **53**(17), 4683.

Claudio, V., Aaron, A., Ralph, W., and Lee, S. (2015). New techniques for motion-artifact-free in vivo cardiac microscopy. *Frontiers in Physiology*, **6**(MAY).

Cleveland, W. S. (1979). Robust locally weighted regression and smoothing scatterplots. *Journal of the American statistical association*, **74**(368), 829–836.

Constantinides, C., Mean, R., and Janssen, B. J. (2011). Effects of isoflurane anesthesia on the cardiovascular function of the c57bl/6 mouse. *ILAR journal/National Research Council, Institute of Laboratory Animal Resources*, **52**, e21.

De Ruiter, N. (2015). *Algorithms to process data from the MARS molecular imaging system*. Ph.D. thesis, University of Otago.

De Ruiter, N. J., Butler, P. H., Butler, A. P., Bell, S. T., Chernoglazov, A. I., and Walsh, M. F. (2017). Mars imaging and reconstruction challenges. In *Proceedings of the 14th International Meeting on Fully Three-Dimensional Image Reconstruction in Radiology and Nuclear Medicine, Xi'an, China*, pages 18–23.

Dinkel, J., Bartling, S. H., Kuntz, J., Grasruck, M., Kopp-Schneider, A., Iwasaki, M., Dimmeler, S., Gupta, R., Semmler, W., Kauczor, H.-U., *et al.* (2008). Intrinsic gating for small-animal computed tomography: a robust ecg-less paradigm for deriving cardiac phase information and functional imaging. *Circulation: Cardiovascular Imaging*, **1**(3), 235–243.

Ewald, A. J., Werb, Z., and Egeblad, M. (2011). Monitoring of vital signs for long-term survival of mice under anesthesia. *Cold Spring Harbor Protocols*, **2011**(2), pdb–prot5563.

Ferreira, C., Ximenes Filho, R., Vieira, J., Tomal, A., Poletti, M., Garcia, C., and Maia, A. (2010). Evaluation of tissue-equivalent materials to be used as human brain tissue substitute in dosimetry for diagnostic radiology. *Nuclear Instruments and Methods in Physics Research Section B: Beam Interactions with Materials and Atoms*, **268**(16), 2515–2521.

Fitzpatrick, M. J., Starkschall, G., Antolak, J. A., Fu, J., Shukla, H., Keall, P. J., Klahr, P., and Mohan, R. (2006). Displacement-based binning of time-dependent computed tomography image data sets. *Medical Physics*, **33**(1), 235–246.

Ford, N., Martin, E. L., Lewis, J., Veldhuizen, R., Holdsworth, D., and Drangova, M. (2009). Quantifying lung morphology with respiratory-gated micro-ct in a murine model of emphysema. *Physics in Medicine & Biology*, **54**(7), 2121.

Ford, N. L., Martin, E. L., Lewis, J. F., Veldhuizen, R. A., Drangova, M., and Holdsworth, D. W. (2007a). In vivo characterization of lung morphology and function in anesthetized free-breathing mice using micro-computed tomography. *Journal of Applied Physiology*, **102**(5), 2046–2055.

Ford, N. L., Wheatley, A. R., Holdsworth, D. W., and Drangova, M. (2007b). Optimization of a retrospective technique for respiratory-gated high speed micro-ct of free-breathing rodents. *Physics in Medicine & Biology*, **52**(19), 5749.

Ford, N. L., McCaig, L., Jeklin, A., Lewis, J. F., Veldhuizen, R. A., Holdsworth, D. W., and Drangova, M. (2017). A respiratory-gated micro-ct comparison of respiratory patterns in free-breathing and mechanically ventilated rats. *Physiological reports*, **5**(2), e13074.

Glass, I., Butler, A. P., Butler, P. H., Bones, P. J., and Weddell, S. J. (2013). Physiological gating of the mars spectral micro ct scanner. In *2013 28th International Conference on Image and Vision Computing New Zealand (IVCNZ 2013)*, pages 317–322. IEEE.

Gonzalez, R. C. and Woods, R. E. (2007). Image processing. *Digital Image Processing*, **2**, 1.

Guo, X., Johnston, S. M., Qi, Y., Johnson, G. A., and Badea, C. T. (2011). 4d micro-ct using fast prospective gating. *Physics in Medicine & Biology*, **57**(1), 257.

Hegazy, M. A., Eldib, M. E., Mun, Y. J., Cho, M. H., Cho, M. H., and Lee, S. Y. (2017). A bench-top micro-ct capable of simulating head motions. *Biomedical Engineering Letters*, **7**(3), 237–244.

Horioka, K., Tanaka, H., Isozaki, S., Okuda, K., Asari, M., Shiono, H., Ogawa, K., and Shimizu, K. (2019). Hypothermia-induced activation of the splenic platelet pool as a risk factor for thrombotic disease in a mouse model. *Journal of Thrombosis and Haemostasis*, **17**(10), 1762–1771.

Jiang, H. (2009). Computed tomography: principles, design, artifacts, and recent advances. In *SPIE*.

Kavanagh, A., Evans, P. M., Hansen, V. N., and Webb, S. (2009). Obtaining breathing patterns from any sequential thoracic x-ray image set. *Physics in Medicine & Biology*, **54**(16), 4879.

Kuntz, J., Dinkel, J., Zwick, S., Bäuerle, T., Grasruck, M., Kiessling, F., Gupta, R., Semmler, W., and Bartling, S. (2010). Fully automated intrinsic respiratory and cardiac gating for small animal ct. *Physics in Medicine & Biology*, **55**(7), 2069.

Lee, S., Vinegoni, C., Sebas, M., and Weissleder, R. (2014). Automated motion artifact removal for intravital microscopy, without a priori information. *Scientific reports*, **4**, 4507.

Lowe, C. D., Ortega, A., Aamir, R., Chernoglazov, A. I., Butler, A. P., Anderson, N. G., Moghiseh, M., Asghariomabad, F., Butler, P. H., de Ruiter, N. J., *et al.* (2018). Mars pulmonary spectral molecular imaging: potential for locating tuberculosis involvement. In *2018 IEEE Nuclear Science Symposium and Medical Imaging Conference Proceedings (NSS/MIC)*, pages 1–4. IEEE.

Martin, R., Rubinstein, A., Ahmad, M., Court, L., and Pan, T. (2015). Evaluation of intrinsic respiratory signal determination methods for 4d cbct adapted for mice. *Medical Physics*, **42**(1), 154–164.

Moghiseh, M., Aamir, R., Panta, R. K., de Ruiter, N., Chernoglazov, A., Healy, J., Butler, A., and Anderson, N. (2016). Discrimination of multiple high-z materials by multi-energy spectral ct–a phantom study. *JSM Biomed Imaging Data Pap*, **61**, 1007.

Moghiseh, M., Lowe, C., Lewis, J. G., Kumar, D., Butler, A., Anderson, N., and Raja, A. (2018). Spectral photon-counting molecular imaging for quantification of monoclonal antibody-conjugated gold nanoparticles targeted to lymphoma and breast cancer: an in vitro study. *Contrast media and Molecular imaging*, **2018**.

National Institute of Standards and Technology (NIST). https://www.nist.gov.

Panta, R. K., Butler, A. P., Butler, P. H., de Ruiter, N. J., Bell, S. T., Walsh, M. F., Doesburg, R. M., Chernoglazov, A. I., Goulter, B. P., Carbonez, P., *et al.* (2018). First human imaging with mars photon-counting ct. In *2018 IEEE Nuclear Science Symposium and Medical Imaging Conference Proceedings (NSS/MIC)*, pages 1–7. IEEE.

Prebble, H., Cross, S., Marks, E., Healy, J., Searle, E., Aamir, R., Butler, A., Roake, J., Hock, B., Anderson, N., *et al.* (2018). Induced macrophage activation in live excised atherosclerotic plaque. *Immunobiology*, **223**(8-9), 526–535.

Rahmim, A., Bloomfield, P., Houle, S., Lenox, M., Michel, C., Buckley, K. R., Ruth, T. J., and Sossi, V. (2004). Motion compensation in histogram-mode and list-mode em reconstructions: beyond the event-driven approach. *IEEE Transactions on Nuclear Science*, **51**(5), 2588–2596.

Rit, S., Sarrut, D., and Ginestet, C. (2005). Respiratory signal extraction for 4d ct imaging of the thorax from cone-beam ct projections. In *International Conference on Medical Image Computing and Computer-Assisted Intervention*, pages 556–563. Springer.

SAII - Instruments For Small Animals (2017). http://www.i4sa.com/.

Sara, U., Akter, M., and Uddin, M. S. (2019). Image quality assessment through fsim, ssim, mse and psnr—a comparative study. *Journal of Computer and Communications*, **7**(3), 8–18.

Schambach, S. J., Bag, S., Schilling, L., Groden, C., and Brockmann, M. A. (2010). Application of micro-ct in small animal imaging. *Methods*, **50**(1), 2–13.

Schumann, A. Y., Kuhnhold, A., Fuchs, K., Bartsch, R. P., Bauer, A., Schmidt, G., and Kantelhardt, J. W. (2010). Reconstructed respiration and cardio-respiratory phase synchronization in post-infarction patients. *Proceedings of the 6th ESGCO*, pages 1–4.

Smith, J. O. (2007). *Mathematics of the discrete Fourier transform (DFT): with audio applications*. Julius Smith.

Studinger, P., Lénárd, Z., Kováts, Z., Kocsis, L., and Kollai, M. (2003). Static and dynamic changes in carotid artery diameter in humans during and after strenuous exercise. *The Journal of Physiology*, **550**(2), 575–583.

Suckow, C., Kuntner, C., Chow, P., Silverman, R., Chatziioannou, A., and Stout, D. (2009). Multimodality rodent imaging chambers for use under barrier conditions with gas anesthesia. *Molecular Imaging and Biology*, **11**(2), 100–106.

Sutton, D. (1987). A textbook of radiology and imaging.

T O'Brien, R., Kipritidis, J., Shieh, C.-C., and Keall, P. J. (2014). Optimizing 4dcbct projection allocation to respiratory bins. *Physics in Medicine & Biology*, **59**(19), 5631.

Taguchi, K., Blevis, I., and Iniewski, K. (2020). *Spectral, Photon Counting Computed Tomography: Technology and Applications*. CRC Press.

Taylor, D. K. (2007). Study of two devices used to maintain normothermia in rats and mice during general anesthesia. *Journal of the American Association for Laboratory Animal Science*, **46**(5), 37–41.

The Mathworks, Inc. (2017). https://au.mathworks.com/products/matlab.html.

Tremoleda, J. L., Kerton, A., and Gsell, W. (2012). Anaesthesia and physiological monitoring during in vivo imaging of laboratory rodents: considerations on experimental outcomes and animal welfare. *EJNMMI research*, **2**(1), 44.

Vedam, S., Keall, P., Kini, V., Mostafavi, H., Shukla, H., and Mohan, R. (2002). Acquiring a four-dimensional computed tomography dataset using an external respiratory signal. *Physics in Medicine & Biology*, **48**(1), 45.

Vergalasova, I., Cai, J., and Yin, F.-F. (2012). A novel technique for markerless, self-sorted 4d-cbct: Feasibility study. *Medical Physics*, **39**(3), 1442–1451.

Walsh, M. F. (2014). *Spectral computed tomography development*. Ph.D. thesis, University of Otago.

Wang, Z., Bovik, A. C., Sheikh, H. R., and Simoncelli, E. P. (2004). Image quality assessment: From error measurement to structural similarity. *IEEE Transactions on Image Processing*, **13**(1).

Yan, H., Wang, X., Yin, W., Pan, T., Ahmad, M., Mou, X., Cerviño, L., Jia, X., and Jiang, S. B. (2013). Extracting respiratory signals from thoracic cone beam ct projections. *Physics in Medicine & Biology*, **58**(5), 1447.

Yin, W., Goldfarb, D., and Osher, S. (2007). A comparison of three total variation based texture extraction models. *Journal of Visual Communication and Image Representation*, **18**(3), 240–252.

Zijp, L., Sonke, J.-J., and van Herk, M. (2004). Extraction of the respiratory signal from sequential thorax cone-beam x-ray images. pages 507–509.

Appendix A

Inpainting algorithm

A.1 Inpainting algorithm

In this appendix, the inpainting algorithm applied in section 4.3.1 in chapter 4 is introduced.

To set the neighbouring window size, first convert the grey-scale image into a binary image where the masked pixels possess a value of one, and good pixels have a value of zero. Then compute the maximum number of consecutive one values along the columns in the image(M_c). For each masked pixel, place a window of ($2\times$M$_c$)+1 by ($2\times$M$_c$)+1 pixels centred around the masked pixel. The masked pixel will be replaced with one of its good pixel neighbours in the image based on algorithm A.1.

The reason for choosing the M_c as the inpainting window size originates from the fact that even when removing the gap between adjacent detectors, there might still be rows with mostly masked pixels. An example is a masked row between detector two and three in Fig. 4.2c. Therefore, choosing the maximum number of consecutive one values across the rows will result in a safe window size for the inpainting algorithm.

We tested the algorithm for exposure images acquired from three, seven and fourteen detector MARS cameras. For a three detector exposure image, the value of M_c was 8 pixels long. About 984 of the total pixels in the exposure image were inpainted success-

fully. For a seven exposure image, the M_c value was also 8 pixels, and 1255 of pixels of the whole image were inpainted. In a fourteen exposure image, the M_c was 47 pixels and 13763 pixels of total pixels in the image were inpainted. The example of fourteen detectors images was a severe case with almost half a detector in poor condition. For the initial gating work, the algorithm demonstrated a competent performance. Fig. A.1 shows an exposure image acquired from the motion phantom with the amplitude of 5 mm in a seven exposure image after applying the inpainting algorithm on (a).

Algorithm A.1 Pixel inpainting algorithm

Go through all the pixels in the image:

for *all masked pixels in the image* **do**

- **if** *the masked pixel is not located on the edges of the image* **then**
  - define a window of $(2M_c)+1$ by $(2M_c)+1$ pixels centred around the masked pixel.
- **else**
  - Shrink a $(2M_c)+1$ by $(2M_c)+1$ pixel window centred around the masked pixel to fit on the image.
- **for** *each pixel in the window* **do**
  - **if** *the pixel is not masked* **then**
    - Determine the distance between this pixel and the masked pixel
    - Register the pixel if it has the smallest distance so far
    - Copy the value of the registered unmasked pixel into the masked pixel

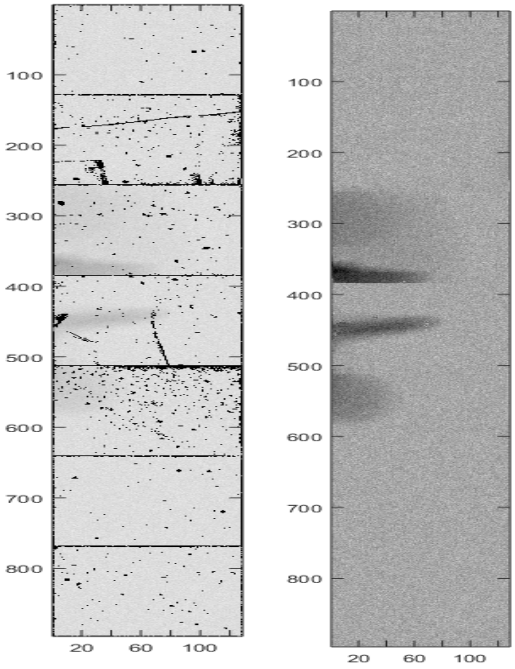

(a) (b)

Figure A.1: An illustration of applying inpainting algorithm on a seven detectors exposure image. The original exposure image is shown in (a). The result after applying the inpainting algorithm on (a) is shown in (b).

Appendix B

A post-reconstruction image enhancement algorithm

B.1 Intensity enhancement algorithm

In this section, our objective is to increase the sharpness of reconstructed data. This aim can be accomplished by applying an intensity enhancement algorithm based on the conjunction of the Laplacian and gradient operator. This algorithm is written based on a method proposed in a book by Gonzalez and Woods (2007) and is updated for MARS data.

The Laplacian operator focuses on the regions with rapid intensity changes (i.e. curvature) and glosses over areas with gradually differing intensity. This transform intensifies the fine details such as thin lines and points and forms noisier results compared to the Gradient operator.

The Gradient operator intensifies prominent edges in an image and cancels moderately changing background features. It has a robust average response in the area of eminent intensity conversion, such as edges compared to the Laplacian. The gradient has a lower response to fine details and noise than the Laplacian.

Applying a combination of best characteristics of the Laplacian and Gradient, can compensate for the noise and enhance the structural features in the image. This combination maintains details in edge areas and reduces noise in flat areas.

Code was developed in MATLAB to increase the precision and clearness of the MARS reconstructed data for medical evaluation purposes. The algorithm is presented in Algorithm B.1.

Algorithm B.1 After reconstruction intensity enhancement process

for *Reconstructed slice number i = 1 to end* **do**

1- Computing the Laplacian image:

$$\text{Laplacian Kernel} = \begin{bmatrix} -1/8 & -1/8 & -1/8 \\ -1/8 & 1 & -1/8 \\ -1/8 & -1/8 & -1/8 \end{bmatrix}$$

Laplacian image = convolution (Original image (i), Laplacian Kernel)

2- Computing the sharpened image:

Sharpened image = summation (Original image (i) and Laplacian image)

3- Computing the Gradient image:

Gradient image = gradient (Original image (i) based on Sobel method)

4- Smoothing the Gradient image:

Smooth gradient image = Convolution (Original image (i), 5 by 5 averaging filter)

5- Computing mask:

Mask image = Multiply (Sharpened image and Smooth gradient image)

6- Enhancing the image:

Enhanced image= summation(Original image(i) and Mask image)

7- Calculating Gamma corrected image:

```
/* To make image dark take value of gamma > 1, to make image bright take
value of gamma < 1                                                    */
```

Gamma corrected image = Multiply (constant factor C and (Enhanced image to gamma power))

An example of the application of this method on the motion phantom dataset is illustrated in Fig. B.1. The process starts by calculating the Laplacian of the original image, presented in Fig. B.1a.

The convolution Kernal was used in the MATLAB environment to estimate the second derivative (Laplacian image), shown in Fig. B.1b. The sharpened image is acquired by the summation of the original image and the Laplacian image, displayed Fig. B.1c.

The gradient of the original image is calculated with the Sobel operator, which results in a more edge dominated image, shown in Fig. B.1d. This step was followed by the convolution of the original image with an averaging filter to further lower the gradient's response to noise and fine details, resulting in smoothed Sobel image, displayed in Fig. B.1e.

A mask image was calculated by multiplying the Laplacian and smoothed Sobel image, shown in Fig. B.1h. The mask image has sharper edges and less visible noise than the final sharpened image is acquired by summing the original image with the mask image, shown in Fig. B.1g. A power-law transformation function was applied to the final sharpened image to enhance the dynamic range. The gamma value was set to be 1.5 and C (constant factor) was 1.

The enhanced reconstructed images further highlight details and structures. This algorithm can be used as a post-reconstruction algorithm to enhance any images from the MARS scanners.

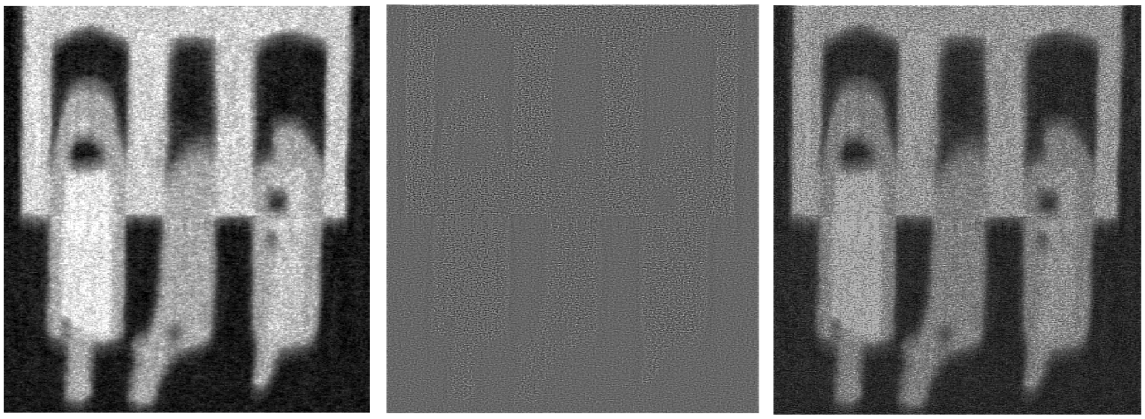

(a) Original image (b) Laplacian image (c) Sharpend image

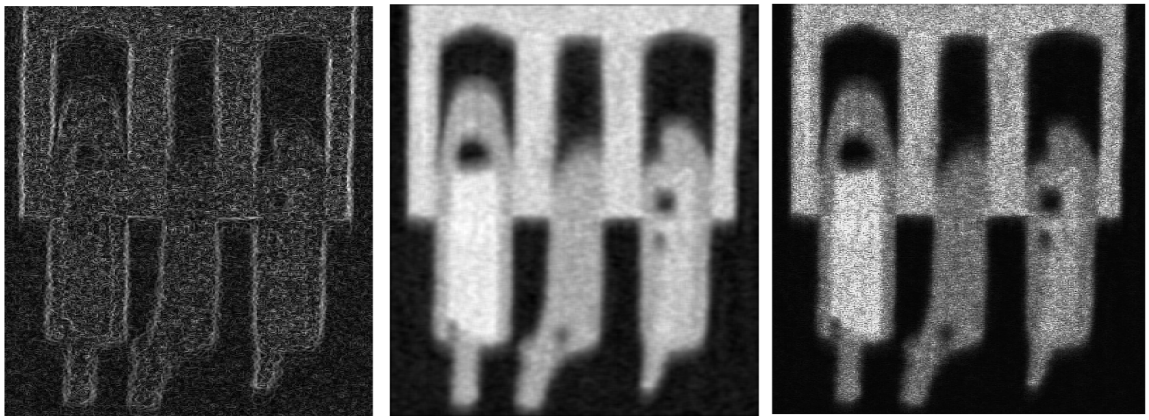

(d) Sobel gradient image (e) Smoothed gradient image (f) Masked image

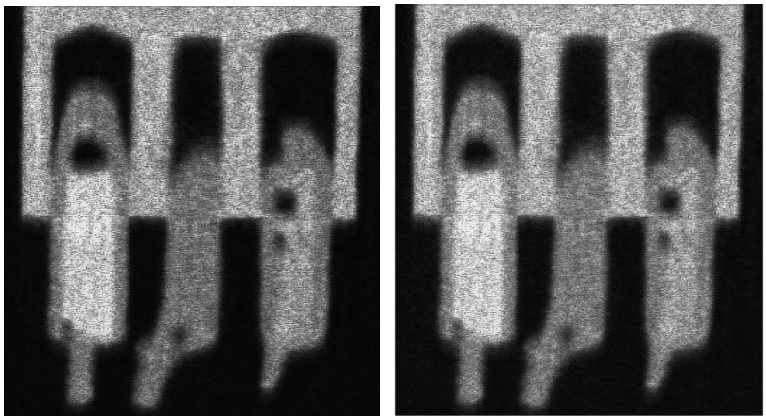

(g) Final enhanced image (h) Gamma corrected image

Figure B.1: The steps in the application of an image enhancement algorithm on a reconstructed slice. The sharpened image is a result of the application of an algorithm based on the conjunction of the Laplacian and the gradient operator. Sharper edges are the final result of this algorithm.